

**EXPERIMENTAL STUDY ON AERODYNAMIC CHARACTERISTICS  
OF NACA 4412 AEROFOIL WITH DIFFERENT PLANFORMS**

**By**

**Mohammad Shariful Islam**

**MASTER OF SCIENCE IN MECHANICAL ENGINEERING**



**Department of Mechanical Engineering**

Bangladesh University of Engineering & Technology

**October 2017**

**EXPERIMENTAL STUDY ON AERODYNAMIC CHARACTERISTICS  
OF NACA 4412 AEROFOIL WITH DIFFERENT PLANFORMS**

By

**Mohammad Shariful Islam**

A Thesis Submitted to the Department of Mechanical Engineering in  
partial fulfillment of the requirements for the degree of

Master of Science  
in  
Mechanical Engineering

Department of Mechanical Engineering  
Bangladesh University of Engineering & Technology  
Dhaka-1000, Bangladesh

## **DEDICATION**



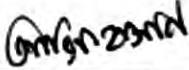


Dedicate this thesis

To my teachers;

To my parents and family

The thesis titled "Experimental Study on Aerodynamic Characteristics of NACA 4412 Aerofoil with Different Planforms," submitted by **Mohammad Shariful Islam**, Roll: 1014102043 P, Session: October-2014, has been accepted as satisfactory in partial fulfillment of the requirements for the degree of Master of Science in Mechanical Engineering on 28<sup>th</sup> October 2017.

### BOARD OF EXAMINERS

1.   
\_\_\_\_\_  
Dr. Mohammad Ali  
Professor  
Department of Mechanical Engineering  
BUET, Dhaka-1000, Bangladesh. Chairman  
(Supervisor)
2.   
\_\_\_\_\_  
Head  
Department of Mechanical Engineering  
BUET, Dhaka-1000, Bangladesh. Member  
(Ex-Officio)
3.   
\_\_\_\_\_  
Dr. Mohammad Arif Hasan Mamun  
Professor  
Department of Mechanical Engineering  
BUET, Dhaka-1000, Bangladesh. Member
4.   
\_\_\_\_\_  
Dr. Mohammad Mamun  
Professor  
Department of Mechanical Engineering  
BUET, Dhaka-1000, Bangladesh. Member
5.   
\_\_\_\_\_  
Dr. Md. Quamrul Islam  
Professor  
Military Institute of Science & Technology  
Mirpur, Dhaka-1216, Bangladesh. Member  
(External)

## **ABSTRACT**

The main function of a wing of an aircraft is to generate lift force to make the flight possible in the air. This force is generated by a special wing cross section which is called aerofoil. and the silhouette of the wing when viewed from above or below is known as wing planform. In this research, NACA 4412 aerofoil planform is used due to have good stall properties and low roughness effect. As the aerodynamic characteristics of aerofoils play a pivotal role to develop an aircraft, it is wanted to explore aerodynamic characteristics from five planforms (wooden-plastic) models. All the models are prepared keeping the overall surface area alike with changing the aspect ratio (AR) of wings. The rectangular planform (Model-1: AR- 1.929) is considered as reference model to compare with the other models which are incorporating curvature at the leading edge for two models (Model- 2: AR- 2.96 and Model- 3: AR- 2.57) and at the trailing edge for two models (Model- 4: AR- 3.11 and Model- 5: AR- 2.96).

All the models are tested at air speed of 79.20 kph (0.06 Mach) i.e. at Reynolds Number  $1.74 \times 10^5$  in the closed circuit wind tunnel. The static pressure at  $-4^\circ$ ,  $0^\circ$ ,  $4^\circ$ ,  $8^\circ$ ,  $12^\circ$ ,  $16^\circ$ ,  $20^\circ$  and  $24^\circ$  angle of attack are measured from both upper and lower surfaces of models by using a multi-tube manometer. After analyzing the data, it is found that the curved trailing edge wing planforms. have better lift coefficient, lower drag coefficient and better lift to drag ratio than other planforms whereas the curved leading edge planforms have better performance than rectangular planform. It is found that a wing of high AR (Model- 4) is produced less induced drag than a wing of low AR due to the less air disturbance at the tip of a longer and thinner wing.

It is observed that the critical angle of attack of all the five planforms remain around  $16^\circ$  beyond which the stall occurs. So, to obtain maximum lift from NACA 4412 aerofoil, the wing needs to be positioned at around 16 degrees with respect to the flight path whereas curved trailing edge planforms of NACA 4412 shows the better result. Therefore, this type of models may be considered to design a wing of aircraft.

## **ACKNOWLEDGEMENT**

First of all, my thanks and gratitude to Allah for the completion of this research successfully. Many people deserve thanks for making this research possible. I would like to express my heart-felt thanks and sincere gratitude to my supervisor Dr. Mohammad Ali, Professor and Head, Department of Mechanical Engineering, BUET, Dhaka, for his continuous guidance, supervision, inspiration, encouragement, and untiring support throughout this research work and sharing of his in depth knowledge on experimental research and the field of flow separation control. I could not have wished for a better advisor for this research.

I am also grateful to Professor Dr. Md. Quamrul Islam, Department of Mechanical Engineering, MIST, Dhaka and Professor Dr. Mohammad Arif Hasan Mamun and Professor Dr. Mohammad Mamun, Department of Mechanical Engineering, BUET, Dhaka for their cooperation and suggestions whenever needed. It is beyond doubt that without their assistance and kind support, it was impossible for me to complete this research work.

I feel proud to express that all of my family members including my mother, son, daughter, brothers and sisters gave me help, guidance and inspiration throughout this work. Their sacrifice and love made this thesis a great success in my carrier. I also want to mention Dr. Mst Rukshana Sultana, my spouse, because without her love and unlimited support, I definitely would not have achieved this result.

Special thanks goes to Md Atif Yasir , Kamruzzam Nayem, Tahsin Zaman and Shahadat Hossain Shihab for their sincere curiosity and help on the research. Finally, I like to express my sincere thanks to all other Teachers and Staffs of BUET for their cooperation and help in the successful completion of the work.

## DECLARATION

No portion of the work contained in this thesis has been submitted in support of an application for another degree or qualification of this or any other University or Institution of learning.



---

Dr. Mohammad Ali  
Supervisor



---

Mohammad Shariful Islam  
Author

# CONTENTS

	<b>Page</b>
Cover Sheet	I
Title	II
Dedication	III
Certificate of Approval	IV
Abstract	V
Acknowledgement	Vi
Candidate's Declaration	VII
Contents	VIII-XI
List of Figures	XII-XV
List of Tables	XVI
Nomenclature	XVII
<b>CHAPTER - 1 INTRODUCTION</b>	<b>1-4</b>
1.1 General	1
1.2 Background	1
1.3 Problem Statement	2
1.4 Motivation of the Research Work	3
1.5 Scope and Objectives of the Research	3
1.6 Outline of the Research	4



	<b>Page</b>
<b>CHAPTER-2 LITERATURE REVIEW</b>	6-13
<b>CHAPTER-3 OVERVIEW OF WING AERODYNAMICS</b>	14-30
3.1 Wing and Aerofoil	14
3.2 Aerodynamic Characteristics of Wing	15
3.3 General Features of an Aerofoil	15
3.2.1 Terminologies	15
3.2.2 NACA Aerofoil	16
3.4 Aerodynamic Forces Developed by Aerofoil	17
3.5 Lift and Drag Coefficient of Aerofoil	20
3.6 Aerofoil Data Sources	22
3.7 Co-ordinates of NACA Aerofoils	23
3.8 Geometric Parameters of Wing	24
3.8.1 Mean Geometric Chord	24
3.8.2 Mean Aerodynamic Chord	25
3.8.3 Aspect Ratio	25
3.8.4 Tapper Ratio	25
3.9 Familiarization with Different Wing Planforms	25
3.9.1 According to Aspect Ratio	26
3.9.2 According to Wing Sweep	26
3.9.3 According to Chord Variation along Span	27
3.9.4 Variable Planforms	28
3.9.5 Wing-body Combinations	29
3.10 Selection Criteria to Use NACA 4412	30

	<b>Page</b>
<b>CHAPTER-4 MATHEMATICAL MODELING</b>	<b>31-40</b>
4.1 Determination of Pressure Coefficient	31
4.2 Estimation of Aerodynamic Coefficient	32
<b>CHAPTER-5 EXPERIMENTAL SETUP AND METHODOLOGY</b>	<b>41-48</b>
5.1 Design and Construction	41
5.1.1 Wing Models	41
5.1.2 Pressure Measuring Device	44
5.1.3 Fixture for Altering Angle of Attack	45
5.2 Experimental Setup	46
5.2.1 Wind Tunnel	46
5.2.2 Experimental Parameters	47
5.3 Methodology	48
<b>CHAPTER-6 RESULT AND DISCUSSIONS</b>	<b>49-79</b>
6.1 Analysis of Collected Data	49
6.2 Surface Pressure Distributions	50
6.2.1 Pressure Distributions at $-4^\circ$ AOA	50
6.2.2 Pressure Distributions at $0^\circ$ AOA	54
6.2.3 Pressure Distributions at $4^\circ$ AOA	58
6.2.4 Pressure Distributions at $8^\circ$ AOA	61
6.2.5 Pressure Distributions at $12^\circ$ AOA	65
6.2.6 Pressure Distributions at $16^\circ$ AOA	68
6.2.7 Pressure Distributions at $20^\circ$ AOA	71
6.2.8 Pressure Distributions at $24^\circ$ AOA	73
6.3 Lift Characteristics	76

	<b>Page</b>
6.4 Drag Characteristics	77
6.5 Lift and Drag Ratio	78
<b>CHAPTER-7 CONCLUSIONS AND RECOMMENDATIONS</b>	<b>79-82</b>
7.1 Conclusion	79
7.2 Recommendations	81
<b>REFERENCES</b>	<b>83-88</b>
<b>APPENDIX-I</b> Calculated Values of Pressure Coefficient	<b>89-96</b>
<b>APPENDIX-II</b> Uncertainty Analysis	<b>97-98</b>

# LIST OF FIGURES

Figure No	Nomenclature	Page No
Figure 1.1	Typical Drag Breakdown by Components of Transport Aircraft	1
Figure 2.1	Coefficient of Lift and Drag VS AOA	5
Figure 2.2	Coefficient of Lift and Drag VS AOA and Lift Coefficient/ Drag Coefficient VS AOA	13
Figure 3.1	Wing and Aerofoil with Nomenclature	14
Figure 3.2	Geometric Features of a Typical Aircraft Wing	15
Figure 3.3	Geometric Features of an Aerofoil	16
Figure 3.4	Flow around an Aerofoil	17
Figure 3.5	Pressure Distribution around an Aerofoil	18
Figure 3.6	Aerodynamic Forces Acting on Aerofoil	18
Figure 3.7	Aerodynamic Characteristics of Aircraft Wing	19
Figure 3.8	Variation of Aerodynamic Characteristics with Angle of Attack	20
Figure 3.9	Graphs of Different Parameters of Aerofoil	22

<b>Figure No</b>	<b>Nomenclature</b>	<b>Page No</b>
Figure 3.10	NACA Aerofoil Coordinates	23
Figure 3.11	Wing Geometric parameters	24
Figure 3.12	Wing Planforms according to Aspect Ratio	26
Figure 3.13	Wing Planforms according to Wing Sweep	26
Figure 3.14	Wing Planforms according to Chord Variation	28
Figure 3.15	Variable Wing Planforms	29
Figure 3.16	Wing Planforms due to Wing –body Combinations	29
Figure 4.1	Pressure Distribution over an Aerofoil’s Surface in Terms of $C_p$	32
Figure 4.2	Illustration of Pressure and Shear Stress on Aerofoil Surface	33
Figure 4.3	Resultant Aerodynamic Force and Its Components	34
Figure 4.4	Nomenclature for Integration of $p$ and $\tau$ Distributions	35
Figure 4.5	Aerodynamic Force on an Element of the Body Surface	35
Figure 4.6	Reference Area and Length for Airplane	38
Figure 4.7	Geometrical Relationship of Differential Lengths	38
Figure 4.8	Paneling of the Wing Surface	40
Figure 5.1	Experimental Wing Models	42
Figure 5.2	Multi-tube Manometer	45
Figure 5.2	AOA Altering Fixture	45

<b>Figure No</b>	<b>Nomenclature</b>	<b>Page No</b>
Figure 5.3	Schematic Diagram of the Wind Tunnel at BUET's Turbulence Lab	46
Figure 5.4	Photograph of Experimental Setup	47
Figure 6.1	$C_p$ Distribution of Segment-A at $\alpha = -4^\circ$	51
Figure 6.2	$C_p$ Distribution of Segment-B at $\alpha = -4^\circ$	52
Figure 6.3	$C_p$ Distribution of Segment-C at $\alpha = -4^\circ$	53
Figure 6.4	$C_p$ Distribution of Segment-D at $\alpha = -4^\circ$	54
Figure 6.5	$C_p$ Distribution of Segment-A at $\alpha = 0^\circ$	55
Figure 6.6	$C_p$ Distribution of Segment-B at $\alpha = 0^\circ$	56
Figure 6.7	$C_p$ Distribution of Segment-C at $\alpha = 0^\circ$	57
Figure 6.8	$C_p$ Distribution of Segment-D at $\alpha = 0^\circ$	58
Figure 6.9	$C_p$ Distribution of Segment-A at $\alpha = 4^\circ$	59
Figure 6.10	$C_p$ Distribution of Segment-B at $\alpha = 4^\circ$	60
Figure 6.11	$C_p$ Distribution of Segment-C at $\alpha = 4^\circ$	60
Figure 6.12	$C_p$ Distribution of Segment-D at $\alpha = 4^\circ$	61
Figure 6.13	$C_p$ Distribution of Segment-A at $\alpha = 8^\circ$	62
Figure 6.14	$C_p$ Distribution of Segment-B at $\alpha = 8^\circ$	63
Figure 6.15	$C_p$ Distribution of Segment-C at $\alpha = 8^\circ$	64
Figure 6.16	$C_p$ Distribution of Segment-D at $\alpha = 8^\circ$	64
Figure 6.17	$C_p$ Distribution of Segment-A at $\alpha = 12^\circ$	65
Figure 6.18	$C_p$ Distribution of Segment-B at $\alpha = 12^\circ$	66

<b>Figure No</b>	<b>Nomenclature</b>	<b>Page No</b>
Figure 6.19	$C_p$ Distribution of Segment-C at $\alpha = 12^\circ$	67
Figure 6.20	$C_p$ Distribution of Segment-D at $\alpha = 12^\circ$	68
Figure 6.21	$C_p$ Distribution of Segment-A at $\alpha = 16^\circ$	69
Figure 6.22	$C_p$ Distribution of Segment-B at $\alpha = 16^\circ$	69
Figure 6.23	$C_p$ Distribution of Segment-C at $\alpha = 16^\circ$	70
Figure 6.24	$C_p$ Distribution of Segment-D at $\alpha = 16^\circ$	70
Figure 6.25	$C_p$ Distribution of Segment-A at $\alpha = 20^\circ$	71
Figure 6.26	$C_p$ Distribution of Segment-B at $\alpha = 20^\circ$	72
Figure 6.27	$C_p$ Distribution of Segment-C at $\alpha = 20^\circ$	72
Figure 6.28	$C_p$ Distribution of Segment-D at $\alpha = 20^\circ$	73
Figure 6.29	$C_p$ Distribution of Segment-A at $\alpha = 24^\circ$	74
Figure 6.30	$C_p$ Distribution of Segment-B at $\alpha = 24^\circ$	74
Figure 6.31	$C_p$ Distribution of Segment-C at $\alpha = 24^\circ$	75
Figure 6.32	$C_p$ Distribution of Segment-D at $\alpha = 24^\circ$	75
Figure 6.33	Variation of Lift Coefficient with Angle of Attack	76
Figure 6.34	Variation of Drag Coefficient with Angle of Attack	77
Figure 6.35	Variation of Lift to Drag Ratio with Angle of Attack	79

# LIST OF TABLES



<b>Table No</b>	<b>Nomenclature</b>	<b>Page No</b>
Table 1	Dimensions of Five Models	44
Table 2	Calculated Values of Pressure Coefficient at $-4^\circ$ Angle of Attack	90
Table 3	Calculated Values of Pressure Coefficient at $0^\circ$ Angle of Attack	91
Table 4	Calculated Values of Pressure Coefficient at $4^\circ$ Angle of Attack	92
Table 5	Calculated Values of Pressure Coefficient at $8^\circ$ Angle of Attack	93
Table 6	Calculated Values of Pressure Coefficient at $12^\circ$ Angle of Attack	94
Table 7	Calculated Values of Pressure Coefficient at $16^\circ$ Angle of Attack	95
Table 8	Calculated Values of Pressure Coefficient at $20^\circ$ Angle of Attack	96
Table 9	Calculated Values of Pressure Coefficient at $24^\circ$ Angle of Attack	97



# NOMENCLATURE

A	Axial Force
b	Wing Span
C	Wing Chord
$C_D$	Coefficient of Drag
$C_L$	Coefficient of Lift
$C_p$	Coefficient of Pressure
$C_{pu}$	Upper Surface Pressure Coefficient
$C_{pl}$	Lower Surface Pressure Coefficient
D	Drag Force
L	Lift Force
L/D	Lift to Drag Ratio
M	Model
N	Normal Force
p	Pressure
$P_\infty$	Free Stream Pressure
$R_N$	Reynolds Number
S	Wing Surface Area
$U_\infty$	Free Stream Velocity of Air
v	Velocity of Air
$\alpha$	Angle of Attack
$\tau$	Shear Stress
p or $p_a$	Density of Air
$p_w$	Density of Water
$\mu_a$	Absolute Viscosity of Air
$\mu_w$	Absolute Viscosity of Water
$\frac{1}{2} \rho U_\infty^2$	Free Stream Dynamic Pressure

## INTRODUCTION

### 1.1 General

The primary lifting surface of an aircraft is its wing. The wings are the airfoils that generate the lift necessary to get and keep, an aircraft off the ground. Airplanes fly when the movement of air across their wings creates an upward force on the wings (and thus the rest of the plane) that is greater than the force of gravity pulling the plane toward the earth. The wing planform is the silhouette of the wing when viewed from above or below. The shape/geometry can be varied span wise to search better performance. The effects of wing shape/size are crucial to aerodynamic characteristics on which the efficiency/performance of aircraft depends. Therefore, researches on different wing shapes/geometries are still on throughout the world to explore the maximum possible lift and minimum possible drag.

### 1.2 Background

In aerodynamics, the main source of the airplane drag is related with the wing. Around two-thirds of the total drag of typical transport aircraft at cruise conditions is produced by the wing [1]. The drag stems from the vortices shed by an aircraft's wings, which causes the local relative wind downward (an effect known as downwash) and generate a component of the local lift force in the direction of the free stream. The strength of this induced drag is proportional to the spacing and radii of these vortices. By designing wings, which force the vortices farther apart and at the same time create vortices with larger core radii, it may significantly reduce the amount of drag the aircraft induces. Airplanes which experience less drag require less power and therefore less fuel to fly an arbitrary distance, thus making flight, commercial, more efficient and less costly [2]. So, an efficient wing plays a vital role to make the flight safe, smooth, effective and less costly.

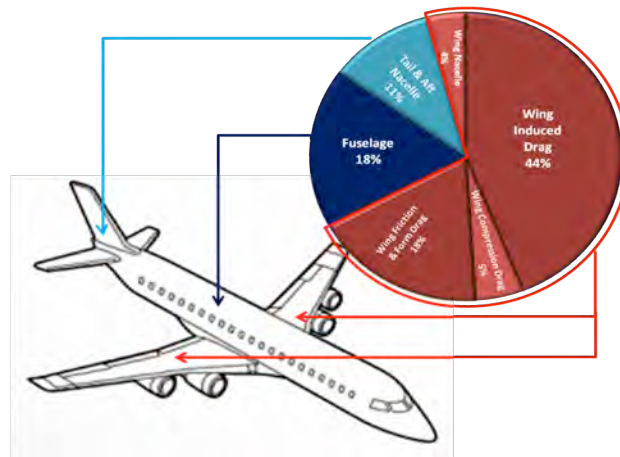


**Figure 1.1: Typical Drag Breakdown by Components of Transport Aircraft [1]**

### 1.3 Problem Statement

The aerofoil is the heart of an airplane it affects the cruise speed, takeoff and landing distances, stall speed, handling qualities (specially near the stall), and overall aerodynamic efficiency during all phases of flight. When wing is generating lift, it has a reduced pressure on the upper surface and an increased pressure on the lower surface. For a wing of finite span, the air on the upper surface flows inward and air below the under-surface flows outward. For this reason, there is a continual spilling of the air round the wing tip from the bottom surface of the wing to the upper surface. These two airflows meet at the trailing edge and cause wing-tip vortices. If there is a wing of infinite aspect ratio, the air flows over the wing surface without any inward or outward deflection, and therefore no wing-tip vortices, no induced drag. But such a thing is impossible in practical flight, and for this reason the effective aspect ratio is increased as large as is practicable by changing chord and length. The extension of wingspan permits the lowering of drag but this comes at a cost of increasing the strength of the wing and hence its weight.

The performance/efficiency of aircraft depends on the size and shape of wing. So, the researchers in the world are always trying to search the maximum possible lift and minimum possible drag on different wing/geometries. In this backdrop, this research will make an endeavor to find out the improved aerodynamic characteristics and performance through different planforms of wing. This study will make an endeavor to find the optimum performance of airfoils among the planforms considered. In aerodynamics, it is suggested that performance of airfoil depends on the size/shape of the wing as well as the wing planforms. Thereby, the expected outcome is to enable the aircraft designers and engineers to choose the appropriate wing planforms/shapes with a view to reducing the drag for efficient flying.

## **1.4 Motivation of the Research Work**

Literature review as discussed in chapter-2 reveals that researches on different airfoils and conventional wing geometries like rectangular, sweepback, tapered or, delta shapes have been carried out in many places in the world in an extensive way. But aerodynamic characteristics of Curved (inclined/slanted) edge wing planforms are yet to be explored. Thus, this study will make an endeavor to find the optimum performance of airfoils among the planforms considered through experimental method by wind-tunnel test.

## **1.5 Scope and Objectives of the Research**

The proposed experimental investigation is carried out in the wind tunnel to explore aerodynamic characteristics of four different wings of curved edge planforms; two having curve/slant at leading edge and the other two having curve/slant at trailing edge. Similar characteristics of a rectangular wing of equal span and surface area are also investigated in the same way for reference. At the end, the characteristics of the curved-edge wings are compared with that of the rectangular wing. So the specific objectives and scope of the research are as follows:

- a. To obtain the pressure distribution over the surfaces of different shapes of wing with NACA 4412 airfoils (rectangular, curved leading edges and curved trailing edges).
- b. To obtain the pressure distribution at different Angles of Attack of the wing models with a suitable fixture required during the experiment in the wind tunnel available at turbulence laboratory of BUET.
- c. To determine the aerodynamic characteristics (Coefficient of Pressure- $C_p$ , Coefficient of Lift- $C_L$ , Coefficient of Drag- $C_D$  and Lift to Drag Ratio-L/D) from static pressure distributions of the wing models.
- d. To analyze and compare all the above characteristics with the variation of Angle of Attack.

## **1.6 Organisation of the Thesis**

The dissertation is divided into seven chapters as follows:

- a. The first chapter covers the background information along with problem statement, scope and objectives of the research.
- b. The second chapter reviews the available literature related to the present research work.
- c. The third chapter presents the overview of the aerodynamics of wing.
- d. The fourth chapter describes theory of calculations and mathematical modeling in details.
- e. The fifth chapter illustrates the details of experimental set up and procedures.
- f. The sixth chapter presents the experimental results and discussion on the important aspects of the results.
- g. Finally, the seventh chapter concludes the overall research and recommends few scopes for further research related to the present outcome.

## LITERATURE REVIEW

The available literatures directly or indirectly related with the aerodynamics of wings and airfoils are focused on the following areas:

Hossain et al. [2] conducted an experimental analysis for the aerodynamic characteristics of rectangular wing with and without bird feather like winglets for different Reynolds Number. The experimental result shows 25~30% reduction in drag coefficient and 10~20% increase in lift coefficient by using bird feather like winglet at  $8^\circ$  angle of attack.

Ghods et al. [3] conducted an experimental analysis of NACA 2415 wing in wind tunnel where he shows Lift increases as the angle of attack increases between -5 and +17 degrees and at +17 degrees maximum lift is generated which is shown in Figure-2.1. If the angle of attack is increased any further, drag becomes the dominant factor and the wing enters the stall mode.

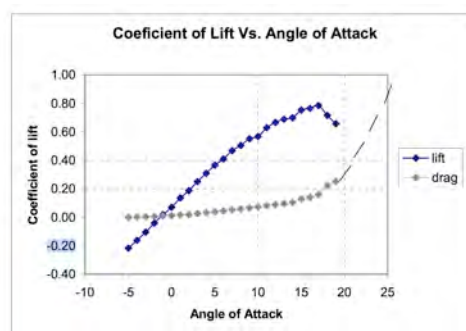


Figure 2.1: Coefficient of Lift and Drag VS AOA [3]

Dash [4] analyzed the NACA0012 wind turbine airfoil at various angles of attack, keeping the Reynolds number constant. The efficiency of the aerodynamic wind turbine is greatly influenced by the aerodynamic efficiency of the airfoil. In the present study NACA0012 airfoil is considered as a suitable wind turbine blade. The geometry and analysis was done using ANSYS-Fluent. Calculations were done for constant air velocity altering only the angle of attack. For the computational domain an unstructured mesh with sphere of influence and inflation was selected, taking care of the refinement of the grid near the airfoil in order to enclose the boundary layer approach. The CFD simulation results show close agreement with the results obtained from wind tunnel testing experiments, thus suggesting CFD analysis as a reliable alternative to experimental methods.

Mineck et al. [5] tested three planar, untwisted wings with the same elliptical chord but with different curvatures of the quarter-chord line. They found that the elliptical wing with the unswept quarter-chord line has the lowest lifting efficiency, the elliptical wing with the unswept trailing edge has the highest lifting efficiency and the crescent-shaped wing has efficiency in between.

Recktenwald [6] tested a circular planform non-spinning body with an airfoil section configuration developed and produced by Geobat Flying Saucer Aviation Inc. in the Auburn University wind tunnel facility. For comparison purpose, a Cessna 172 model was also tested. The author found that the lift curve slope of the Geobat was less than that of Cessna 172 but displayed better stall characteristics.

Wakayama [7] studied and presented basic results from wing planform optimization for minimum drag with constraints on structural weight and maximum lift. Analyses in each of these disciplines were developed and integrated to yield successful optimization of wing planform shape. Results demonstrated the importance of weight constraints, compressibility drag, maximum lift, and static aero-elasticity on wing shape, and the necessity of modeling these effects to achieve realistic optimized planforms.

Paulo et al. [8] studied Multi-disciplinary Design and Optimization (MDO) of a transport aircraft wing. They developed a mathematical model of the MDO framework using MATLAB which includes the calculation of aircraft drag polar (based on geometrical characteristics), stability derivatives and performance for some flight phases.

Dwivedi et al. [9] adopted a simple approach for experiment on aerodynamic static stability analysis of different types of wing shapes. They tested the reduced scale size wings of different shapes like rectangular, rectangular with curved tip, tapered, tapered with curved tip etc. in low speed subsonic wind tunnel at different air speeds and different angles of attack. The authors found that the tapered wing with curved tip was the most stable at different speeds and ranges of working angles of attack.

Aerodynamic characteristics analyses for different airfoils have also been conducted at different corners of the world like Mahmud [10] analyzed the effectiveness of an airfoil with bi-camber surface. Kandwal et al. [11] presented a computational method to deduce the lift and drag properties, which can reduce the dependency on wind tunnel testing. The study is done on air flow over a two-dimensional NACA 4412 Airfoil using ANSYS FLUENT (version 12.0.16), to obtain the surface pressure distribution, from which drag and lift were calculated using integral equations of pressure over finite surface areas. In addition, the drag and lift coefficients were also determined. The CFD simulation results show close agreement with those of the experiments, thus suggesting a reliable alternative to experimental method in determining drag and lift. Robert [12] studied the variation of pressure distribution over an airfoil with Reynolds Number. Sharma [13] analyzed the flow behaviour around an airfoil body.

Wells [14] made an effort to verify the high performance characteristics of the co-flow jet (CFJ) airfoil experimentally. The CFJ utilizes tangentially injected air at the leading edge and tangentially removed air at the trailing edge to increase lift and stall margin and also to decrease drag. The mass flow rates of the injection and



suction are equal, so there is a zero net mass flow rate. Two airfoils were tested at the University of Florida. One airfoil had an injection slot size of 0.65% chord length and the other had an injection slot size twice as large or 1.31% chord length. Both airfoils had a suction slot size of 1.96% chord length. The smaller injection slot size performed superior for increased lift and stall margin, whereas the larger injection slot size performed superior for decreased drag. The smaller injection slot airfoil had an increase in maximum lift of 113% to 220% and an increase in stall margin of 100% to 132% when compared to the baseline airfoil.

Demasi [15] presented an original method of predicting the minimum induced drag conditions in conventional or innovative lifting systems. The procedure shown is based on the lifting line theories and the small perturbation acceleration potential. Under the hypothesis of linearity and rigid wake aligned with the free stream, the optimal condition was formulated using the Euler-Lagrange integral equation under the conditions of fixed total lifting force and wing span. The minimum induced drag problem was then formulated and solved numerically and analytically when possible. Classical configurations and non-planar lifting systems were extensively analyzed. In particular, the configurations examined were: Classical cantilever wing and biplane, Circular annular wing, Elliptical annular wing, Elliptical lifting arcs. For each system, the optimal circulation distribution and the minimum induced drag were calculated.

Ismail [16] presented a preliminary analytic method for estimation of load and pressure distributions on low speed wings with flow separation and wake rollup phenomena. A higher order vortex panel method was coupled with the numerical lifting line theory by means of iterative procedure including models of separation and wake rollup. The presented method was investigated through a number of test cases with different types of wing sections (NACA 0012 and GA (W)-1) for different aspect ratios and angles of attack, the results include the lift and drag curves, lift and pressure distributions along the wing span taking into the consideration the effect of the angles of attack and the aspect ratios on the wake rollup. The pressure distribution on the wings showed that there is a region of

constant pressure on the upper surface of the wings near the trailing edge in the middle of the wing, also there is a region of flow separation on the upper surface of the wings.

McArthur [17] studied three airfoil shapes at Reynolds numbers of 1 and  $2 \times 10^4$ ; a flat plate airfoil, a circular arc cambered airfoil, and the Eppler 387 airfoil. Lift and drag force measurements were made on both 2D and 3D conditions, with the 3D wings having an aspect ratio of 6, and the 2D condition being approximated by placing end plates at the wing tips. This study showed that lifting line theory could be applied when there were no sudden changes in the slope of the force curves.

Hassan et al. [18] investigated the aerodynamic characteristics of forward swept wing theoretically and experimentally. Theoretically, a computer program was developed to predict the pressure distribution about surface of the wing using three dimensional Low Order Subsonic Panel method. The aerodynamic coefficients of the wing were calculated from the pressure distribution which gained from tangential velocities experimentally. Tests were carried out by designing and manufacturing a wing model with special arrangement for pressure tapping suitable for wind tunnel testing. The entire wing was rotated about an axis in the plane of symmetry and normal to the chord to produce different sweep and incidence angles for wing by using rotating mechanism. Wind tunnel test was carried out at ( $U_\infty=33.23\text{m/s}$ ) for different swept angles and angles of attack. Comparisons were made between the predicted and experimental results. It was clear from the investigation that the lift and drag characteristics for the forward swept wing were less in values compared with the swept back wing. Therefore, a forward swept wing can fly at higher speed corresponding to a pressure distribution associated for lower speed.

Ahmed [19] studied the flow characteristics over a NACA 4415 airfoil experimentally at a Reynolds number of  $2.4 \times 10^5$  by varying the angle of attack from 0 to  $10^\circ$  and ground clearance of the trailing edge from five percent of chord to

eighty percent. The pressure distribution on the airfoil surface was obtained, velocity survey over the surface was performed, wake region was explored and lift and drag forces were measured. A strong suction effect was observed on the lower surface for angles of attack of 0 and 2.5° at small ground clearances. Increased suction was observed on the upper surface for small ground clearances. For the angle of attack of 10°, the flow on the upper surface could not withstand the adverse pressure gradient at small ground clearances and separated from the surface resulting in a loss of lift and an increase in drag.

Alam [20] made an effort to determine the interference effect of different biplane configurations. NACA 0024 symmetric airfoil with chord length of 100mm was used for four biplane configurations. The interference effects were analyzed by varying the distance between the airfoils and the angle of attack numerically with the help of CFD software. The interference effect is more for biplane configuration at 0.40 of chord length and reduces when the distance between the airfoils increases.

Walter [21] investigated the effect of ground proximity on the lift, drag and moment coefficients of inverted, two-dimensional airfoils. The purpose of the study was to examine the effect of ground proximity on airfoils post stall, in an effort to evaluate the use of active aerodynamics to increase the performance of a race car. The airfoils were tested at angles of attack ranging from 0°~135°. The tests were performed at a Reynolds number of  $2.16 \times 10^5$  based on chord length. Forces were calculated via the use of pressure taps along the centre line of the airfoils. The RMIT Industrial Wind Tunnel (IWT) was used for the testing. The IWT was chosen as it would allow enough height to reduce blockage effect caused by the airfoils when at high angles of incidence. The walls of the tunnel were pressure tapped to allow monitoring of the pressure gradient along the tunnel. The results show a delay in the stall of the airfoils tested with reduced ground clearance. Two of the airfoils tested showed a decrease in  $C_L$  with decreasing ground clearance; the third showed an increase. The  $C_D$  of the airfoils post-stall decreased with reduced

ground clearance. Decreasing ground clearance was found to reduce pitch moment variation of the aerofoils with varied angle of attack.

Al-Kayiem et al. [22] investigated the wing-ground collision experimentally and numerically. The investigation involved a series of wind tunnel measurements of a 2-D wing model having NACA 4412 airfoil section. An experimental set up has been designed and constructed to simulate the collision phenomena in a low speed wind tunnel. The investigations were carried out at different Reynolds numbers ranging from  $10^5$  to  $4 \times 10^5$ , various model heights to chord ratios ranging from 0.1 to 1, and different angles of attack ranging from  $-4^\circ$  to  $20^\circ$ . Numerical simulation of the wing-ground collision was carried out using FLUENT software. The results showed that the aerodynamic characteristics were considerably influenced when the wing is close to the ground, mainly at angles of attack  $4^\circ$  to  $8^\circ$ . The take-off and landing speeds were found to be very influencing parameters on the aerodynamic characteristics, mainly the lift of the wing in collision status.

Janiszewska [23] conducted a comprehensive experimental investigation on a LS (1)-0421MOD airfoil model. Surface pressure distributions were obtained for 2D baseline and 3D configurations under clean and surface grit conditions. Several vortex generator configurations were evaluated. The data were taken for steady state and unsteady conditions. The steady state data included angles of attack from  $0^\circ$  to  $30^\circ$  and Reynolds numbers of  $10^6$ . The unsteady conditions were simulated using a face cam that provided a sinusoidal angle of attack variation with  $10^\circ$  amplitude for three frequencies of 0.6 and 1.8 Hz at mean angles of attack of  $8^\circ$ ,  $14^\circ$  and  $20^\circ$ . Surface pressure data were obtained from six span wise stations, which were integrated to local coefficients. The maximum 2D lift coefficient obtained for the 1.0 million Reynolds number was 1.58 at  $14.4^\circ$  angle of attack. For the 3D case the maximum lift coefficient at the wall was 1.58 at  $19.5^\circ$  and at the tip was 1.20 at  $18.3^\circ$ . The results showed that the application of the grit roughness reduces the maximum lift coefficients in all configurations by as much as 50%. The Flat and Curled vortex generators increased the maximum lift coefficient for both the 3D tip and wall stations, up to 1.6 and 1.92, respectively. The unsteady maximum lift

coefficients were always higher than those for the steady state up to 60% and showed, generally, large hysteresis loops. The hysteresis loops were smaller for the 3D wing configuration due to the tip vortex influence, therefore smallest hysteresis loops occurred at the tip. The Flat and Curled vortex generators removed the hysteresis loops for all frequencies at 14° mean angle and significantly reduced the minimum value of the pitching moment and the pressure drag at stall.

Arora [24] studied aerodynamic characteristics for the aircraft model with NACA wing No. 65-3-218 using subsonic wind tunnel of 1000 mm x 1000 mm rectangular test section. Tests were conducted on the aircraft model with and without winglet of two configurations at Reynolds numbers  $1.7 \times 10^5$ ,  $2.1 \times 10^5$ , and  $2.5 \times 10^5$ . Lift curve slope increased more with the addition of the elliptical winglet and at the same time the drag decreased more for the aircraft model with elliptical shaped winglet giving an edge over the aircraft model without winglet as far as lift to drag ratio for the elliptical winglet is considered. Elliptical winglet of configuration 2 (winglet inclination 60°) showed, overall, the best performance, giving about 6% increase in lift curve slope as compared to without winglet configuration and it also provided the best lift to drag ratio.

Mashud [25] introduced a flow separation control mechanism to improve the aerodynamic characteristics of an airfoil. Control of flow separation over an airfoil which experiences a laminar separation bubble for a low Reynolds number was experimentally simulated under the effects of suction and injection. To perform the experiment a NACA 4215 airfoil profile was chosen to make the wing model. The wing model with control mechanism was tested in a subsonic wind tunnel for different angles of attack and different suction-injection frequency. The wing performance was significantly improved due to control of flow separation by suction and injection. It was also found that the lift increased about 14% and drag reduced about 23% at 8° angle of attack.

Sahin [26] studied numerical and experimentally analysis lift and drag performances of NACA 0015 airfoil at different attack angle at low Reynolds numbers (Re) by

measuring the forces every two degrees from 0° to 20°. The experiment test was conducted in low speed wind tunnel, and the numerical analysis was performed using CFD program which was FLUENT. The results obtained from experiment and numerical were compared. In this study, stall angle depended on turbulent occurred behind airfoil was determined.

Nazmul [27] studied with three different planforms like wooden model with straight leading and trailing edge i.e. rectangular planform and another model with curved leading edge and straight trailing edge are prepared with NACA 4412 aerofoil in equal length (span) and surface area. Both the models are tested in a closed circuit wind tunnel at air speed of 85.35 kph (0.07 Mach) i.e. at Reynold's number  $1.82 \times 10^5$ . After analyzing the data, it is found that the curved leading edge wing planform is having higher lift coefficient and lower drag coefficient than the rectangular wing planform. The critical angle of attack of three planforms remain around 16° beyond which stall occurs.

National Aerofoil Data for NACA 4412 [28] aerofoil shows the critical angle of attack for rectangular planform around 16° AOA. The following figure-2.2 shows the Coefficient of Lift and Drag VS AOA and Lift Coefficient/ Drag Coefficient VS AOA :

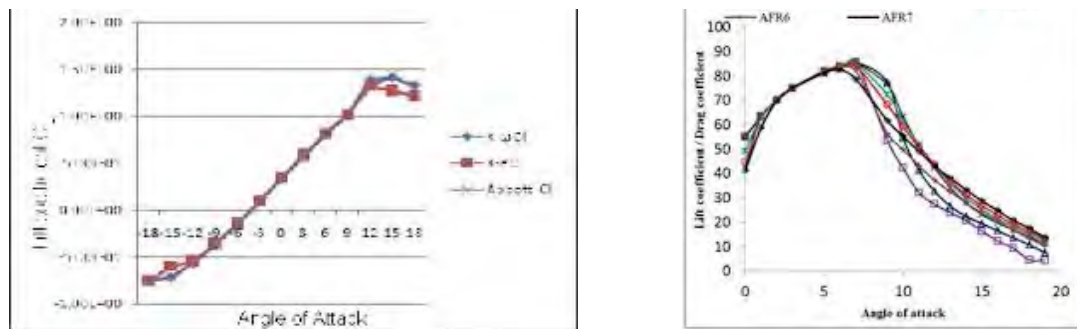


**Figure 2.2: Coefficient of Lift and Drag VS AOA and Lift Coefficient/Drag Coefficient VS AOA [28].**

## AN OVERVIEW OF WING AERODYNAMICS

### 3.1 Wing and Aerofoil

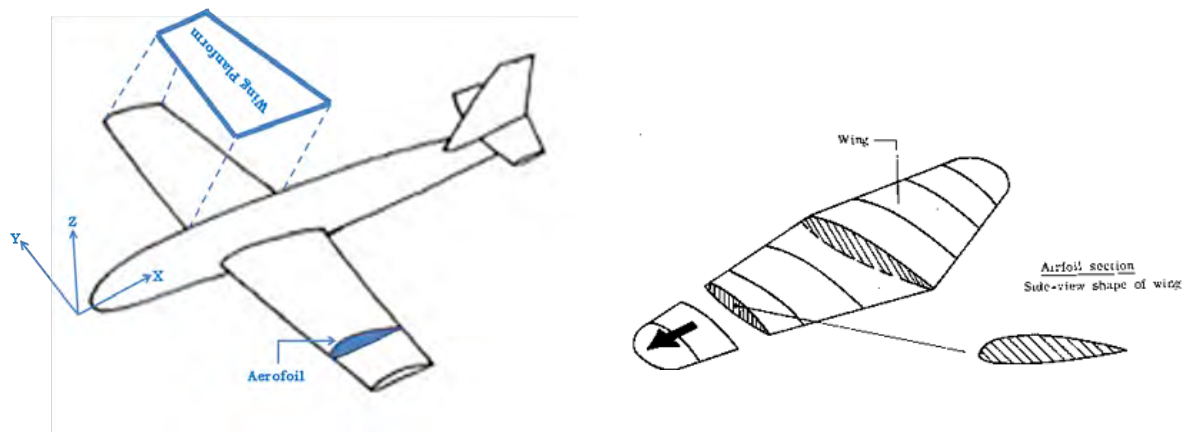
Wing is an aerodynamic structure that generates lift when comes into contact with moving air molecules i.e. wind. It may be considered as the most important component of an aircraft, since a fixed-wing aircraft is not able to fly without it. The main function of the wing of an aircraft is to generate lift force to make the flight possible in the air. This will be generated by a special wing cross section which is called airfoil. Wing is a three dimensional component, while the airfoil is two dimensional section as shown in Figure 3.1. The wing may have a constant or a non-constant cross-section across the wing [29]. Airfoils are basically replicas of wings that is much smaller in size. With the drag and lift values that are taken with airfoils, coefficients are calculated and since coefficients does not depend on wing size, larger wings can be produced.



Figure 3.1: Wing and Aerofoil with Nomenclature [29]

### 3.2 Aerodynamic Characteristics of Wing

The wing has a finite length called its wing span. If the wing is sliced with a plane parallel to the x-z plane of the aircraft, the intersection of the wing surfaces with that plane is called an airfoil. The wing is a 3D object, but it is usually treated as a set of two 2D geometric features; planform (x-y plane) and airfoil (x-z plane) as shown in Figure 3.2:



**Figure 3.2: Geometric Features of a Typical Aircraft Wing [29]**

### 3.3 General Features of an Aerofoil

Any section of the wing cut by a plane parallel to the aircraft xz plane is called an aerofoil. It usually looks like a positive cambered section that the thicker part is in front of the aerofoil.

#### 3.2.1 Terminologies

A typical aerofoil section is shown in Figure 3.2, where several geometric parameters are illustrated [30, 31].



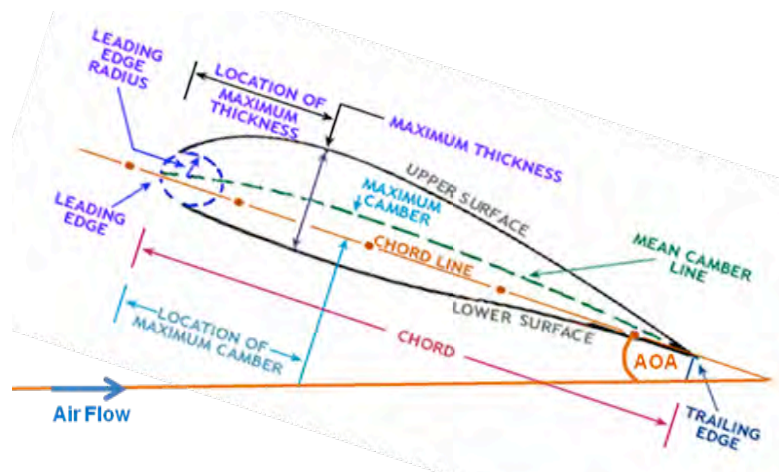


**Figure 3.3: Geometric Features of an Aerofoil [30,31].**

Airfoils have a leading edge and a trailing edge, and are usually designed with different top and bottom surface curvatures to promote the flow induced pressure difference that causes lift. The major feature of an aerofoil is the mean camber line, which is the locus of points halfway between the upper and lower surfaces. The most forward and rearward points of the mean camber line are the leading and trailing edges respectively. The straight line connecting the leading and trailing edges is the chord line of the aerofoil and the precise distance from the leading to the trailing edge measured along the chord line is called the chord of the aerofoil. The camber is the maximum distance between the mean camber line and chord line, measured perpendicular to the chord line. If the mean camber line in a straight line, the airfoil is referred to as symmetric airfoil, otherwise it is called cambered aerofoil. The camber of aerofoil is usually positive. The angle between the chord line and the direction of air flow is called the angle of attack.

### 3.2.2 NACA Aerofoils

The NACA airfoils are airfoil shapes for aircraft wings developed by the National Advisory Committee for Aeronautics (NACA). Airfoils are described and can be distinguished between each other by the numbers that follow the acronym NACA. There are six NACA families which are 4-Digit, 5-Digit, 6-Series, 7-Series, 8-Series and 16-Series. In NACA Four Digit Series, there are four digits that follow the acronym NACA and these 4 digits show 3 different properties of the airfoil. The first

family of airfoils designed in the above mentioned way is known as the NACA Four-Digit aerofoils. The explanation of the 4-digit NACA aerofoil is as follows [32, 33]:

- a. The first digit specifies the maximum camber in percentage of the chord.
- b. The second digit indicates the position of the maximum camber in tenths of chord.
- c. The last two digits provide the maximum thickness of the airfoil in percentage of chord.

For example, the NACA 4412 airfoil chosen for this research has a maximum thickness of 12% with a camber of 4% located 40% back from the airfoil leading edge.

### 3.4 Aerodynamic Forces Developed by Aerofoil

An airfoil-shaped body moved through the air will vary the static pressure on the top surface and on the bottom surface of the airfoil. In a positive cambered airfoil, the upper surface static pressure is less than ambient pressure, while the lower surface static pressure is higher than ambient pressure [29-32]. This is due to higher airspeed at upper surface and lower speed at lower surface of the airfoil as shown in Figure 3.3. As the airfoil angle of attack increases, the pressure difference between upper and lower surfaces will be higher as shown in Figure 3.4.

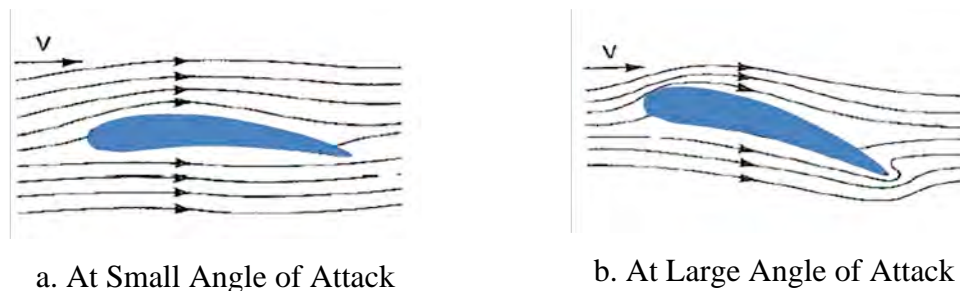


**Figure 3.4: Flow around an Aerofoil [29-32].**

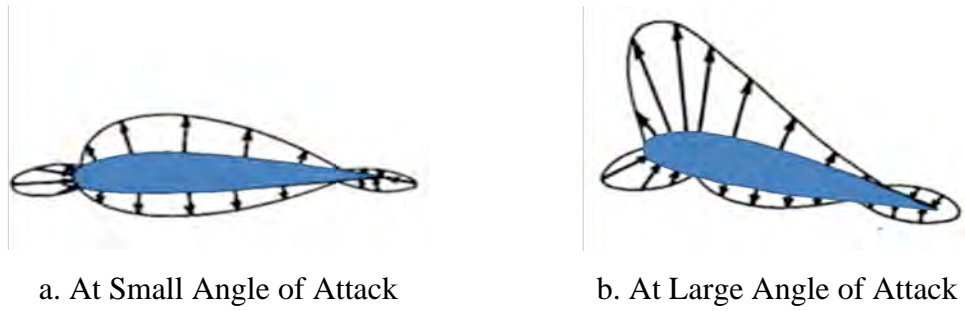


**Figure 3.5: Pressure Distribution around an Aerofoil [29-32].**

The force divided by the area is called pressure, so the aerodynamic force generated by an airfoil in a flow field may be calculated by multiplication of total pressure by area. The total pressure is simply determined by integration of pressure over the entire surface. The magnitude, location, and direction of this aerodynamic force are functions of airfoil geometry, angle of attack, flow properties, and airspeed relative to the airfoil. The location of this resultant force out of the integration is called center of pressure. The location of this center depends on aircraft speed and the airfoil's angle of attack.

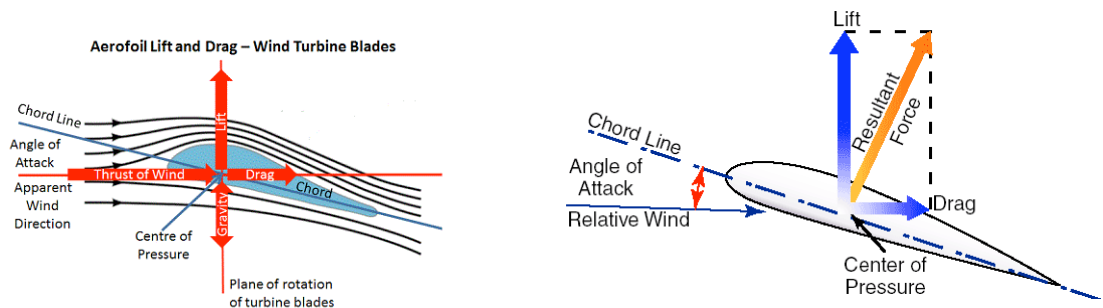


**Figure 3.6: Aerodynamic Forces Acting on Aerofoil [27,29].**

Thus, the pressure and shear stress distributions over the airfoil generate an aerodynamic force. However, this resultant force is replaced with two aerodynamic forces as shown by the vector in Figure 3.6. On the other word, the aerodynamic force can be resolved into two forces, perpendicular (lift) and parallel (drag) to the relative wind. The lift is always defined as the component of the aerodynamic force perpendicular to the relative wind. The drag is always defined as the component of the aerodynamic force parallel to the relative wind.

The flow of air through the surfaces of an aircraft produces the lifting force. The shape of the wings of an aircraft is designed to make the airflow through the surface to produce a lifting force in the most efficient manner. In addition to the lift, a force directly opposing the motion of the wing through the air is always present, which is called drag force. The angle between the relative wind and the chord line is the Angle of Attack of the airfoil.

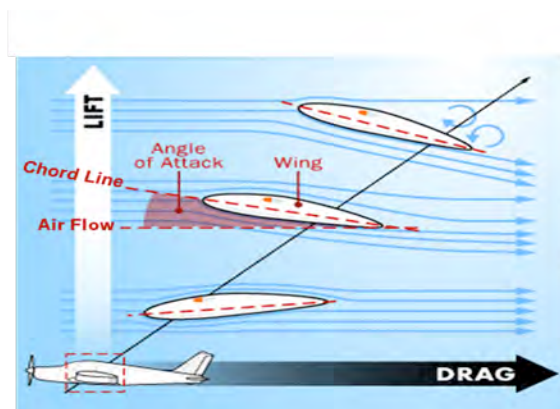


**Figure 3.7: Aerodynamic Characteristics of Aircraft Wing [27,29].**

The lift and drag forces developed by the wing vary with the change of angle of attack. The lift force increases almost linearly with angle of attack until a maximum value is reached, whereupon the wing is said to stall. The variation of the drag force with angle of attack is approximately parabolic. It is desirable for the wing to have the maximum lift and smallest possible drag i.e. the maximum possible lift to drag ratio.

The variation of all these aerodynamic characteristics (lift force, drag force and lift to drag ratio) with angle of attack for a typical aircraft are shown in Figure 1.4:

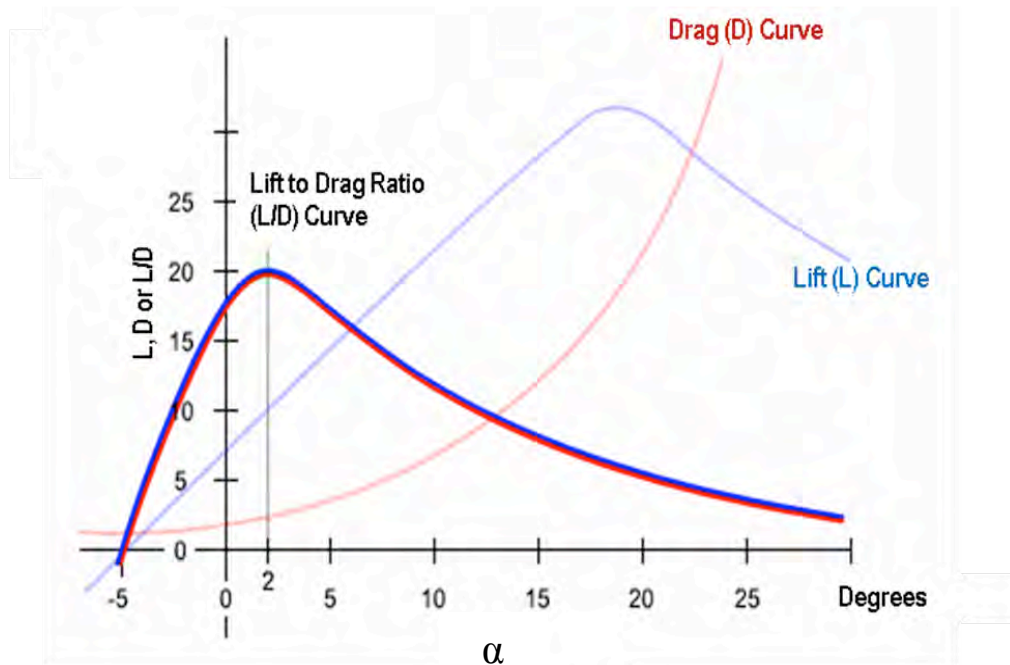


**Figure 3.8: Variation of Aerodynamic Characteristics with Angle of Attack [29].**

The aerodynamic characteristics of a wing depend on several parameters such as the wing's geometry, density of air, airspeed, the angle of attack etc. In this research, NACA 4412 aerofoil has been used for different planforms in the same airspeed, density of air and angle of attack with a view to search the effect of variation of wing planform/geometry on the aerodynamic characteristics. In aerodynamics, it is suggested that performance of airfoil depends on the size/shape of the wing as well as the wing planforms. Thereby, the expected outcome is to enable the aircraft designers and engineers to choose the appropriate wing planforms/shapes with a view to reducing the drag for efficient flying.

### 3.5 Lift and Drag Coefficient of Airfoil

The lift and drag generated by an airfoil are usually measured in a wind tunnel and published as coefficient which are dimensionless. These are mainly the variations of

non-dimensionalized lift and drag relative to angle of attack [33, 34]. Two aerodynamic forces (lift and drag) are usually non-dimensionalized by dividing them to appropriate parameters as follows:

$$\text{Lift Coefficient, } C_L = \frac{L}{\frac{1}{2}\rho U_\infty^2 A} \quad (3.1)$$

$$\text{Drag Coefficient, } C_D = \frac{D}{\frac{1}{2}\rho U_\infty^2 A} \quad (3.2)$$

Where,  $L$  and  $D$  are the lift force and drag force respectively.

$A$  is the Planform area=Chord x Span.

$U_\infty$  is the free stream air velocity.

$\frac{1}{2}\rho U_\infty^2$  is the dynamic pressure and  $\rho$  is the density of air

Another important parameter, the lift-to-drag ratio ( $L/D$ ) is the amount of lift generated by an airfoil, divided by the drag it creates by moving through the air. An airplane has a high  $L/D$  if it produces a large amount of lift or a small amount of drag. A higher or more favorable  $L/D$  is typically one of the major goals in aircraft design.

$$\text{Ratio} = \frac{\text{Lift}}{\text{Drag}} = \frac{L}{D} \quad (3.3)$$

Thus, the performance and characteristics of an airfoil may be evaluated by looking at the following graphs:

- a. The variations of lift coefficient ( $C_L$ ) with angle of attack ( $\alpha$ ).
- b. The variations of drag coefficient ( $C_D$ ) with angle of attack ( $\alpha$ ).
- c. The variations of drag coefficient ( $C_D$ ) with lift coefficient ( $C_L$ ).
- d. The variations of lift-to-drag ratio ( $L/D$ ) with angle of attack ( $\alpha$ ).

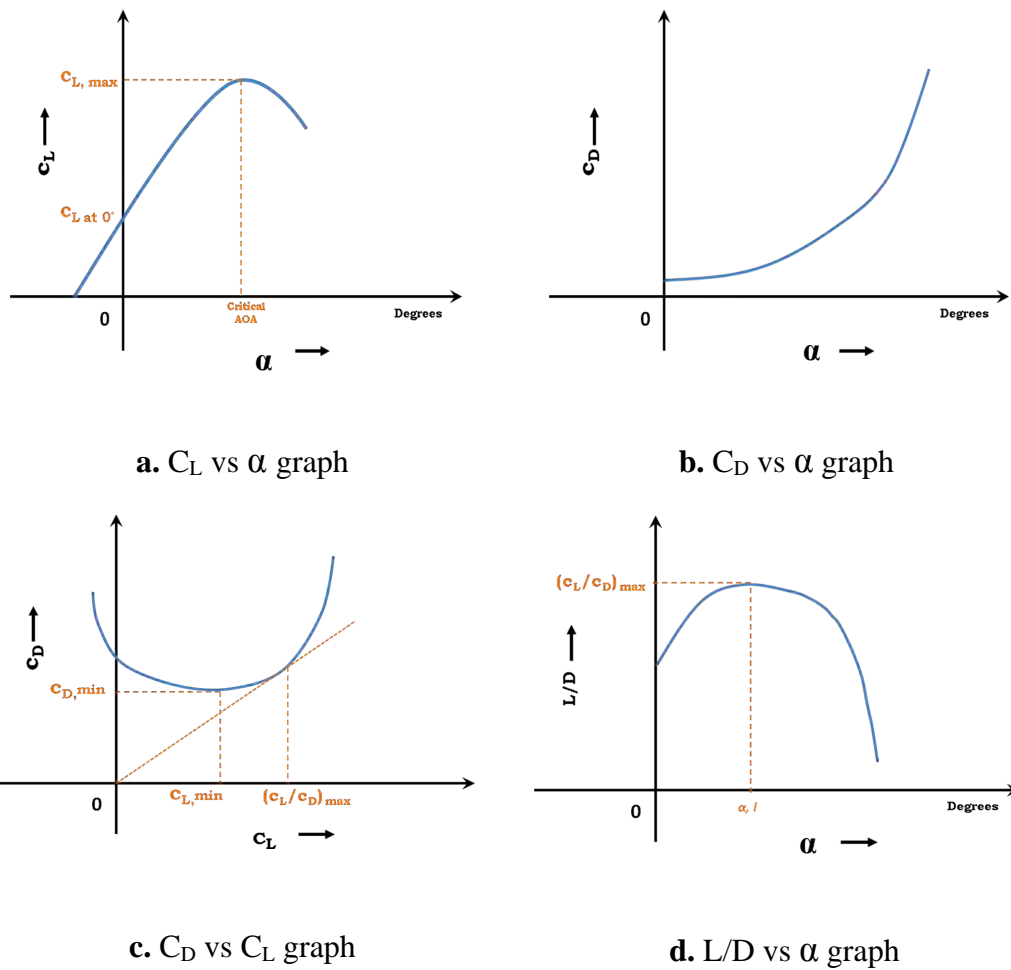


**Figure 3.9: Graphs of Different Parameters of Aerofoil [27,29]**

### 3.6 Aerofoil Data Sources

Selection of a proper airfoil is possible from the previously designed and published airfoil sections. Two reliable airfoil resources are NACA and Eppler. The details of Eppler airfoils have been published in [35]. NACA airfoils have been published in a book published by Abbott and Von Doenhoff [36]. Eppler airfoil names begin with the letter “E” followed by three numbers. In general, the Eppler airfoils are for very low Reynolds number, Wortman airfoils for low (sailplane-ish) Reynolds number, and the NASA Low-Speed airfoils (e.g. LS(1)-0413) and Mid Speed Airfoils e.g. MS(1)-0313) are for “moderate” Reynolds numbers [33].

### 3.7 Co-ordinates of NACA Airfoils

One of the most reliable resources and widely used data base is the airfoils developed by National Advisory Committee for Aeronautics, NACA (predecessor of NASA) in 1930s and 1940s. The Cambered airfoil sections of all NACA families are obtained by combining a mean line and a thickness distribution [33].

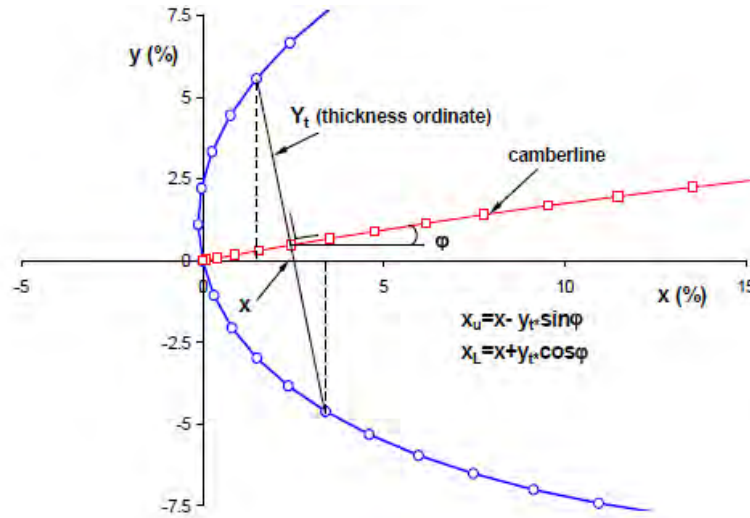


**Figure 3.10: NACA Aerofoil Co-ordinates [33].**

The abscissas, ordinates and slopes of the mean line are designated as  $x_c$ ,  $y_c$  and  $\tan \theta$  respectively. If  $x_u$  and  $y_u$  represent the abscissa and ordinate of a typical point of the upper surface of the airfoil and  $y_t$  is the ordinate of the symmetrical thickness distribution at the chord wise position  $x$ , the upper and lower surface coordinates are given by the following relations ( $u$  denotes upper surface and  $l$  denotes lower surface):

$$x_u = x - y_t(x) \sin \theta \quad (3.4)$$

$$y_u = y_c(x) + y_t(x) \cos \theta \quad (3.5)$$

$$x_l = x + y_t(x) \sin \theta \quad (3.6)$$

$$y_l = y_c(x) - y_t(x) \cos \theta \quad (3.7)$$



Where,  $y_t(x)$  is the thickness function

$y_c(x)$  is the camber line function

$\tan\theta = \frac{dy_c}{dx}$  is the camber line slope

### 3.8 Geometric Parameters of Wing

Aircraft wing can be defined by several geometric parameters such as span (b), wing surface area or planform (S), root chord ( $C_{root}$ ), tip chord ( $C_{tip}$ ) etc. as shown in Figure 3.8. Other important parameters are discussed below:

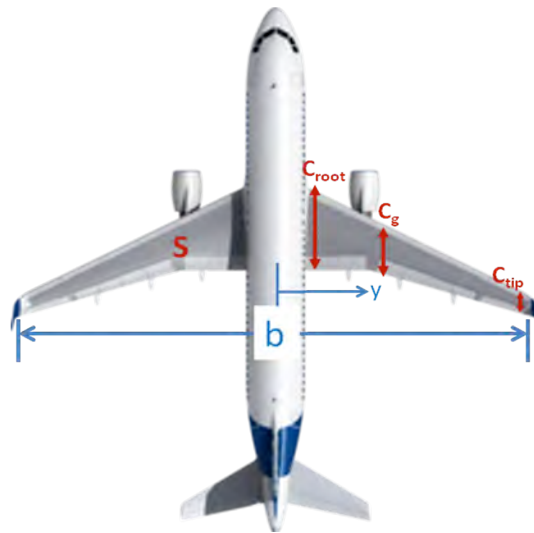


Figure 3.11: Wing Geometric Parameters [27,29].

#### 3.8.1 Mean Geometric Chord ( $C_g$ )

The mean geometric chord is the chord of a rectangular wing having the same span and the same area as the original wing. It can be found for any general wing in the following way:

$$C_g = \frac{\int_0^{b/2} c(y) dy}{\int_0^{b/2} dy} = \frac{2}{b} \int_0^{b/2} c(y) dy = \frac{S}{b} \quad (3.8)$$

### 3.8.2 Mean aerodynamic chord ( $C_{MAC}$ )

The mean aerodynamic chord is (loosely) the chord of a rectangular wing with the span, (not area) that has the same aerodynamic properties with regarding the pitching moment characteristics as the original wing. It can be found for any general wing in the following way:

$$C_{MAC} = \frac{\int_0^{b/2} [c(y)]^2 dy}{\int_0^{b/2} c(y) dy} = \frac{2}{s} \int_0^{b/2} [c(y)]^2 dy \quad (3.9)$$

### 3.8.3 Aspect ratio (AR)

The aspect ratio is the wing span divided by the mean geometric chord. It is a measure of how long and narrow a wing is. A square wing would have an aspect ratio of 1. Aspect ratio can be calculated in following ways:

$$AR = \frac{b}{C_g} = \frac{b^2}{S} \quad (3.10)$$

### 3.8.4 Taper ratio ( $\lambda$ )

It is the ratio of the tip chord to the root chord and is expressed as follows:

$$\lambda = \frac{C_{tip}}{C_{root}} \quad (3.11)$$

## 3.9 Familiarization with Different Wing Planforms

There are various types of wing planforms which are either successfully used in different aircrafts or still in the process of researches for viable uses. The planforms can be determined according to various factors as discussed below:

### 3.9.1 According to Aspect Ratio (AR)

The aspect ratio is the span divided by the mean or average chord. It is a measure of how long and slender the wing appears when seen from above or below.

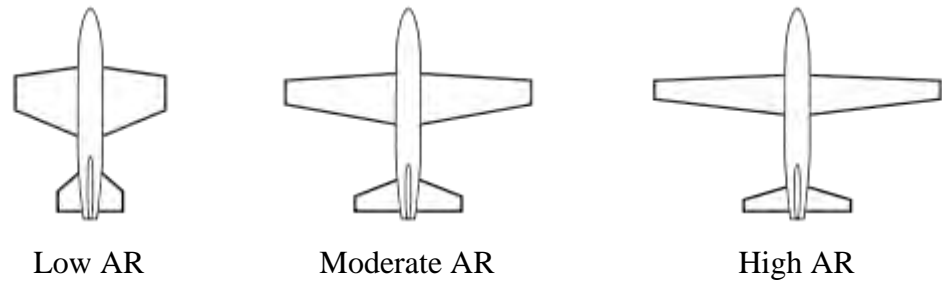


**Figure 3.12: Wing Planforms according to AR [29].**

### 3.9.2 According to Wing Sweep

Wings may be swept back or forward swept. A small degree of sweep is sometimes used to adjust the centre of lift when the wing cannot be attached in the ideal position for some reason, such as a pilot's visibility from the cockpit. Some wings may vary the wing sweep during flight:

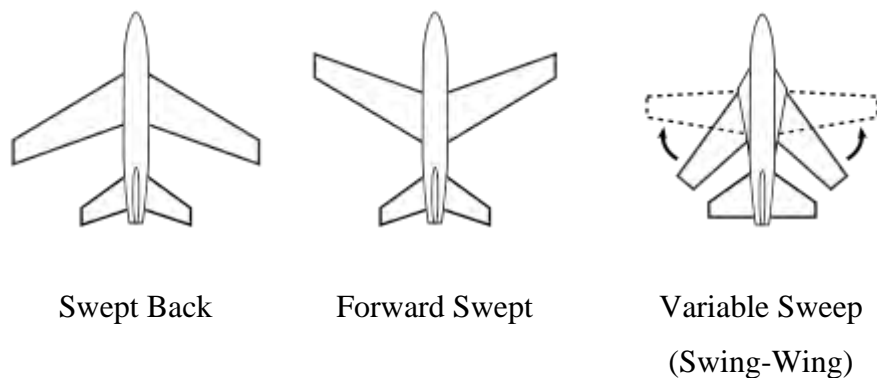
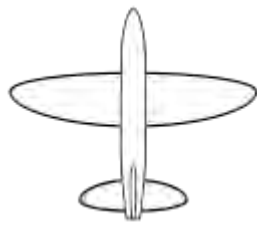


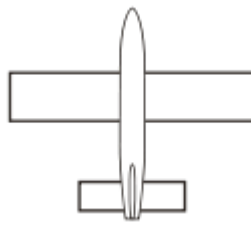
**Figure 3.13: Wing Planforms according to Wing Sweep [29].**

### 3.9.3 According to Chord Variation along Span

The wing chord may be varied along the span of the wing, for both structural and aerodynamic reasons. By varying the chord length along the span, the types of planforms are as follows:



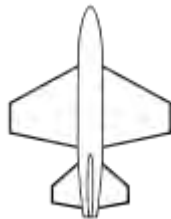
Elliptical



Constant chord



Tapered



Trapezoidal



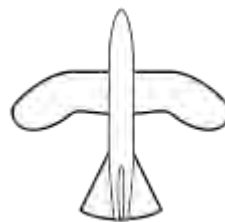
Reverse tapered



Compound Tapered



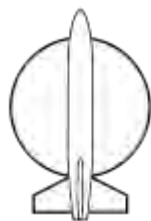
Constant chord,  
tapered outer



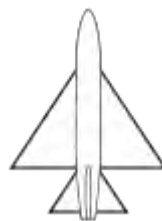
Birdlike



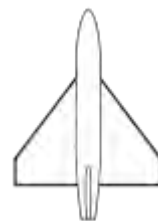
Batlike



Circular



Delta



Cropped Delta

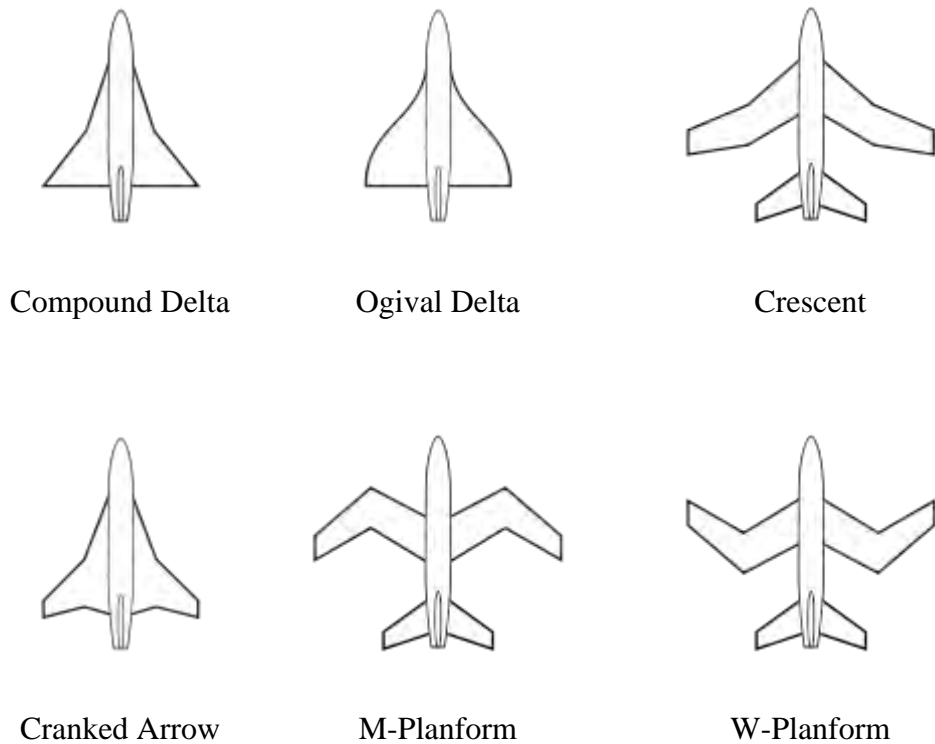


**Figure 3.14: Wing Planforms according to Chord Variation [29].**

### 3.9.4 Variable Planforms

There are also various types of wings having variable planforms such as telescopic wing, extending wing, bidirectional wing, folding wing etc. In telescoping wing, the outer section of wing telescopes over or within the inner section of wing, varying span, aspect ratio and wing area. In extending wing or expanding wing, part of the wing retracts into the main aircraft structure to reduce drag and low-altitude buffet for high-speed flight and is extended only for take-off, low-speed cruise and landing. Bi-directional wing is a proposed design in which a low-speed wing and a high-speed wing are laid across each other in the form of a cross. The aircraft would take off and land with the low-speed wing facing the airflow, then rotate a quarter-turn so that the high-speed wing faces the airflow for supersonic flight.

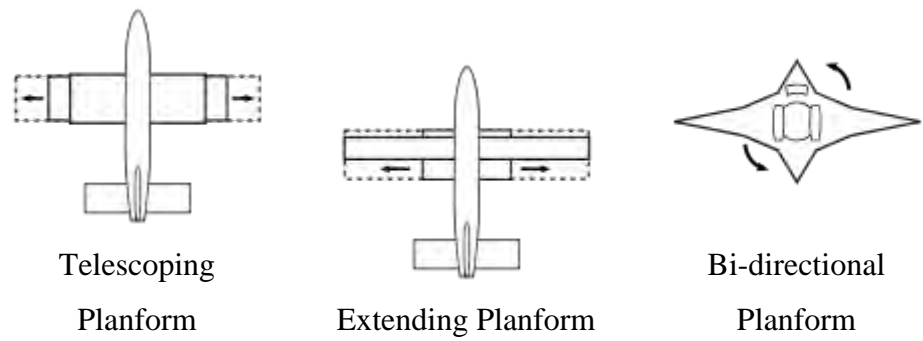


**Figure 3.15: Variable Wing Planforms [29].**

### 3.9.5 Wing-body Combinations

Some designs have no clear join between wing and fuselage (body of the aircraft) such as flying wing, blended wing body (BWB) and lifting body. In flying wing, the aircraft has no distinct fuselage or horizontal tail (although fins and pods, blisters, etc. may be present) whereas in BWB, a smooth transition occurs between wing and fuselage, with no hard dividing line. BWB design reduces wetted area and can also reduce interference between airflow over the wing root and any adjacent body and thus reduces drag. In case of lifting body, the aircraft lacks identifiable wings but relies on the fuselage (usually at high speeds or high angles of attack) to provide aerodynamic lift.

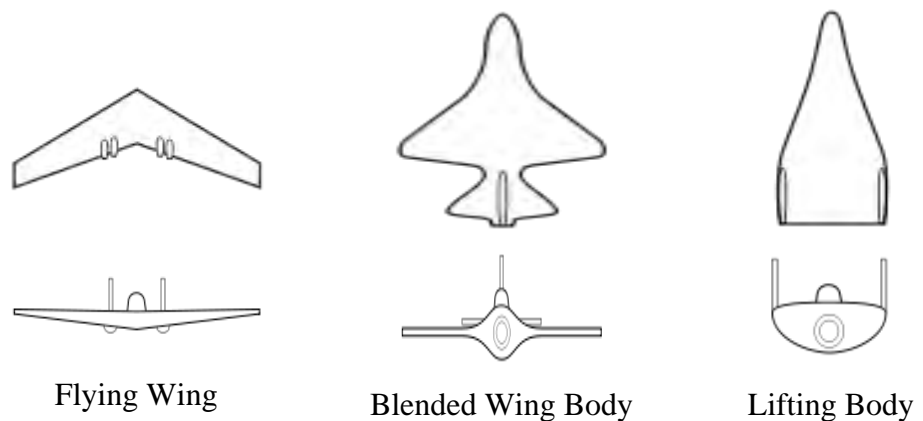


**Figure 3.16: Wing Planforms due to Wing-Body Combinations [29].**

### **3.10 Selection Criteria to Use NACA 4412**

Though there are various types of wings available in the world but the researcher is used NACA 4412 in this experiment because it has good stall properties and has low roughness effect. However, it has low lift coefficients and relatively high drag. These wing are mainly used for general aviation. Their lift and drag values differ from each other and vary with changing angle of attack. Thus, researcher wants to use different planforms of NACA 4412 to undergo various test in wind tunnel to observe their different aerodynamic characteristics. Thereby, the efficient planform model can be utilized in general aviation.

## MATHEMATICAL MODELING

### 4.1 Determination of Pressure Coefficient

The wind tunnel has a reference pressure tap located upstream of the test section and the pressure there is:

$$P_{\alpha} = \rho_{water} g (h_{atm} - h_{\alpha}) \quad (4.1)$$

From the Bernoulli relation, the corresponding velocity along a horizontal stream line is:

$$U_{\alpha} = \sqrt{\frac{2\rho_{water}(h_{atm} - h_{\alpha})}{\rho_{air}}} \quad (4.2)$$

The 32 pressure taps provide pressure values determined from the manometer as:

$$p_i = \rho_{water} g (h_{atm} - h_i) \quad (4.3)$$

The pressure coefficient ( $C_p$ ) is a dimensionless number which describes the relative pressures throughout a flow field in fluid dynamics. It is used in aerodynamics and hydrodynamics. Every point in a fluid flow field has its own unique pressure coefficient. It is very common to find pressures given in terms of  $C_p$  rather than the pressure itself. Figure 4.1 shows the pressure distribution at any point over the surface in terms of the pressure coefficient,  $C_p$ , which is defined as follows:

$$C_p = \frac{P_{Local} - P_{\alpha}}{\frac{1}{2} \rho U_{\alpha}^2} \quad (4.4)$$

Where,  $\frac{1}{2}\rho U_{\alpha}^2$  is the free stream dynamic pressure head



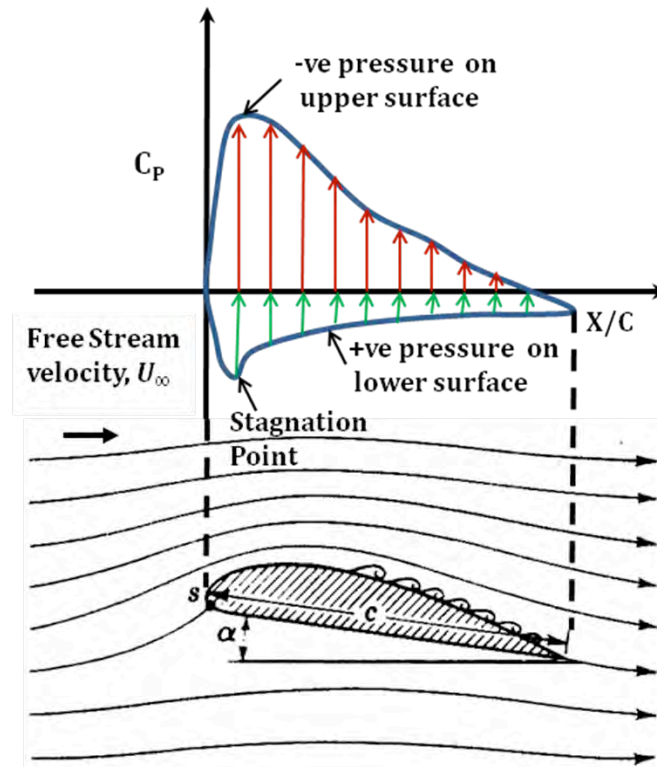


**Figure 4.1: Pressure Distribution over an Aerofoil's Surface in terms of  $C_p$  [29,39].**

Thus, surface pressure coefficient,  $C_p$  can be calculated from the static pressure by the following formula [29,39].

$$C_{p,i} = \frac{P_i - P_\alpha}{\frac{1}{2} \rho U_\alpha^2} \quad (4.5)$$

Where,  $P_i$  is the surface static pressure at any designated point  $i$ .

Values of  $C_p$  at any point over the aerofoil surface can be approximated from the corresponding boundary values by using the first order Lagrange interpolation and extrapolation:

$$c_p(x) = \frac{(x-x_1)}{(x_0-x_1)} c_{p,0} - \frac{(x-x_0)}{(x_1-x_0)} c_{p,1} \quad (4.6)$$

## 4.2 Estimation of Aerodynamic Force Coefficients from $C_p$

The aerodynamic forces and moments on the body are due to only two basic sources such as *the pressure distribution* over the body surface and *the Shear stress distribution* over the body surface [20]. No matter how complex the body shape may be, the aerodynamic forces and moments on the body are due entirely to the above two basic sources. The *only* mechanisms nature has for communicating a force to a body moving through a fluid are pressure and shear stress distributions on the body surface. Both pressure  $p$  and shear stress  $\tau$  have dimensions of force per unit area (pounds per square foot or newton's per square meter). As sketched in Figure 4.2,  $p$  acts *normal* to the surface, and  $\tau$  acts *tangential* to the surface. Shear stress is due to the "tugging action" on the surface, which is caused by friction between the body and the air.

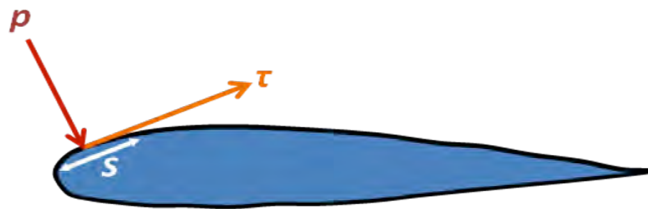


**Figure 4.2: Illustration of Pressure and shear Stress on Aerofoil Surface [20].**

The net effect of the  $p$  and  $\tau$  distributions integrated over the complete body surface is a resultant aerodynamic force  $R$  on the body. In turn, the resultant  $R$  can be split into components, two sets of which are shown in Figure 4.3. In Figure 4.3,  $U_\infty$  is the *relative wind*, defined as the flow velocity far ahead of the body. The flow far away from the body is called the *free stream*, and hence  $U_\infty$  is also called the free stream velocity. In Figure 4.3, by definition,

$$L = \text{lift} = \text{component of } R \text{ perpendicular to } U_\infty$$

$$D = \text{drag} = \text{component of } R \text{ parallel to } U_\infty$$

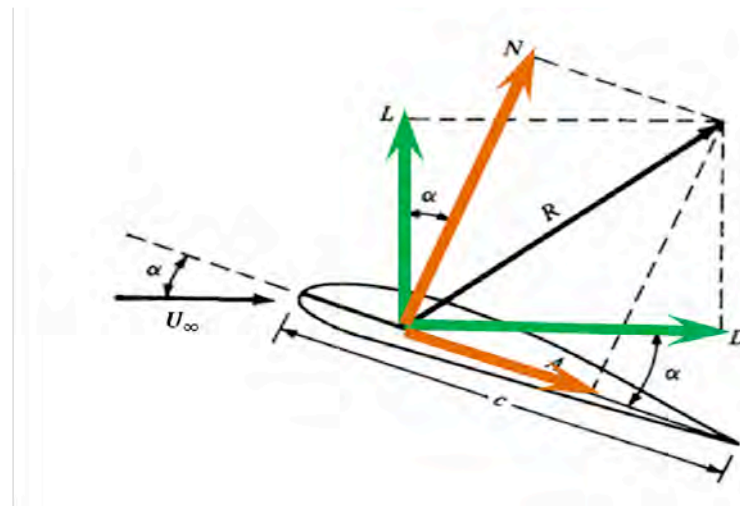


**Figure 4.3: Resultant Aerodynamic Force and its Components [20,27].**

The chord  $c$  is the linear distance from the leading edge to the trailing edge of the body. Sometimes,  $R$  is split into components perpendicular and parallel to the chord, as also shown in Figure 4.3. By definition,

$N$  = normal force = component of  $R$  perpendicular to  $c$

$A$  = axial force = component of  $R$  parallel to  $c$

The angle of attack  $\alpha$  is defined as the angle between  $c$  and  $U$ . Hence,  $\alpha$  is also the angle between  $L$  and  $N$  and between  $D$  and  $A$ . The geometrical relation between these two sets of components is found from Figure 4.3 as:

$$L = N \cos \alpha - A \sin \alpha \quad (4.7)$$

$$D = N \sin \alpha + A \cos \alpha \quad (4.8)$$

The integration of the pressure and shear stress distributions can be done to obtain the aerodynamic forces and moments [29, 38]. Let us consider the two dimensional body sketched in Figure 4.4. The chord line is drawn horizontally, and hence the relative wind is inclined relative to the horizontal by the angle of attack  $\alpha$ . An  $xy$  coordinate system is oriented parallel and perpendicular, respectively, to the chord. The distance from the leading edge measured along the body surface to an arbitrary point  $A$  on the upper surface is  $s_u$ ; similarly, the distance to an arbitrary point  $B$  on

the lower surface is  $s_l$ . The pressure and shear stress on the upper surface are denoted by  $p_u$  and  $\tau_u$ , respectively; both  $p_u$  and  $\tau_u$  are functions of  $s_u$ . Similarly,  $p_l$  and  $\tau_l$  are the corresponding quantities on the lower surface and are functions of  $s_l$ .

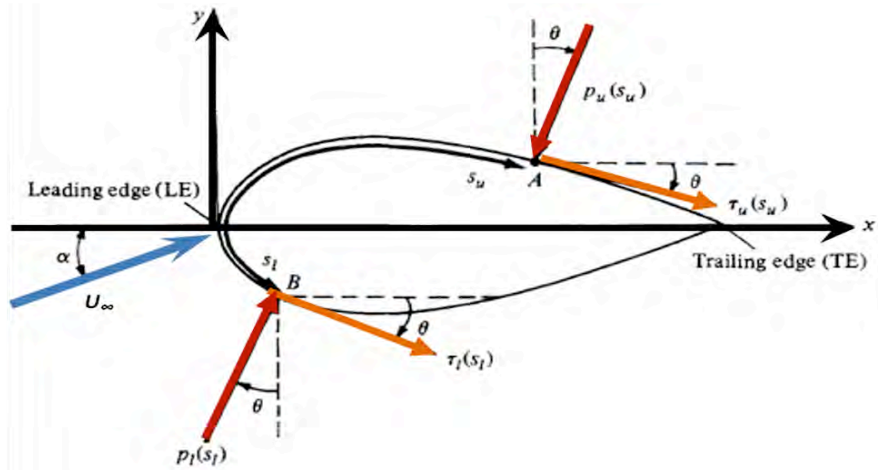


**Figure 4.4: Nomenclature for Integration of  $p$  and  $\tau$  Distribution [29,38].**

At a given point, the pressure is normal to the surface and is oriented at an angle  $\theta$  relative to the perpendicular; shear stress is tangential to the surface and is oriented at the same angle  $\theta$  relative to the horizontal. In Figure 4.4, the sign convention for  $\theta$  is positive when measured *clockwise* from the vertical line to the direction of  $p$  and from the horizontal line to the direction of  $\tau$ . In Figure 4.4, all thetas are shown in their positive direction.

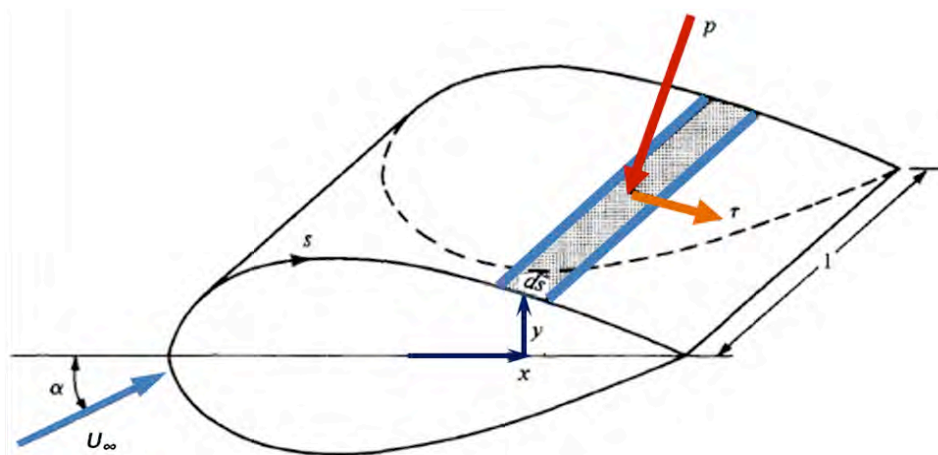


**Figure 4.5: Aerodynamic Force on an Element of the Body Surface [29,38].**

Now let us consider the two-dimensional shape in Figure 4.4 as a cross section of an infinitely long cylinder of uniform section. A unit span of such a cylinder is shown in Figure 4.5. Let us consider an elemental surface area  $dS$  of this cylinder, where  $dS = (ds)(l)$  as shown by the shaded area. We are interested in the contribution to the total normal force  $N'$  and the total axial force  $A'$  due to the pressure and shear stress on the elemental area  $dS$ . The primes on  $N'$  and  $A'$  denote force per unit span. Examining both Figures 4.4 and 4.5, it is seen that the elemental normal and axial forces acting on the elemental surface  $dS$  on the *upper* body surface are

$$dN'_u = -p_u ds_u \cos\theta - \tau_u ds_u \sin\theta \quad (4.9)$$

$$dA'_u = -p_u ds_u \sin\theta + \tau_u ds_u \cos\theta \quad (4.10)$$

On the *lower* body surface, we have

$$dN'_l = p_l ds_l \cos\theta - \tau_l ds_l \sin\theta \quad (4.11)$$

$$dA'_l = p_l ds_l \sin\theta + \tau_l ds_l \cos\theta \quad (4.12)$$

In these equations, the positive clockwise convention for  $\theta$  must be followed. For example, consider again Figure 4.4. Near the leading edge of the body, where the slope of the upper body surface is positive,  $\tau$  is inclined upward, and hence it gives a positive contribution to  $N'$ . For an upward inclined  $\tau$ ,  $\theta$  would be counterclockwise, hence negative. Therefore, in Equation (4.9),  $\sin\theta$  would be negative, making the shear stress term (the last term) a positive value, as it should be in this instance.

The total normal and axial forces *per unit span* are obtained by integrating Equations (4.9) to (4.12) from the leading edge (LE) to the trailing edge (TE):

$$N' = - \int_{LE}^{TE} (p_u \cos\theta + \tau_u \sin\theta) ds_u + \int_{LE}^{TE} (p_l \cos\theta - \tau_l \sin\theta) ds_l \quad (4.13)$$

$$A' = \int_{LE}^{TE} (-p_u \sin\theta + \tau_u \cos\theta) ds_u + \int_{LE}^{TE} (p_l \sin\theta - \tau_l \cos\theta) ds_l \quad (4.14)$$

In turn, the total lift and drag per unit span can be obtained by inserting Equations (4.13) and (4.14) into (4.7) and (4.8).

There are quantities of an even more fundamental nature than the aerodynamic forces themselves. These are *dimensionless force coefficients*. We have already defined a dimensional quantity called the free stream *dynamic pressure* as  $q_\infty = \frac{1}{2}\rho U_\infty^2$ . In addition, let  $s$  be a reference area and  $l$  be a reference length. The dimensionless force coefficients are defined as follows:

$$\text{Lift coefficient:} \quad C_L = \frac{L}{q_\alpha S} \quad (4.15)$$

$$\text{Drag coefficient:} \quad C_D = \frac{D}{q_\alpha S} \quad (4.16)$$

$$\text{Normal force coefficient:} \quad C_N = \frac{N}{q_\alpha S} \quad (4.17)$$

$$\text{Axial force coefficient:} \quad C_A = \frac{A}{q_\alpha S} \quad (4.18)$$

In the above coefficients, the reference area  $S$  and reference length  $l$  are chosen to pertain to the given geometric body shape; for different shapes,  $S$  and  $l$  may be different things. For example, for an airplane wing,  $S$  is the planform area, and  $l$  is the mean chord length, as illustrated in Figure 4.6.

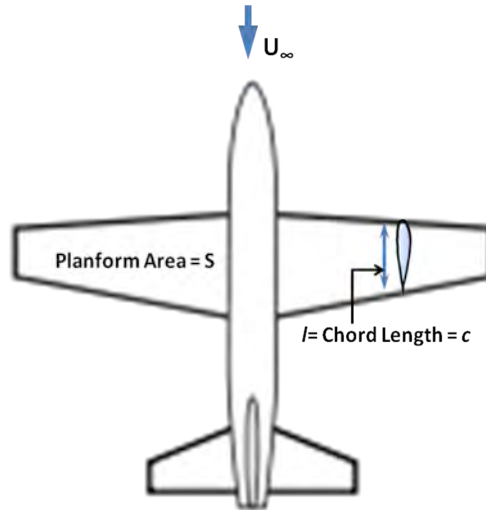


**Figure 4.6: Reference Area and Length for Airplane [29].**

The symbols in capital letters listed above, i.e.,  $C_L$ ,  $C_D$ ,  $C_N$ , and  $C_A$ , denote the force coefficients for a complete three-dimensional body such as an airplane or a finite wing. In contrast, for a two-dimensional body, the forces are per unit span. For these two dimensional bodies, it is conventional to denote the aerodynamic coefficients by lowercase letters as follows:

$$c_l = \frac{L}{q c} \quad \text{and} \quad c_d = \frac{D}{q c}$$

Where, the reference area  $S = c(l) = c$ .

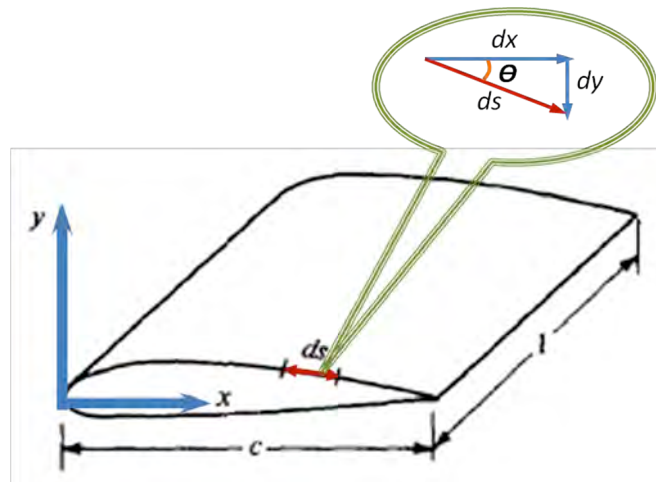


**Figure 4.7: Geometrical Relationship of Differential Lengths [29,38].**

The most useful forms of Equations (4.13) and (4.14) are in terms of the dimensionless coefficients introduced above. From the geometry shown in Figure 4.7,

$$dx = ds \cos \theta$$

$$dy = -ds \sin \theta$$

$$S = c(l) = c$$

Substituting the above expressions of  $dx$ ,  $dy$  and  $S$  into Equations (4.13) and (4.14), dividing by  $q_\infty$ , we obtain the following integral forms for the force and moment coefficients:

$$C_n = \frac{1}{c} \int_0^c (c_{p,l} - c_{p,u}) dx + \frac{1}{c} \int_0^c \left( c_{f,u} \frac{dy_u}{dx} + c_{f,l} \frac{dy_l}{dx} \right) dx \quad (4.19)$$

$$C_a = \frac{1}{c} \int_0^c \left( c_{p,u} \frac{dy_u}{dx} - c_{p,l} \frac{dy_l}{dx} \right) dx + \frac{1}{c} \int_0^c (c_{f,u} + c_{f,l}) dx \quad (4.20)$$

Here,  $y_u$  is directed above the  $x$  axis, and hence is positive, whereas  $y_l$  is directed below the  $x$  axis, and hence is negative. Also,  $dy/dx$  on both the upper and lower surfaces follow the usual rule from calculus, i.e., positive for those portions of the body with a positive slope and negative for those portions with a negative slope. When shear stress due to viscous effect is neglected, an integration of a pressure distribution over an airfoil chord for both upper and lower surfaces is known to provide normal and axial force acting on an airfoil section [29, 38] as follows:

$$C_n = \frac{1}{c} \int_0^c (c_{p,l} - c_{p,u}) dx \quad (4.21)$$

$$C_a = \frac{1}{c} \int_0^c \left( c_{p,u} \frac{dy_u}{dx} - c_{p,l} \frac{dy_l}{dx} \right) dx \quad (4.22)$$

The known pressure coefficients from the experiment can be calculated for the normal and axial force by using a numerical integration of the above equations in the Trapezoidal approximating forms.



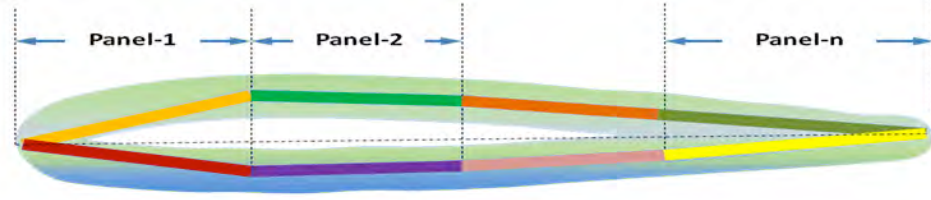


**Figure 4.8: Paneling of the Wing Surface [29,38].**

As shown in Figure 4.8, both the surfaces of the wing section can be divided into small panels corresponding to a total of gaps between each pressure tap location [34]. When  $n$  is a number of panels, the equations can be converted to:

$$C_n = \sum_{i=1}^n \left[ (c_{p,l,i} - c_{p,u,i}) \Delta \left( \frac{x_i}{c} \right) \right] \quad (4.23)$$

$$C_a = \sum_{i=0}^n \left[ \left( c_{p,u,i} \frac{\Delta y_{u,i}}{\Delta x_i} - c_{p,l,i} \frac{\Delta y_{l,i}}{\Delta x_i} \right) \Delta \left( \frac{x_i}{c} \right) \right] \quad (4.24)$$

The interpolated and extrapolated pressure coefficients would be applied to Equation (3.23) and (3.24) in order to get the normal and axial force at a section of interest. Lift and drag coefficient can be obtained from:

$$c_l = c_n \cos \alpha - c_a \sin \alpha \quad (4.22)$$

$$c_d = c_n \sin \alpha + c_a \cos \alpha \quad (4.23)$$

The over-all value of the coefficients for the whole wing can be found out by averaging the same values of each segments of the wing along the span.

## EXPERIMENTAL SETUP AND METHODOLOGY

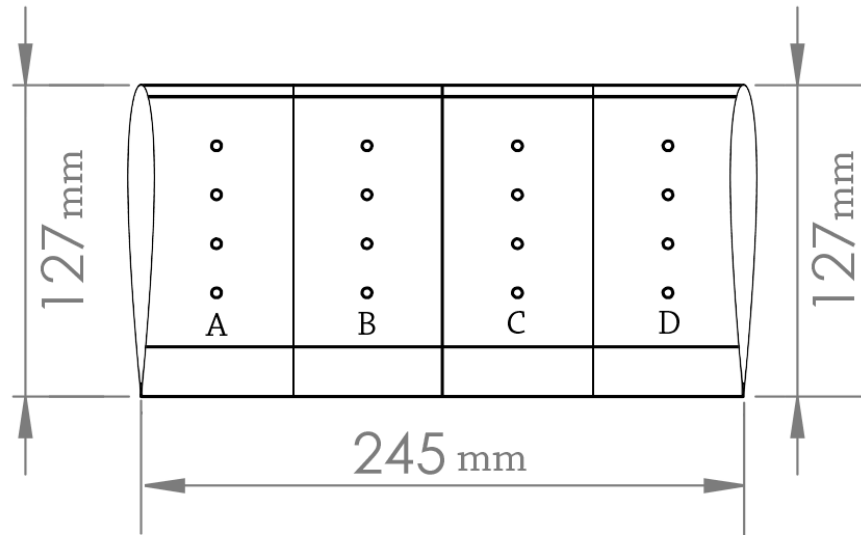
### 5.1 Design and Construction

Manufacturing of the wings is the essential part of this experiment. The wings which will be investigated should be manufactured with great precision. The wings have to have smooth surfaces, equally balanced weight and good shape geometry. The trailing and leading edges should meet the calculated geometries as the angle of attack depends on their reference line. So, to keep in mind the precision criteria, the design is made locally available solid works software and printed by 3D printer. The aerodynamic characteristics ( $C_L$ ,  $C_D$  and  $L/D$ ) can be calculated from the surface pressure distribution of the wing as discussed in the previous chapter. To obtain the pressure distribution over the surfaces, wooden-plastic wing models are prepared with a specific aerofoil, suitable fixture is prepared to set the models in the wind tunnel and a multi-tube manometer is fabricated to take the pressure readings from the surfaces of the wing models.

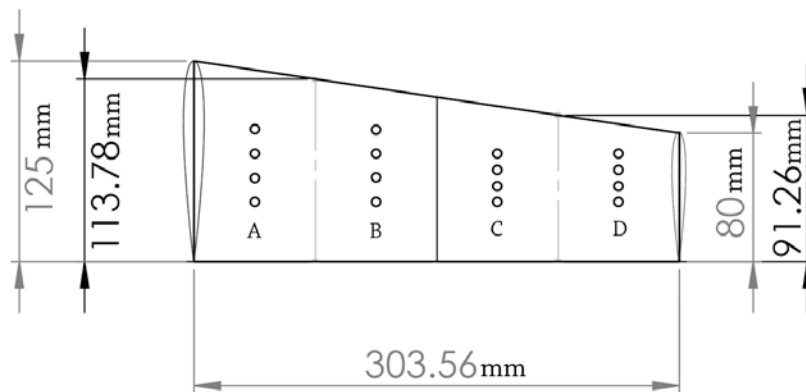
#### 5.1.1 Wing Models

Using NACA 4412 aerofoil, wooden -plastic models for five wings are prepared having the equal surface area ( $31115 \text{ mm}^2$ ) as shown in Figure 5.1. Each model is provided with 32 pressure tapings along the span and chord (16 at upper surface and 16 at lower surface). Along the span the wings are divided into four equal segments (A, B, C and D) as per the figure. For Rectangular wing (Model-1), the chord and the span length are 127 mm and 245 mm respectively. For the curved edge wings, the average chord length is different for different segments along the span. So, as per the model chord length, the span length and the ratio of root chord to tip chord of the curved edge planforms are given in the Table-5.1. Four pressure tapping points at

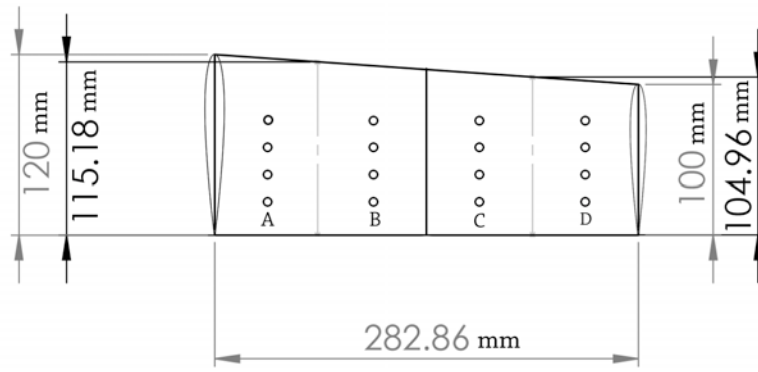
upper surface and four pressure tapping points at lower surface are made at 20%, 40%, 60% and 80% of the average chord length of each segment of all the wing models.



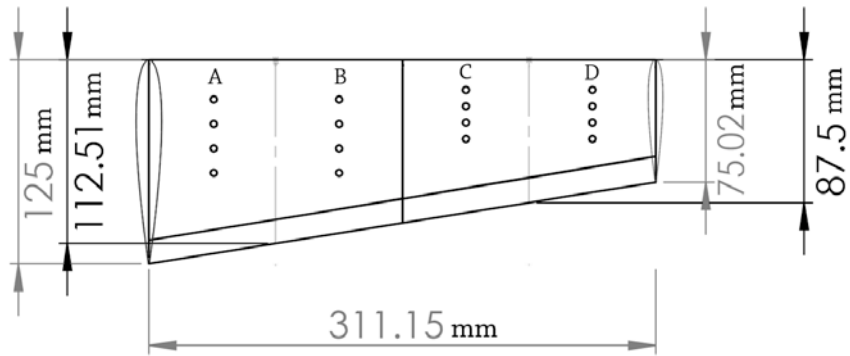
(a) Model-1 : Rectangular Planform (Reference).



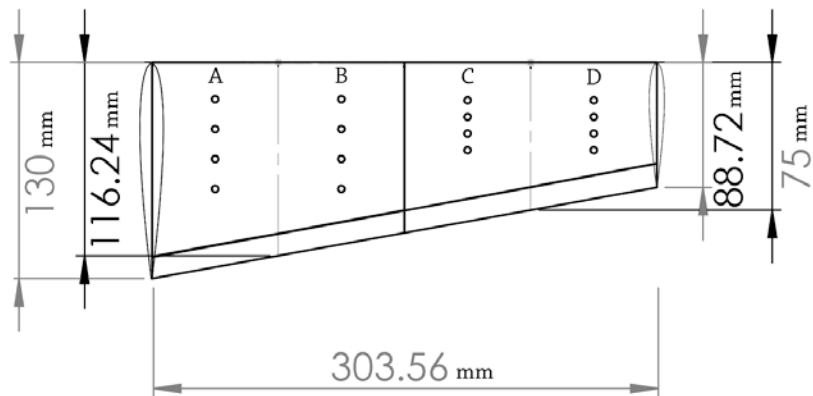
(b) Model-2 : Curved Leading Edge Planform, Type-1.



(c) Model-3 : Curved Leading Edge Planform, Type-2.



(d) Model-4 : Curved Trailing Edge Planform, Type-1.



(e) Model-5 : Curved Trailing Edge Planform, Type-2.

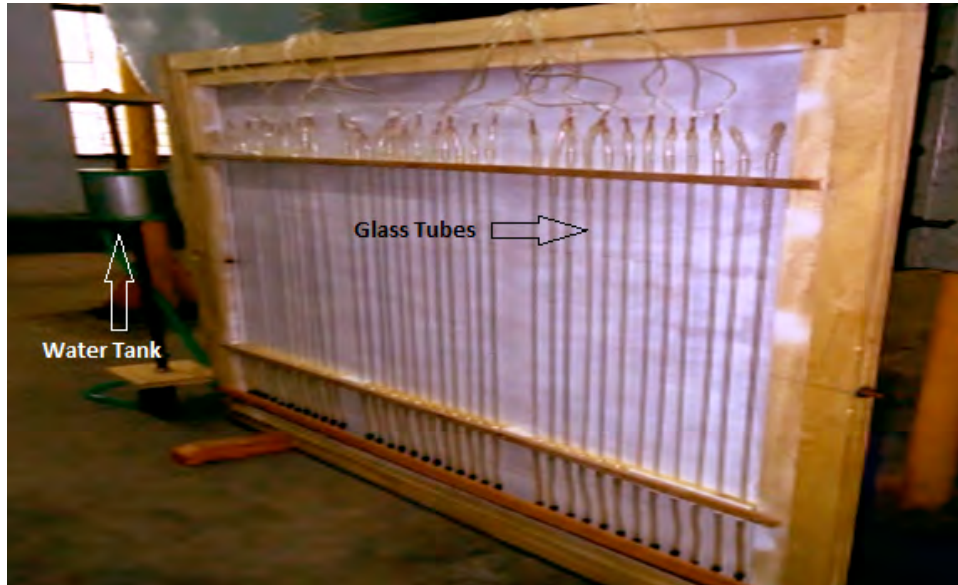
**Figure 5.1: Experimental Wing Models**

Table-1: Dimensions of Five Models

Model No	Type of Model	Average Chord Length, mm	Span Length, mm	Chord Length at Segments, mm				Aspect Ratio
				A	B	C	D	
1	Rectangular Planform	127	245	127	127	127	127	1.929
2	Curved Leading Edge Planform, Type-1	102.51	303.56	125	113.78	91.26	80	2.96
3	Curved Leading Edge Planform, Type-2	110.04	282.86	120	115.18	100	104.96	2.57
4	Curved Trailing Edge Planform, Type-1	100.01	311.15	125	112.51	87.5	75.02	3.11
5	Curved Trailing Edge Planform, Type-2	102.49	303.56	130	116.24	88.72	75	2.96

### 5.1.2 Pressure Measuring Device

The arrangement of multi-tube manometer for measuring the pressures is shown in Figure 5.2. The multi-tube manometer mainly consists of a water tank and 36 manometer glass tubes (in this experiment, 32 glass tubes are used) connected to the tapping points in wing model surfaces. The water tank is used to store the distilled water. Each limb is fitted with a scale graduated in mm to measure the difference of water height. The static pressure is calculated from the difference in water height.



**Figure 5. 2: Multi-tube Manometer**

### **5.1.3 Fixture for Altering Angle of Attack**

The details of wind tunnel are shown in Figure 5.3. A fixture is fabricated and fixed in the test section of the wind tunnel as shown in Figure 5.4. The fixture facilitates the wing models to rotate and fix at any angle of attack. The wing models are tested at angle of attack from  $-4^{\circ}$  to  $24^{\circ}$  with a step of  $4^{\circ}$ . Each model is rotated and fixed at the desired angle by seeing the preset scales (in degrees) pasted on the frame.

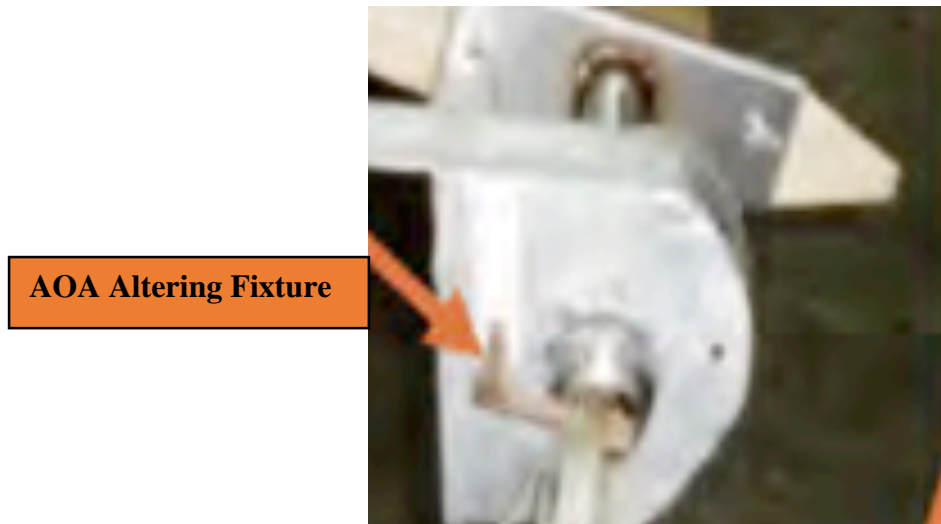


**Figure 5.3: AOA Altering Fixture**

## 5.2 Experimental Setup

### 5.2.1 Wind Tunnel

The experiment is carried out in a 700 mm×700 mm closed circuit wind tunnel as shown in Figure 5.3 available at turbulence lab of Department of Mechanical Engineering, BUET. The wind speed is created by the two 700 mm counter rotating fans. At the discharge of the fans there is a silencer to reduce the sound level. From the silencer air flow passes through the flow controlling butterfly valve, diffuser and the plenum chamber to stabilize the flow to certain level. The fan motors are

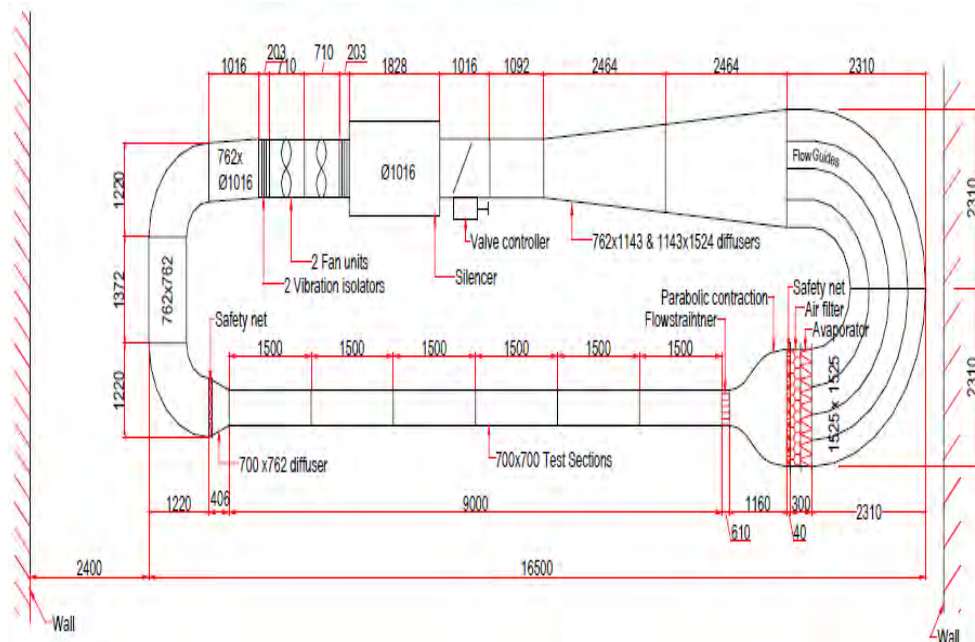


**Figure 5.3: Schematic Diagram of the Wind Tunnel at BUET's Turbulence Lab [39]**

powered by 400V-3 $\Phi$ -50Hz power supply through motor speed controller. Thus the wind speed in the tunnel can be varied both by controlling the fan motor speed as well as by controlling the butterfly valve [39]. To facilitate the present experiment in the open air condition the diffuser at the end of the test section is taken out and the discharge side of the test section is fitted with a 700 mm×700 mm discharge duct

and a 1000 mm×1000 mm to 762 mm×762 mm bell mouth entry is added at the return duct to have smooth entry. Thus the 406 mm open flow field created between the discharge duct and bell mouth entry become the experimental space as shown in Figure 5.4 where desired velocity is obtained.

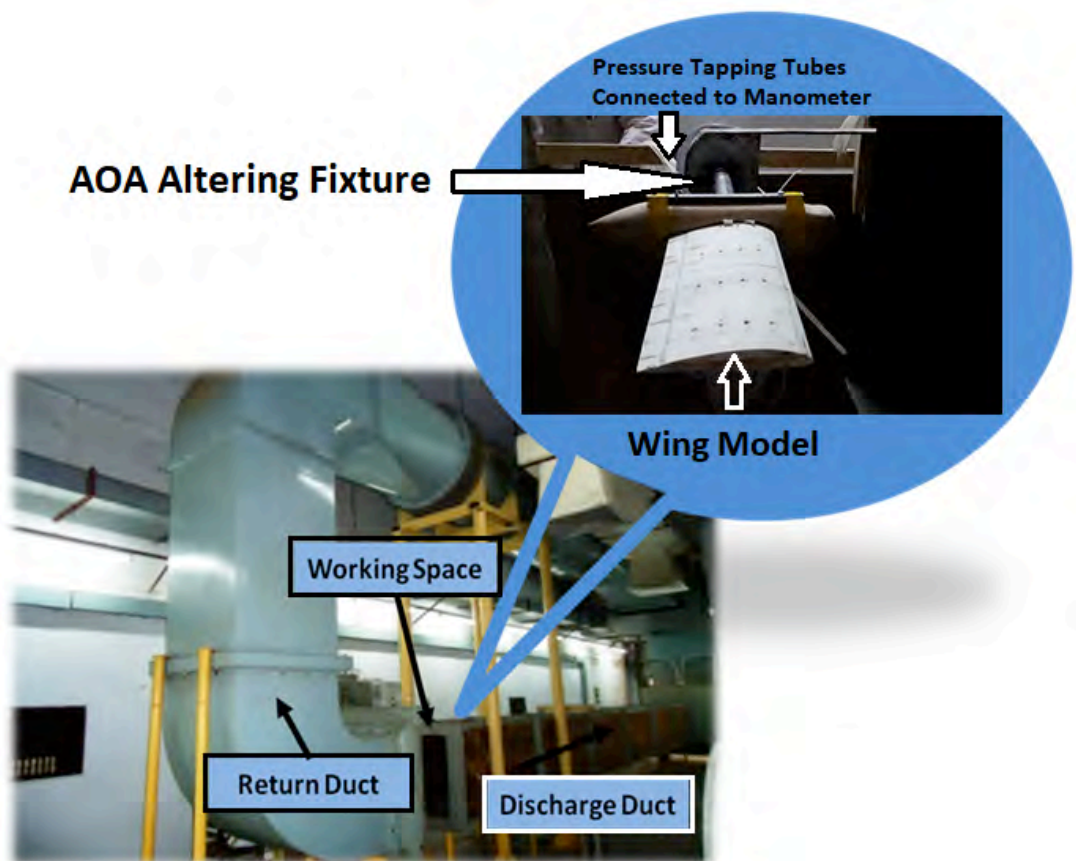


**Figure 5. 4: Photograph of Experimental Set-up.**

### **5.2.2 Experimental Parameters**

All the experimental data are taken at room temperature of 29°C and at air speed of 22 m/s (79.20 kph) and the air flow is considered incompressible throughout the experiment. The Reynold number and Mach number are  $1.74 \times 10^5$  and 0.06 respectively. The specific density of both air and water corresponding to room temperature is assumed to be  $1.15 \text{ kg/m}^3$  and  $996 \text{ kg/m}^3$  respectively.



### 5.3 Methodology

- a. Initially, the static pressure at different angles of attack ( $\alpha = -4^\circ, 0^\circ, 4^\circ, 8^\circ, 12^\circ, 16^\circ, 20^\circ$  and  $24^\circ$ ) are measured from both upper and lower surfaces of the wing models through different pressure tapings by using a multi-tube manometer during wind tunnel testing.
- b. From the static pressure data, the respective coefficient of pressure ( $C_p$ ) is calculated using equation (4.1) to (4.6).
- c. The values of  $C_p$  of both surfaces of individual planforms are plotted in  $C_p$  versus %C graph to observe the pressure pattern of different segments of each planform along the chord length.
- d.  $C_L$  and  $C_D$  of all the wing planforms at every angle of attack are determined from equation (4.23) to (4.26).
- e. L/D at different angle of attack for all the wing models are obtained from the ratio of  $C_L$  to  $C_D$  at respective angle of attack.
- f. Finally, the lift characteristics, drag characteristics and lift to drag ratio of the wing planforms are analyzed and compared with each other from  $C_L$  versus  $\alpha$ ,  $C_D$  versus  $\alpha$  and L/D versus  $\alpha$  graphs.

## RESULTS AND DISCUSSIONS

### 6.1 Analysis of Collected Data

The pressure coefficients of both upper and lower surfaces of different planforms were measured through the wind tunnel testing to analyze aerodynamic characteristics. Then the pressure coefficients are plotted along chord wise positions (% C) at different angles of attack for each of the four segments. The pressure coefficients of a rectangular wing planform are also measured through the wind tunnel testing. These data are plotted in the same way in all the graphs as a reference. Then surface pressure distribution of all the wing planforms are discussed making comparison with each other at every segment for every angle of attack. The resulting data, computed in terms of the normal and axial forces on the wing models, are used as follows:

- a. To determine coefficient of lift ( $C_L$ ), coefficient of drag ( $C_D$ ) and lift to drag ratio (L/D) of individual wing.
- b. Lift characteristics, drag characteristics and lift to drag ratio for all five wing planforms are discussed making comparison with each other from  $C_L$  versus Angle of Attack (AOA,  $\alpha$ ),  $C_D$  versus  $\alpha$  and L/D versus  $\alpha$  plots, respectively.
- c. Calculated values of pressure coefficients of all five planforms from  $-4^\circ$  to  $24^\circ$  angles of attack are shown in Appendix-I.
- d. Uncertainties of experimental results are also analyzed in light of the procedure suggested by Cimbala [40]. The details of uncertainty analysis are shown in Appendix-II.

## 6.2 Surface Pressure Distributions

The pressure distributions of both upper and lower surfaces along the chord length of four segments (Segment- A, B, C and D) of five experimental wing planforms for  $-4^{\circ}$ ,  $0^{\circ}$ ,  $4^{\circ}$ ,  $8^{\circ}$ ,  $12^{\circ}$ ,  $16^{\circ}$ ,  $20^{\circ}$  and  $24^{\circ}$  angle of attack (AOA) are plotted in this chapter. In the graphs, the horizontal axis represents the percentage of the chord length (%C) and the vertical axis represents the surface pressure coefficient ( $C_p$ ). The vertical axis above the zero line (horizontal axis) denotes the negative pressure coefficients or suction pressure coefficients and the vertical axis below the zero line denotes the positive pressure coefficients. All the mentioned graphs are discussed in details in the subsequent sub-paragraphs.

### 6.2.1 Pressure Distributions at $-4^{\circ}$ AOA

At  $-4^{\circ}$  AOA, surface pressure distribution for four segments (A, B, C and D) of Model-1 (Rectangular, M- 1), Model- 2 (Curved Leading Edge, M- 2), Model- 3 (Curved Leading Edge, M- 3), Model- 4 (Curved Trailing Edge, M- 4) and Model- 5 (Curved Trailing Edge, M- 5) planforms are shown in Figure 6.1, 6.2, 6.3, and 6.4, respectively. In all the four figures (Figure-6.1, 6.2, 6.3 and 6.4), both upper and lower surface pressure coefficient,  $C_{pu}$  and  $C_{pl}$  are plotted along the chord (C) for 20% C, 40% C, 60% C and 80% C.

In Figure 6.1, it is seen that both upper and lower surface pressure of all the five planforms near the root (segment-A) are almost at the suction side. The lower surfaces are having more suction pressure than the upper surfaces near the leading edge up to 30~35 % C. But from 40% C up to the trailing edge, the suction pressure of upper surfaces is greater than the suction pressure of lower surfaces. It is also seen that the lower surface pressure decreases from 10% C to 40% C rapidly and then decreases slowly up to 80% C for all the five planforms. For Model- 2 and 3 and Model- 4 and 5 planforms, the upper surface pressure increases up to 40% C and then slowly decreases up to 80% C but for rectangular planform the upper surface pressure remains almost constant throughout the chord length.

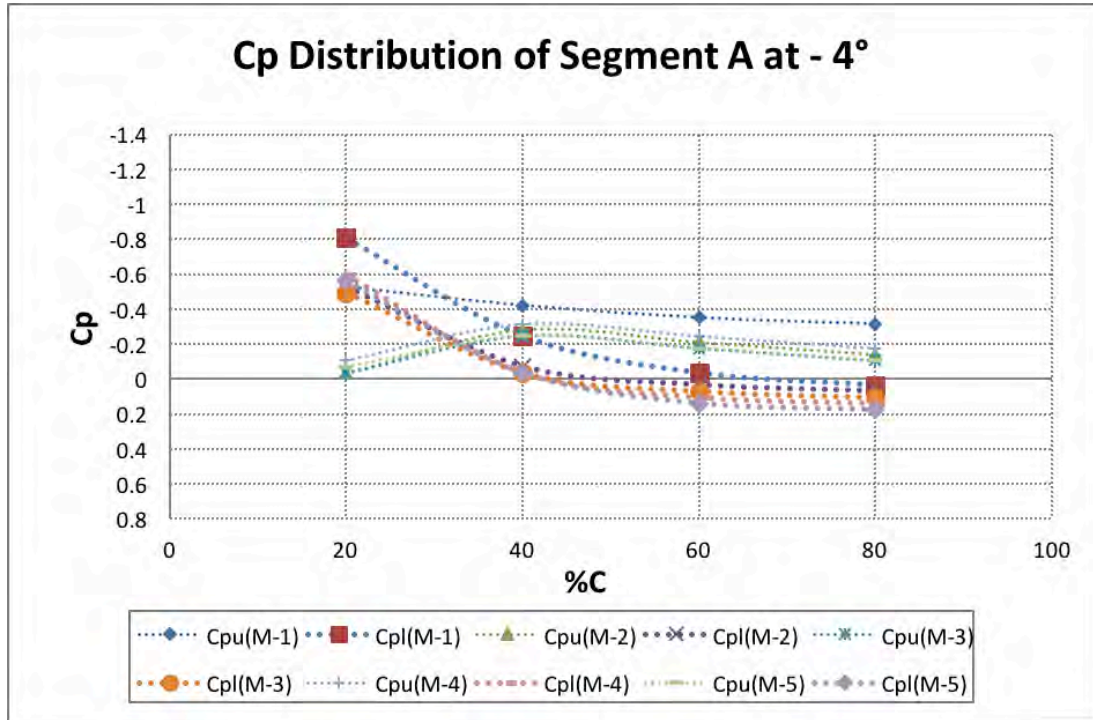


**Figure 6.1:  $C_p$  Distribution of Segment-A at  $\alpha = -4^\circ$**

The upper and lower surface pressure distributions for Segment-B of the five planforms are shown in Figure 6.2. The graph shows that both upper and lower surface pressure of all the five planforms at segment B are also almost at the suction side. For Model- 1 and Model- 2 and 3 planforms, the lower surfaces are having more suction pressure than the upper surfaces near the leading edge up to 30 % C. But from 30 % C up to the trailing edge, the suction pressures of upper surfaces are greater than the suction pressure of lower surfaces. For Model- 4 and 5 planforms, the suction pressure of the upper surface is greater than the suction pressure of the lower surface throughout the chord length (from leading edge to trailing edge). Up to 60%C, the lower surface pressure curve is at the highest for Model- 1 planform, lowest for Model- 4 and 5 planforms and in between for Model- 2 and 3 planforms. Beyond 60 % C up to the trailing edge, the said curves are almost overlapping each other following the similar pattern. Up to 35 %C, the upper surface pressure curve of Model-1 remains at the highest, Model-2 and 3 planforms at the lowest and Model- 4 and 5 planforms is in between the Model- 1 and Model- 2 and 3 planforms. But from 35~80 %C, the upper surface pressure of Model- 2 and 3 planforms are at the

highest level, Model- 1 planform at the lowest and for Model- 4 and 5 planforms; it is in between other planforms. Again, from 80 %C towards the trailing edge, the upper surface pressure curve of Model- 1 planform tends to reach to the higher level than the other planforms.

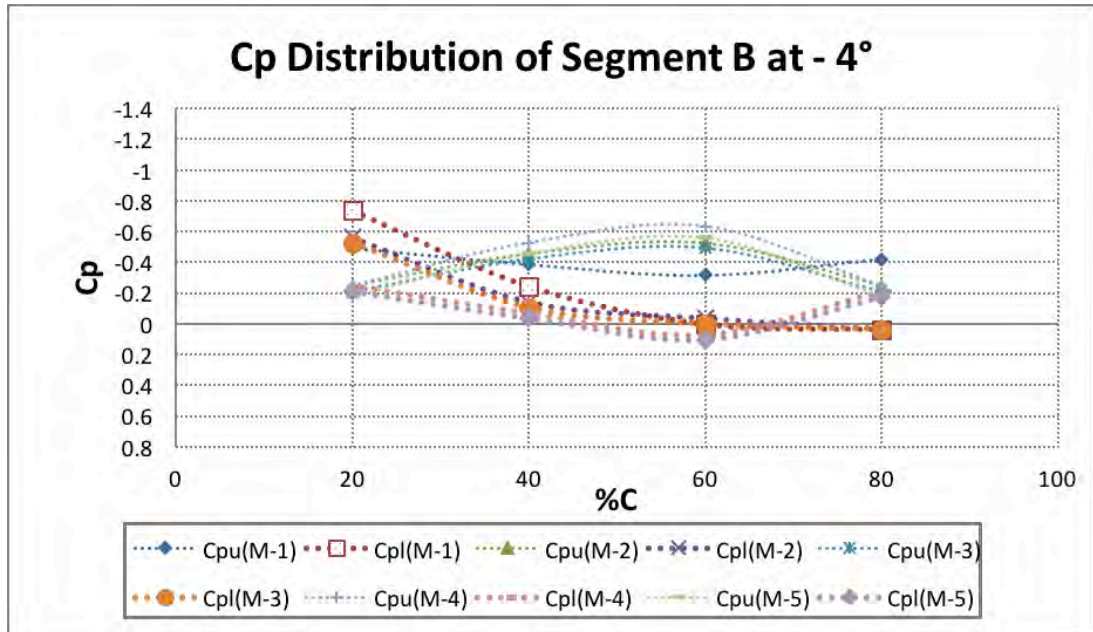


**Figure 6.2:  $C_p$  Distribution of Segment-B at  $\alpha = -4^\circ$**

Figure 6.3 shows the upper and lower surface pressure distribution for Segment-C of the five planforms. For Model- 1 planform, the lower surface is having more suction pressure than the upper surface up to 35% C. The lower surface pressure decreases rapidly from 20% C to 40% C and then further decreases slowly up to the trailing edge. But the upper surface pressure remains constant from the leading edge up to 50% C and then slowly decreases up to the trailing edge. For Model- 2 and 3 planforms, the upper surface is having more suction pressure than the lower surface throughout the chord length and both surfaces' pressure gradually decreases from the leading edge towards the trailing edge. The difference between the upper surface and lower surface pressure of Model- 2 and 3 planforms is highest at below 20% C and this difference gradually decreases up to 60% C and again increases slightly from 60% C to 80% C.

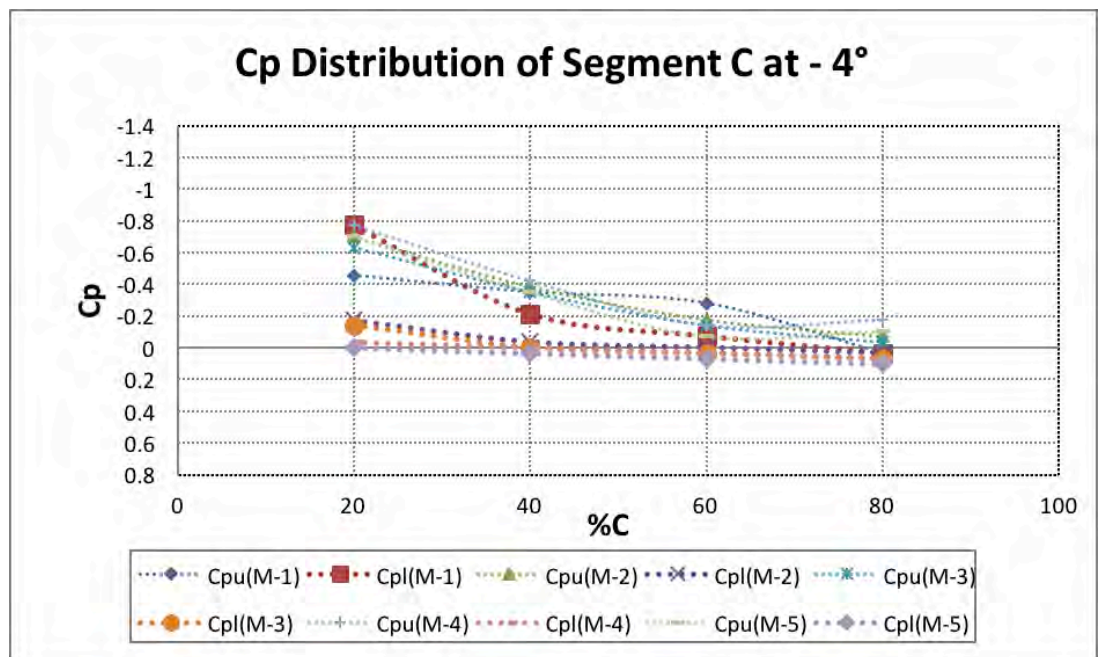


**Figure 6.3:  $C_p$  Distribution of Segment-C at  $\alpha = -4^\circ$**

For Model- 4 and 5 planforms, the upper surface suction pressure is greater from 20% C up to the trailing edge. The difference between the upper and lower surface pressure of the Model- 4 and 5 planforms is observed highest at 20% C.

In Figure 6.4, the surface pressure distributions for Segment-D of the five planforms are shown. For Model-1 planform, the lower surface is having more suction pressure than the upper surface at below 20% C. The lower surface pressure decreases rapidly from 20% C to 40% C and then further decreases slowly up to the trailing edge. The upper surface pressure decreases slowly from 20% C up to 60% C and then increases up to the trailing edge. For Model- 2 and 3 planforms, the upper surface is having more suction pressure than the lower surface throughout the chord length and both surfaces pressures gradually decrease from the leading edge towards the trailing edge. The difference between the upper surface and lower surface pressure of Model- 2 and 3 planforms is having the highest value from 60% C to 90% C.

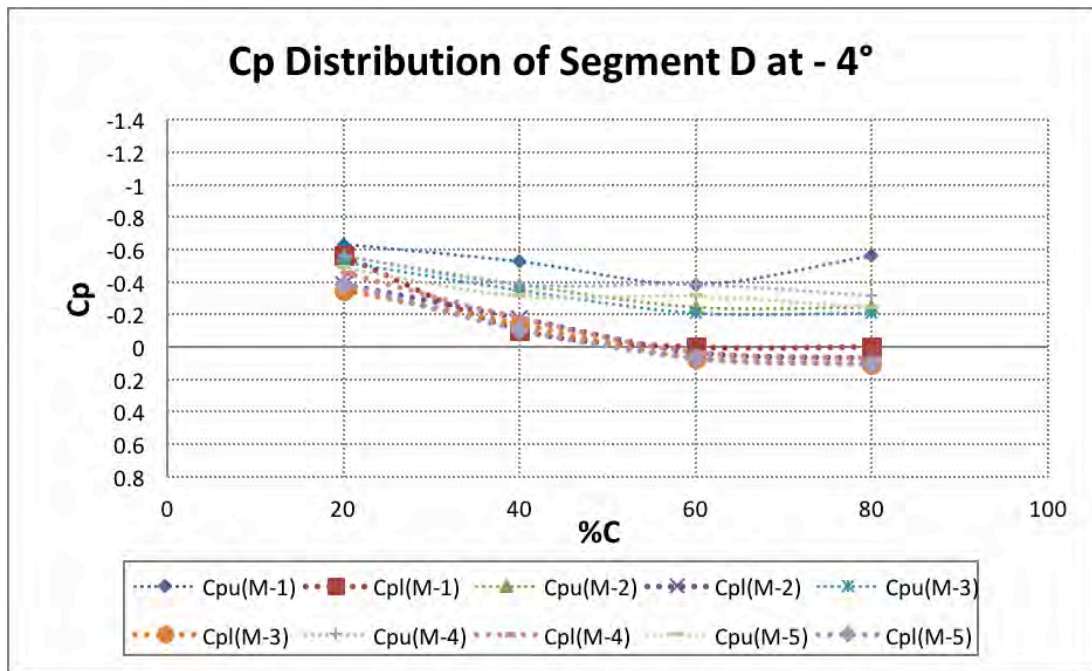


**Figure 6.4:  $C_p$  Distribution of Segment-D at  $\alpha = -4^\circ$**

For Model- 4 and 5 planforms, the upper surface suction pressure is also greater than the lower surface suction pressure throughout the chord length. The difference between the upper and lower surface pressure of Model- 4 and 5 planforms is observed at 20% C. This difference gradually increases up to 40% C and then decreases slowly up to the trailing edge. The overall pressure difference between the two surfaces is highest for Model- 4 and 5 planforms, lowest for rectangular planform and in between the highest and the lowest for Model- 2 and 3 planforms in segment-D.

### 6.2.2 Pressure Distributions at $0^\circ$ AOA

At  $0^\circ$  AOA for four segments, both upper and lower surface pressure coefficient,  $C_{pu}$  and  $C_{pl}$  of Model- 1, 2, 3, 4 and 5 planforms are plotted along the chord in Figure 6.5, 6.6, 6.7 and 6.8, respectively.

In Figure 6.5, the surface pressure distributions for segment-A of the five planforms at  $0^\circ$  AOA are shown. It is found that upper surface of Model- 1 planform is having higher suction pressure than the lower surface pressure. For M- 2, 3, 4 and 5

planforms, the upper surface suction pressure is lower than the pressure of the lower surface up to 25% C but beyond 25% C up to the trailing edge upper surface suction pressure is higher than the lower surface pressure. The lower surface pressure of all five planforms decreases from leading edge to trailing edge but the rate of reduction is higher up to 40% C. For Model- 1 planform, the upper surface pressure decreases gradually from leading edge to trailing edge. For Model- 2, 3, 4 and 5 planforms, upper surface pressure increases from the leading edge up to 40% C, then decreases towards the trailing edge. But the upper surface suction pressure of Model- 4 and 5 planforms are higher than model- 2 and 3 planforms and lower surface of Model- 4 and 5 planforms is having greater positive pressure than Model- 2 and 3 planforms. The difference between the upper surface and lower surface pressure of Model- 2, 3, 4 and 5 planforms become maximum at 40% C.

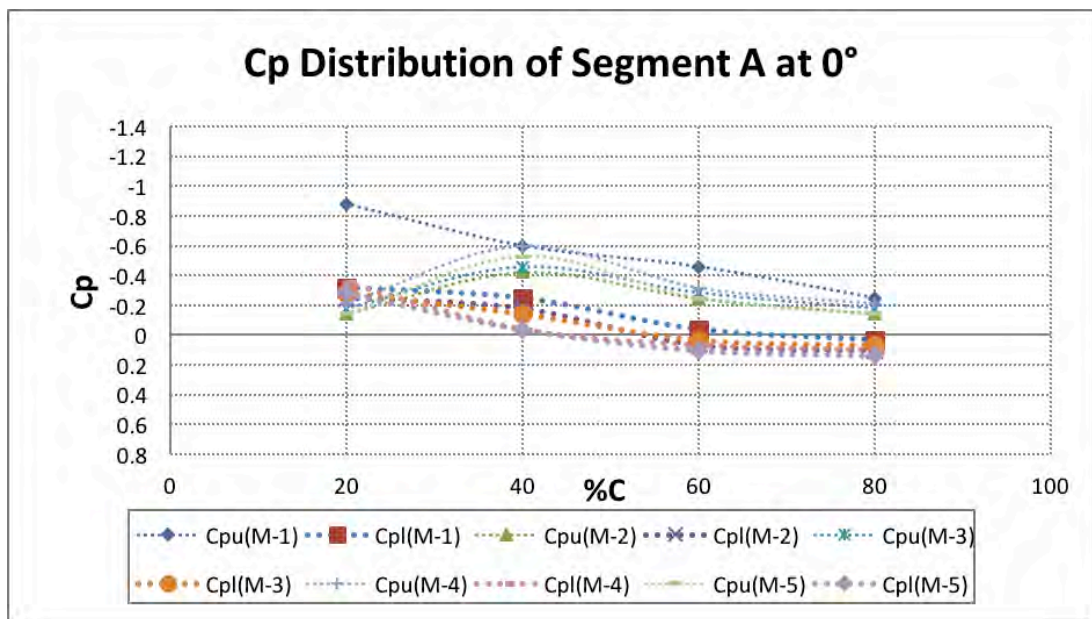


**Figure 6.5:  $C_p$  Distribution of Segment-A at  $\alpha = 0^\circ$**

In Figure 6.6, the surface pressure distributions for Segment-B of the five planforms at  $0^\circ$  AOA are shown. It is found that upper surface of all five planforms are having higher suction pressure than the lower surface pressure of the respective planforms except in case of Model- 1 planform at 60% C. The upper surface of Model- 1 planform is having the positive pressure instead of suction pressure at 60% C. For



Model-1 planform, the upper surface pressure decreases from 20% C and reaches to the positive value at 60% C, then again increases up to the trailing edge. The lower surface pressure remains almost constant throughout the chord. For Model- 2 and 3 planforms, upper surface pressure increases slowly from the leading edge up to 60% C, then decreases towards the trailing edge rapidly. The lower surface pressure decreases from leading edge to trailing edge. The difference between the upper surface and lower surface pressure of Model- 2 and 3 planforms becomes maximum at 60% C. In case of Model- 4 and 5, the upper surface pressure remains almost constant up to 60% C and then decreases towards the trailing edge. The lower surface pressure decreases from leading edge to trailing edge. The upper surface suction pressure of Model- 2 and 3 planforms is higher than Model- 4 and 5 planforms and lower surface of Model- 2, 3, 4 and 5 planforms are having almost same pressure throughout the chord.

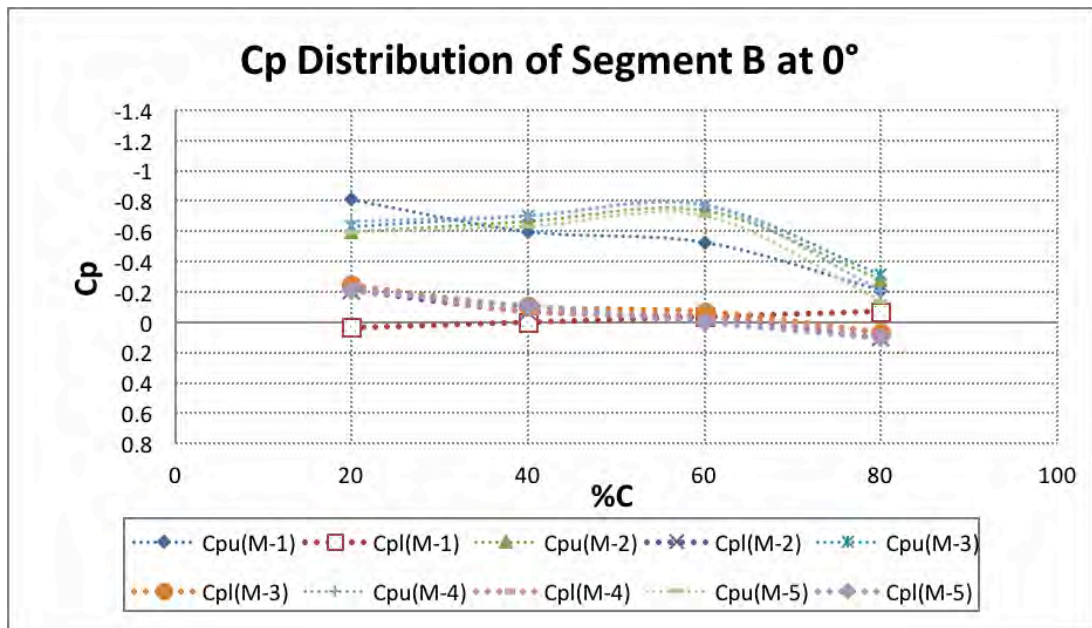


**Figure 6.6:  $C_p$  Distribution of Segment-B at  $\alpha = 0^\circ$**

Figure 6.7 shows the upper and lower surface pressure distribution for segment- C of five planforms. For Model- 1 planform, the upper surface is having more suction pressure than the lower surface throughout the cord. The lower surface pressure decreases from 20% C to 40% C and then decreases slowly up to the trailing edge.

For Model- 4 and 5 planforms, the upper surface suction pressure is more than that of the lower surface. The upper surface pressure gradually reduces from leading edge to trailing edge. The lower surface pressure gradually decreases up to 40% C and then almost constant up to trailing edge. For Model- 4 and 5 planforms, the lower surface suction pressure is lower than that of the upper surface up to 20% C and from 20% C to trailing edge and the upper surface pressure is higher than the pressure of the lower surface. The upper surface pressure slowly decreases from 20% C to 60% C and then gradually increases up to the trailing edge. From 20% C the lower surface suction pressure decreases and reaches to the positive value at 40- 80 % C.

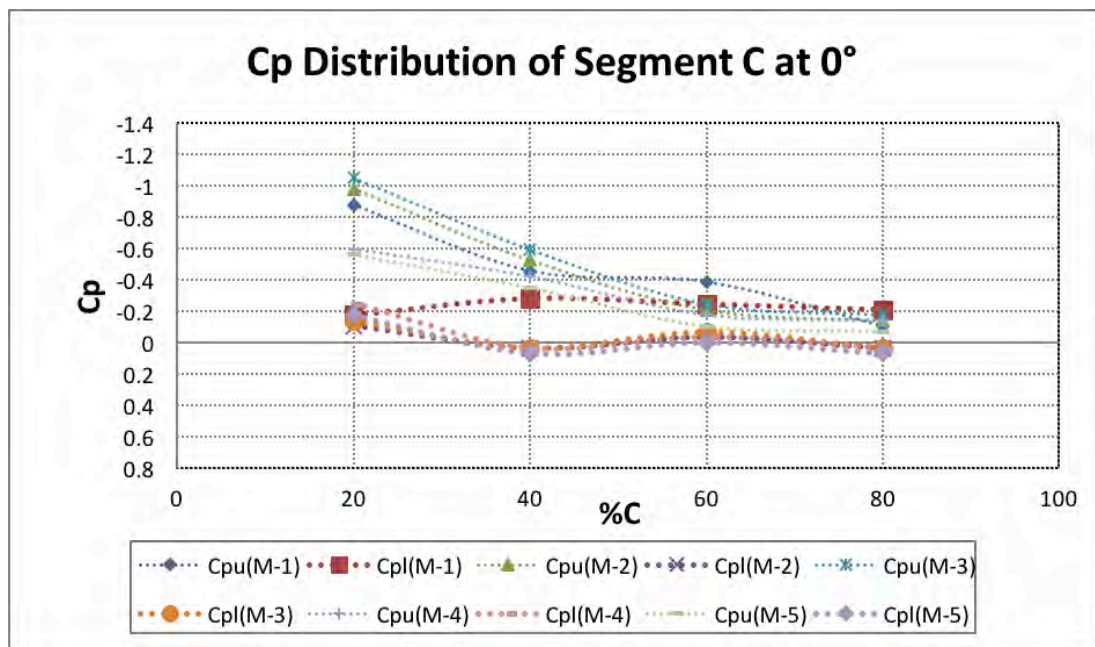


**Figure 6.7: Cp Distribution of Segment-C at  $\alpha = 0^\circ$**

In Figure 6.8, the surface pressure distributions for Segment-D of five planforms at  $0^\circ$  angle of attack are shown. From the figure it is observed that upper surface of all five planforms are having higher suction pressure than the lower surface pressure of the respective planforms. For Model- 1 planform, the upper surface pressure decreases from 20% C to 60% C and then again increases up to the trailing edge. The lower surface pressure also reduces from 20 to 60% C and then remains almost

constant up to the trailing edge. For Model- 2 and 3 planforms, the upper surface pressure decreases from the leading edge to the trailing edge and the lower surface pressure decreases up to 40% C, constant from 20 to 60% C and decreases again up to trailing edge. The difference between the upper surface and lower surface pressure of Model- 2 and 3 planforms is observed maximum at 20% C. In case of Model- 4 and 5 planforms, the upper surface pressure decreases up to 60% C and then remains almost constant up to the trailing edge. The lower surface pressure decreases slightly from leading edge to 40% C, the constant up to 60% C and finally reaches to the positive value at 90% C. Out of five planforms, the upper surface of the Model- 4 and 5 planforms is having the lowest suction pressure but it's lower surface is having the highest pressure.

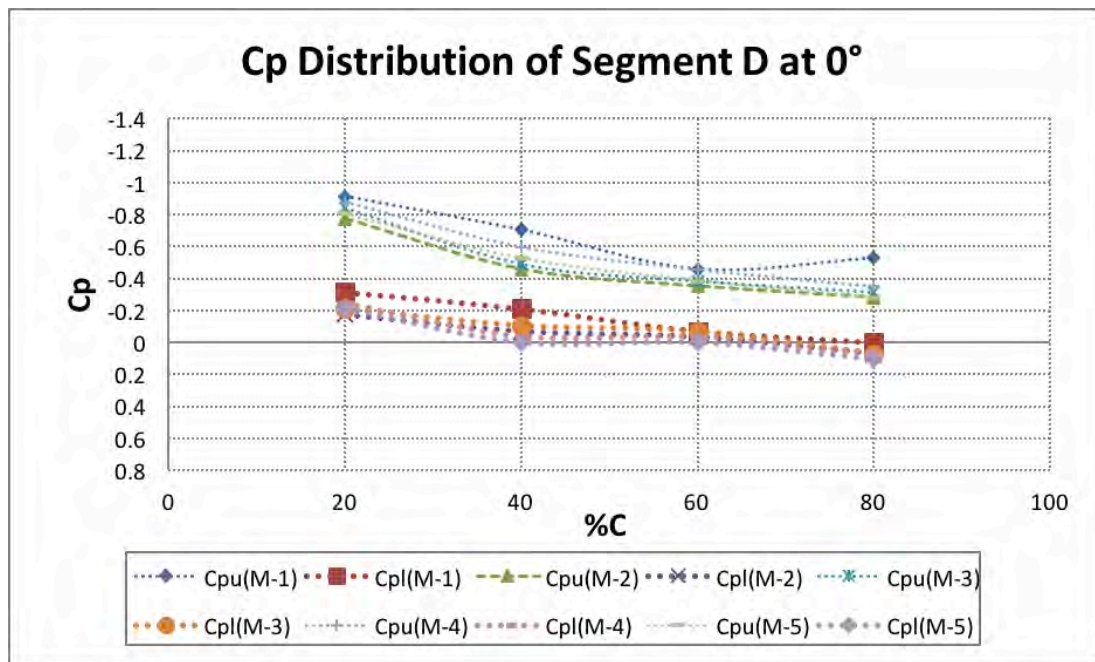
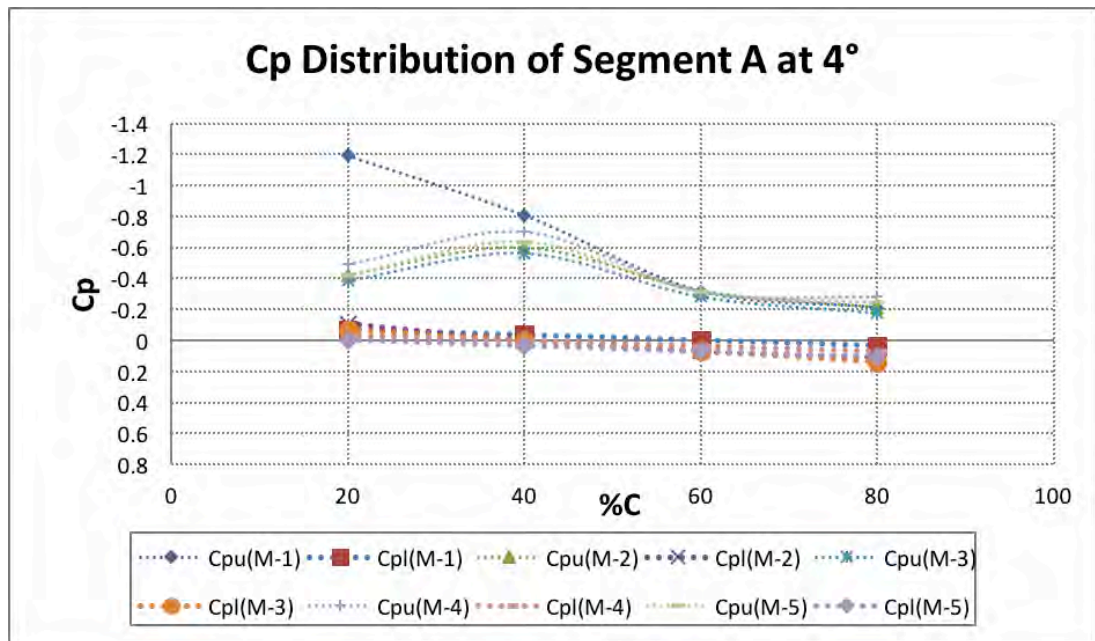


Figure 6.8:  $C_p$  Distribution of Segment-D at  $\alpha = 0^\circ$

### 6.2.3 Pressure Distributions at 4° AOA

The pressure distributions of both upper and lower surface of Model- 1, 2, 3, 4 and 5 planforms at 0° angle of attack for four segments are shown in Figure 6.9, 6.10, 6.11 and 6.12, respectively.

From Figure 6.9 it is observed that pressure difference between the upper and lower surface of Model-1 planform in Segment-A is the highest amongst five planforms. Because, the upper surface pressure of Model-1 planform is higher than that of Model- 2, 3, 4 and 5 planforms up to 40% C. Again it is also seen that the pressure differences between the two surface of Model-4 and 5 planforms are greater than Model- 2 and 3 planforms because of greater pressure difference near the trailing edge of Model- 4 and 5 planforms.



**Figure 6.9:  $C_p$  Distribution of Segment-A at  $\alpha = 4^\circ$**

In Figure 6.10, it is observed that the upper surface pressure of Model- 1 planform in segment-B rapidly decreases from the highest suction pressure at 20% C to the positive pressure at 60% C then again the pressure reaches to the suction side at 80% C. But in case of Model- 2, 3, 4, and 5 planforms, the upper surface pressure always remain at suction side. The difference between upper and lower surface pressure is observed lowest for Model- 1 planform and highest for Model- 4 and 5 planforms. The upper surface pressure of Model- 2, 3, 4 and 5 planforms decrease very slowly from 20% C to 60% C and then decreases rapidly up to 80% C. The upper surface pressure of Model- 2 and 3 planforms is lower than the upper surface

pressure of Model- 4 and 5 planforms. The lower surface of Model- 2 and 3 planforms is having lower positive pressure than that of Model- 4 and 5 planforms.

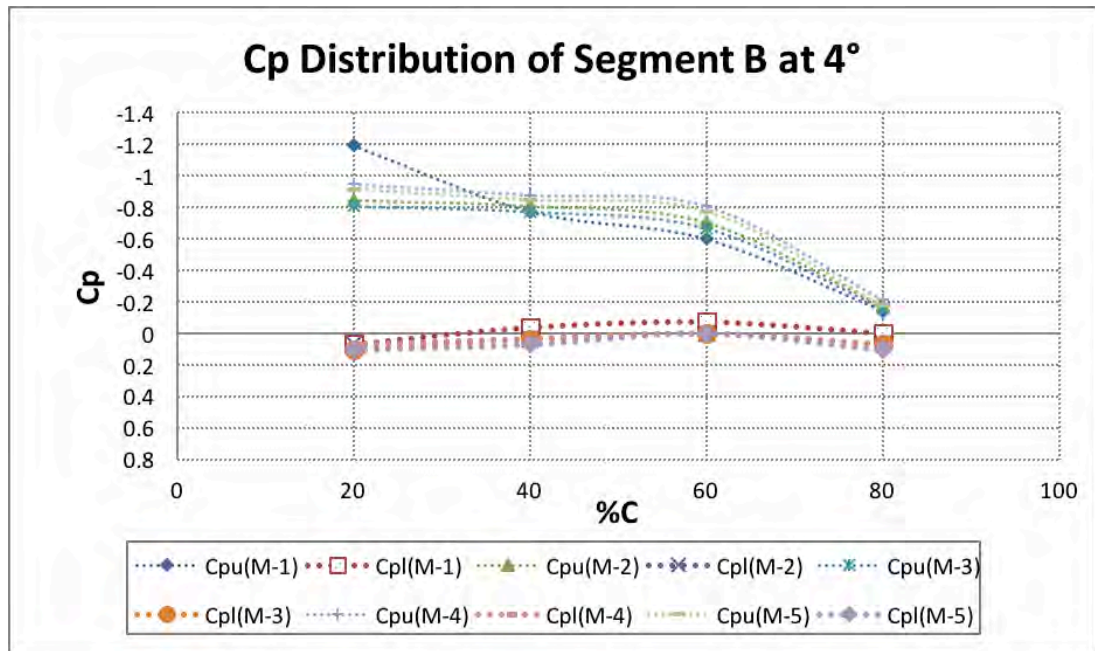


Figure 6.10:  $C_p$  Distribution of Segment-B at  $\alpha = 4^\circ$

Figure 6.11 shows the pressure distribution of segment-C of five planforms. From the figure, it is found that the upper surface suction pressure is highest for Model- 4

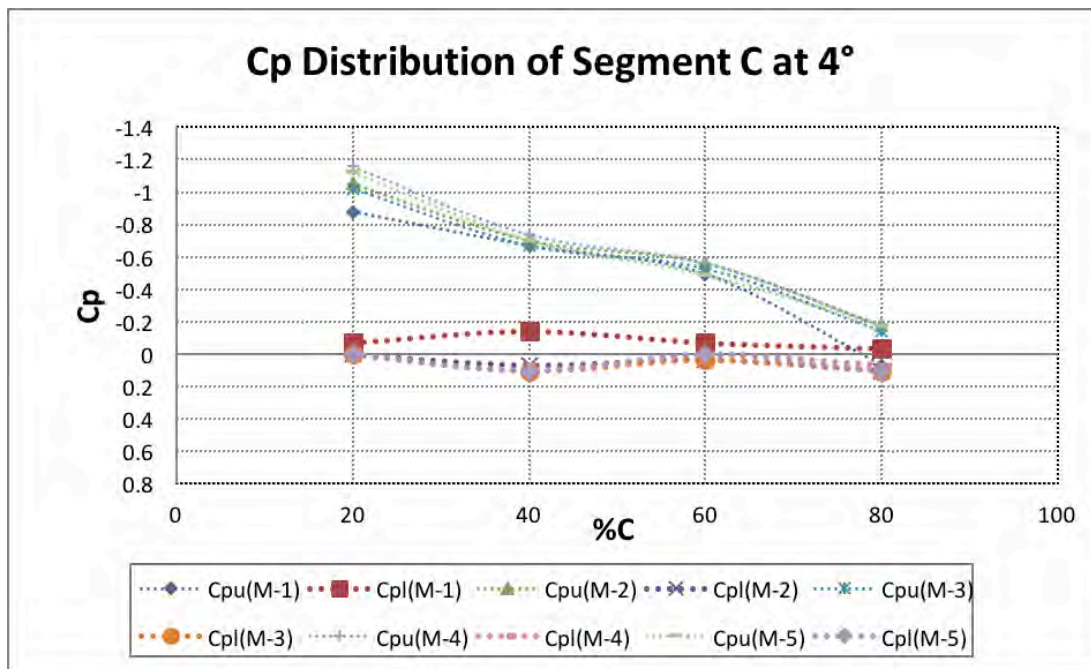
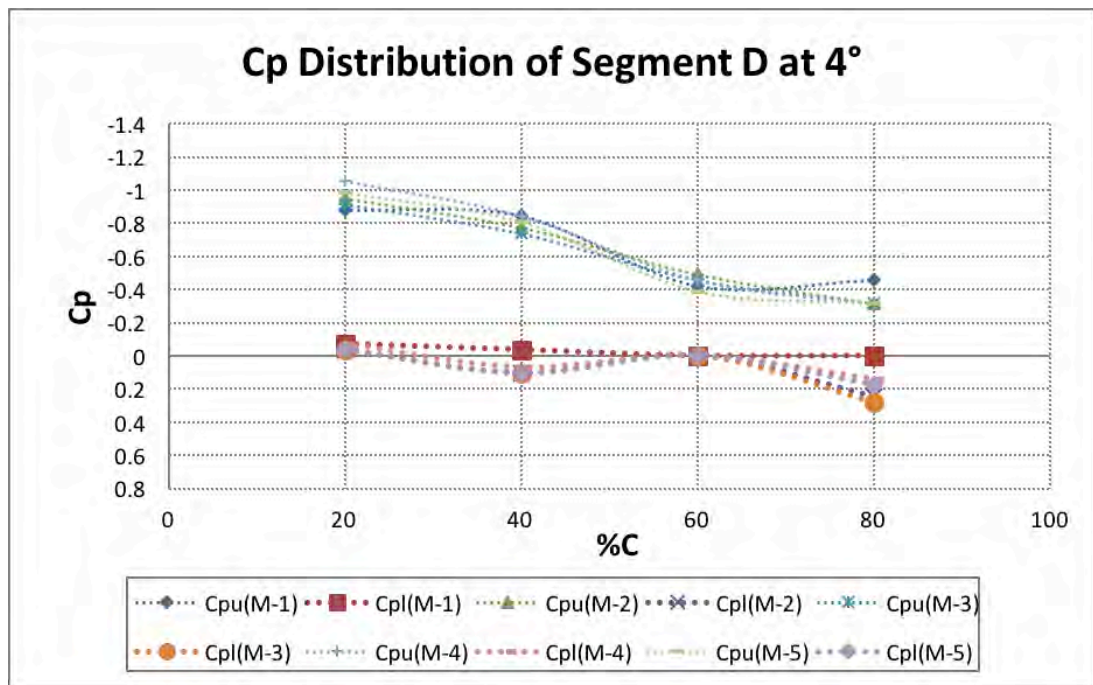


Figure 6.11:  $C_p$  Distribution of Segment-C at  $\alpha = 4^\circ$

and 5 planforms throughout the chord and lowest for Model- 1 planform. The lower surface pressure of Model- 4 and 5 planforms is also highest amongst five planforms. The lower surface pressure for Model- 1 planform mostly remains at the suction side whereas the lower surface pressure of Model- 2, 3, 4 and 5 planforms remain at the positive pressure side. As a result, the pressure difference between the upper and lower surface of Model- 4 and 5 is also at the highest level. In Figure 6.12, It is found that almost similar type of pressure distribution of all five planforms for segment-D are observed as in segment-C. But the difference between two surfaces pressure of respective planforms is lower than that of segment-C.



**Figure 6.12:  $C_p$  Distribution of Segment-D at  $\alpha = 4^\circ$**

#### 6.2.4 Pressure Distributions at $8^\circ$ AOA

At  $8^\circ$  angle of attack, both upper and lower surface pressure coefficient,  $C_{pu}$  and  $C_{pl}$  for four segments of Model- 1, 2, 3, 4 and 5 planforms are plotted along the chord and shown in Figure 6.13, 6.14, 6.15 and 6.16, respectively.

The surface pressure distributions for segment-A of the three planforms at 8° angle of attack are shown in Figure 6.13. From the figure it is seen that upper surface of five planforms are having higher suction pressure than the lower surface pressure of the respective planforms. For Model- 1 planform, the lower surface pressure decreases slowly from 20% C to 40% C, then further decreases slowly up to 60% C and again increases up to the trailing edge. The upper surface pressure decreases gradually from leading edge to trailing edge. For Model- 2, 3, 4 and 5 planforms, upper surface pressure increases from the leading edge up to 40% C, then decreases towards the trailing edge and the lower surface pressure slightly decreases from leading edge to trailing edge. The difference between the upper surface and lower surface pressure of Model- 2 and 3 planforms becomes maximum at 40% C. But the upper surface suction pressure of Model- 4 and 5 planforms is higher than Model- 2 and 3 planforms and lower surface of Model- 4 and 5 planforms is having greater positive pressure than the curved Model- 2 and 3 planforms.

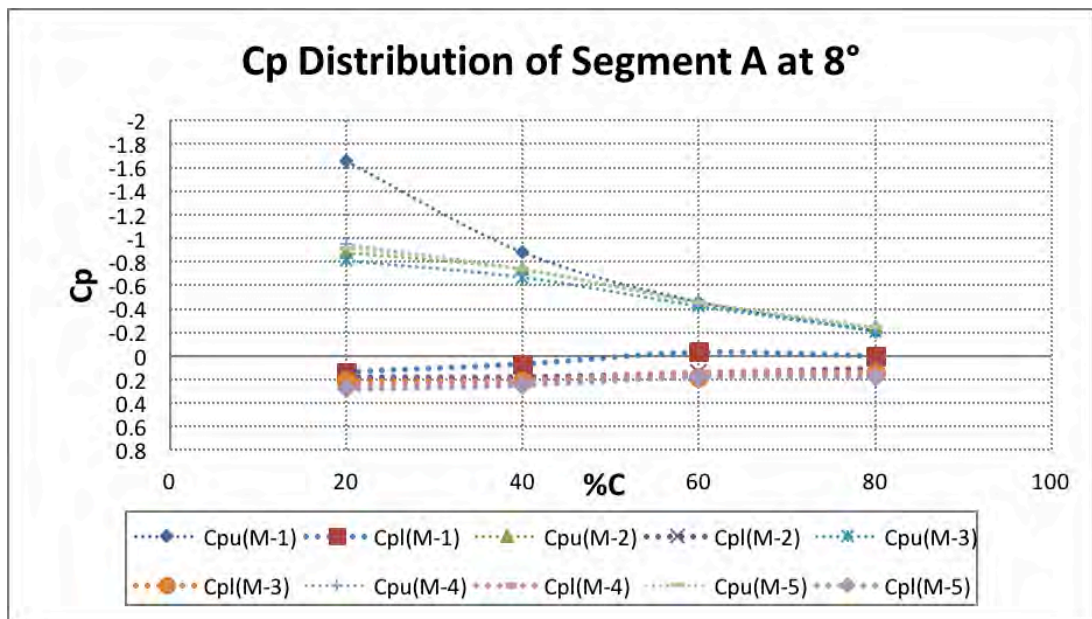


**Figure 6.13:  $C_p$  Distribution of Segment-A at  $\alpha = 8^\circ$**

In Figure 6.14, it is seen that the upper surface pressure of Model- 1 planform in segment-B rapidly decreases from the highest suction pressure at 20% C to the positive pressure at 60% C then again the pressure rises to the suction side at 80% C.

But in case of Model- 2, 3, 4 and 5 planforms, the upper surface pressure always remain at suction side. The difference between upper and lower surface pressure is observed lowest for Model- 1 planform and highest for Model- 4 and 5 planforms. The upper surface pressures of Model- 2, 3, 4 and 5 planforms decrease from 20% C to 80% C. The upper surface pressure of Model- 2 and 3 planforms is lower than the upper surface pressure of Model- 4 and 5 planforms. The lower surface of Model- 2 and 3 planforms is having lower positive pressure than that of Model- 4 and 5 planforms.

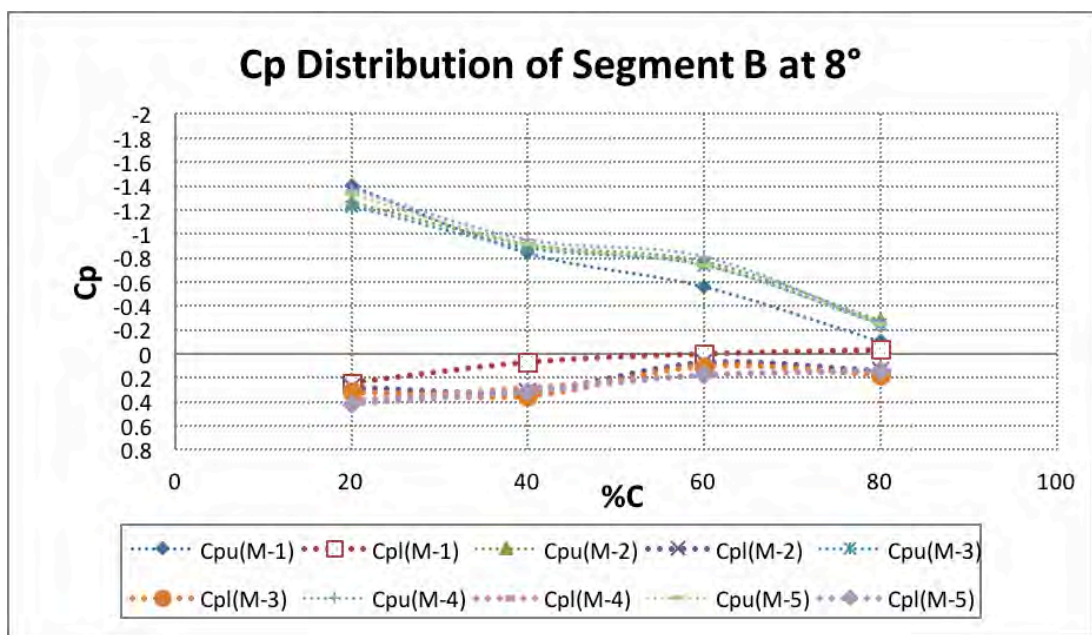


**Figure 6.14:  $C_p$  Distribution of Segment-B at  $\alpha = 8^\circ$**

Figure 6.15 and Figure 6.16 show the pressure distribution of segment-C and segment-D of five planforms respectively. From the figures, it is seen that the upper surface suction pressure is highest for Model- 4 and 5 planforms throughout the chord and lowest for Model- 1 planform. The lower surface pressure of Model- 4 and 5 planform is also highest amongst five planforms. The lower surface pressure for Model-1 planform mostly remains at the suction side whereas the lower surface pressure of Model- 2, 3, 4 and 5 planforms remain at the positive pressure side. As a result, the pressure difference between the upper and lower surface of Model- 4 and



5 planforms is also at the highest level. In segment-D, the difference between two surfaces pressure of respective planforms are lower than those of segment-C.

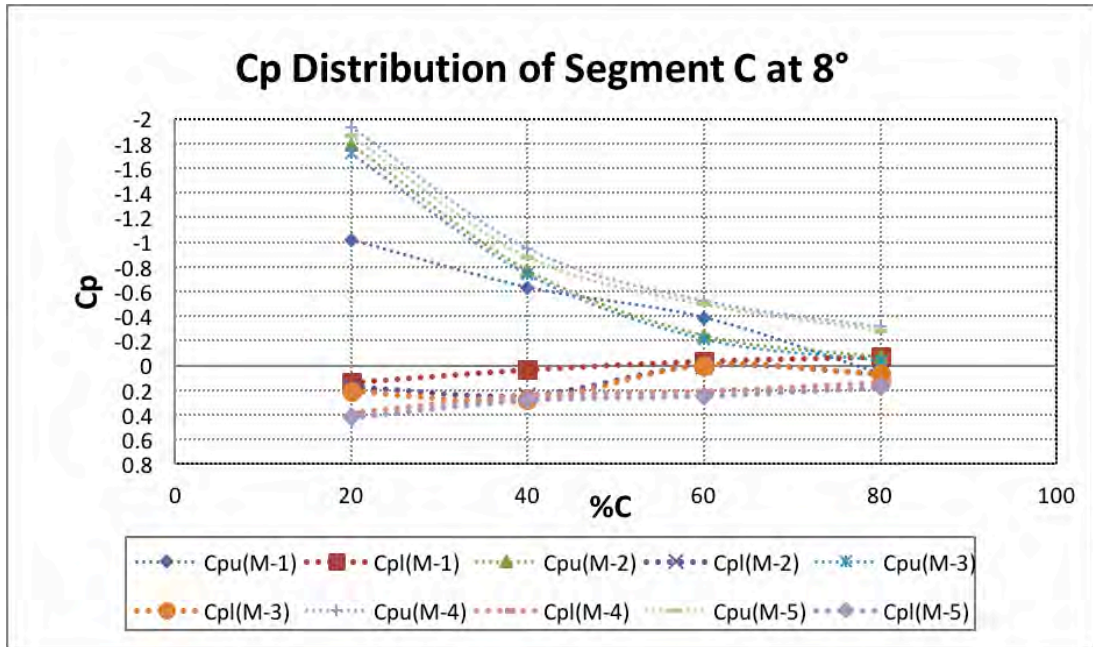


Figure 6.15:  $C_p$  Distribution of Segment-C at  $\alpha = 8^\circ$

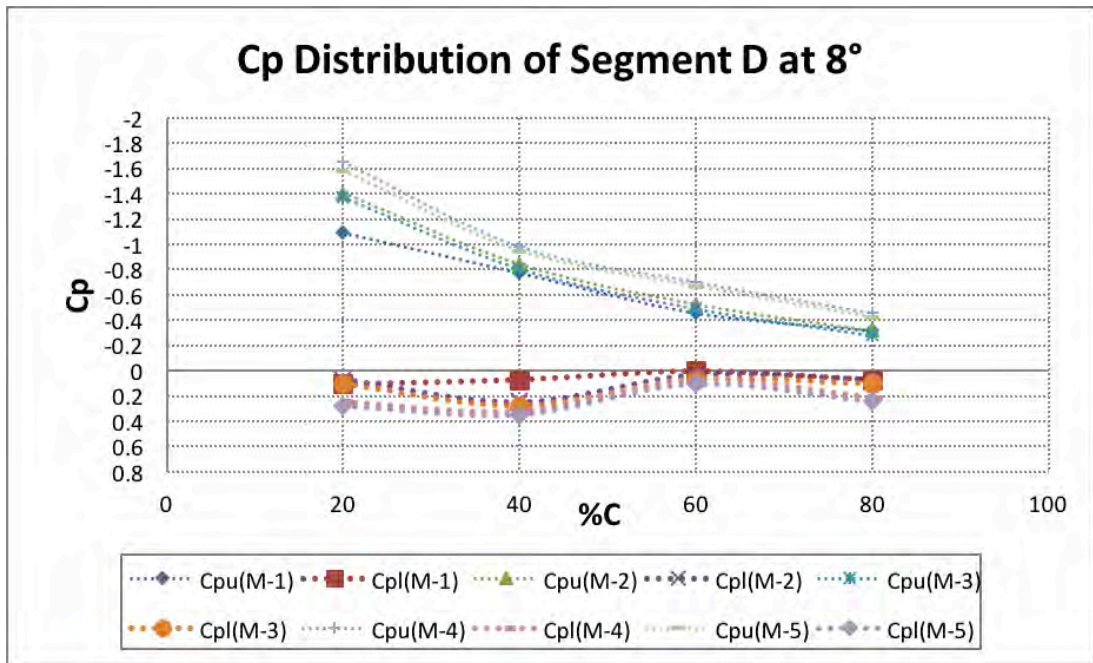
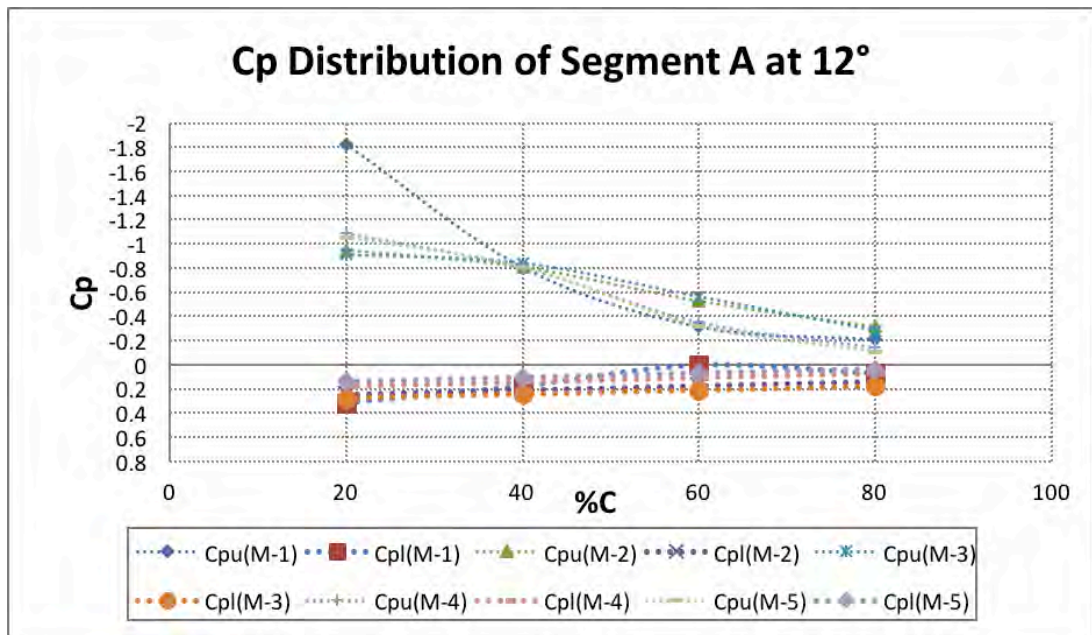


Figure 6.16:  $C_p$  Distribution of Segment-D at  $\alpha = 8^\circ$

## 6.2.5 Pressure Distributions at 12° AOA

Surface pressure distribution at 12° angle of attack for four segments of Model- 1, 2, 3, 4 and 5 planforms are plotted along the chord and shown in Figure 6.17, 6.18, 6.19 and 6.20, respectively.

The surface pressure distributions for segment-A of five planforms at 12° angle of attack are shown in Figure 6.17. From the figure it is observed that upper surface of five planforms are having higher suction pressure than the lower surface pressure of the respective planforms. For Model- 1 planform, the lower surface pressure increases slowly from 20% C up to the trailing edge. The upper surface pressure decreases gradually from leading edge to trailing edge. For Model- 2 and 3 planforms, upper surface pressure increases from the leading edge up to 40% C, then decreases towards the trailing edge and the lower surface pressure increases from leading edge to trailing edge.



**Figure 6.17:  $C_p$  Distribution of Segment-A at  $\alpha = 12^\circ$**

For Model- 4 and 5 planforms, upper surface pressure decreases from 10% C towards the trailing edge and the lower surface pressure increases from leading edge

to trailing edge. The difference between upper surface and lower surface pressure is observed maximum for Model- 1 planform. The upper surface suction pressure of Model- 4 and 5 planforms is higher than Model- 2 and 3 planforms up to 30% C and lower surface of Model- 4 and 5 planforms is having slightly lower positive pressure than Model- 2 and 3 planforms.

From Figure 6.18 for segment-B, it is found that the upper surface suction pressure of five planforms reduces from leading edge to trailing edge and the lower surface positive pressure reduces from leading edge to trailing edge in segment-B. Thus the pressure difference between upper and lower surface is maximum near the trailing edge at 20% C. Also, the overall pressure difference between upper and lower surface is maximum for Model-1 planform and lowest for Model- 4 and 5 planforms in segment-B.

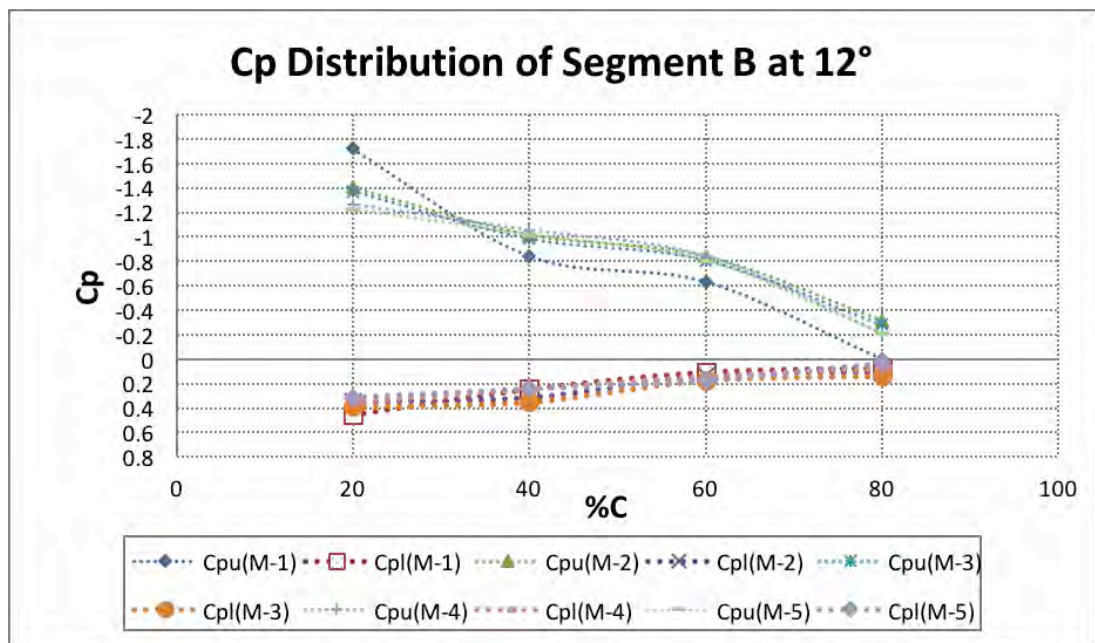
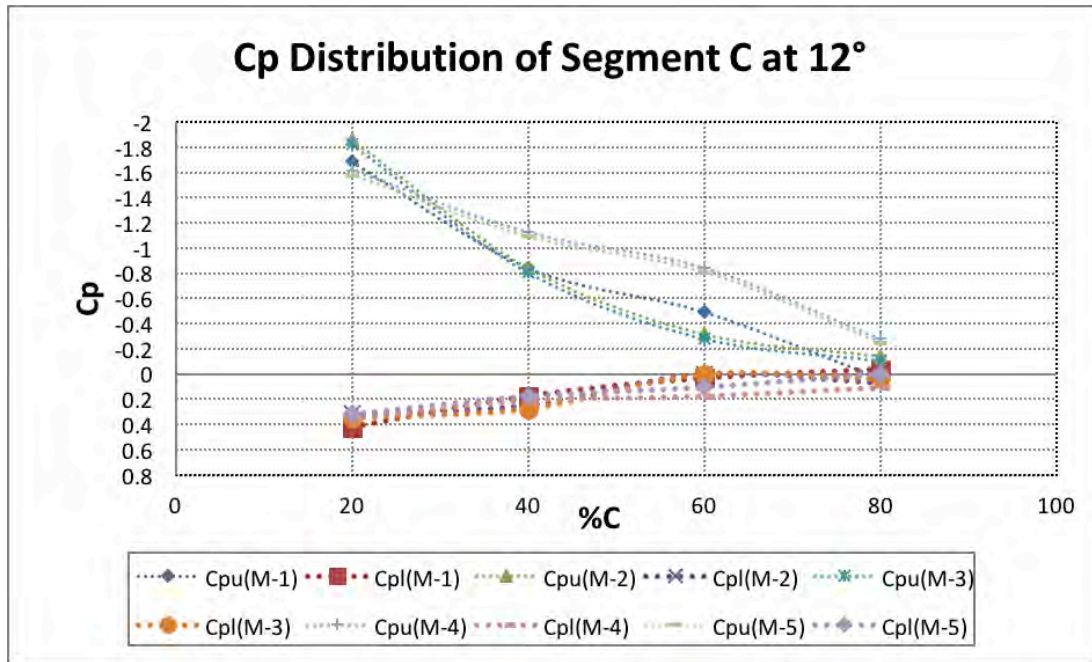


Figure 6.18:  $C_p$  Distribution of Segment-B at  $\alpha = 12^\circ$

But in segment-C in Figure 6.19, the difference between upper and lower surface pressure becomes maximum for Model- 4 and 5 planforms. Because in segment-C, the upper surface suction pressure of Model- 1 planform and Model- 2 and 3 planforms reduces rapidly from leading edge up to trailing edge but for Model- 4 and 5 planforms, the upper surface pressure reduces very slowly up to the trailing edge.



**Figure 6.19:  $C_p$  Distribution of Segment-C at  $\alpha = 12^\circ$**

In segment-D, overall pressure difference between upper and lower surface of all five planforms seems equal as shown in Figure 6.20. It is seen that the upper surface suction pressure of five planforms reduces more rapidly up to 40% C and the lower surface positive pressure increases rapidly up to 60% C. From 60% C to 80% C, the difference between two surfaces pressure of individual planform changes very slowly.

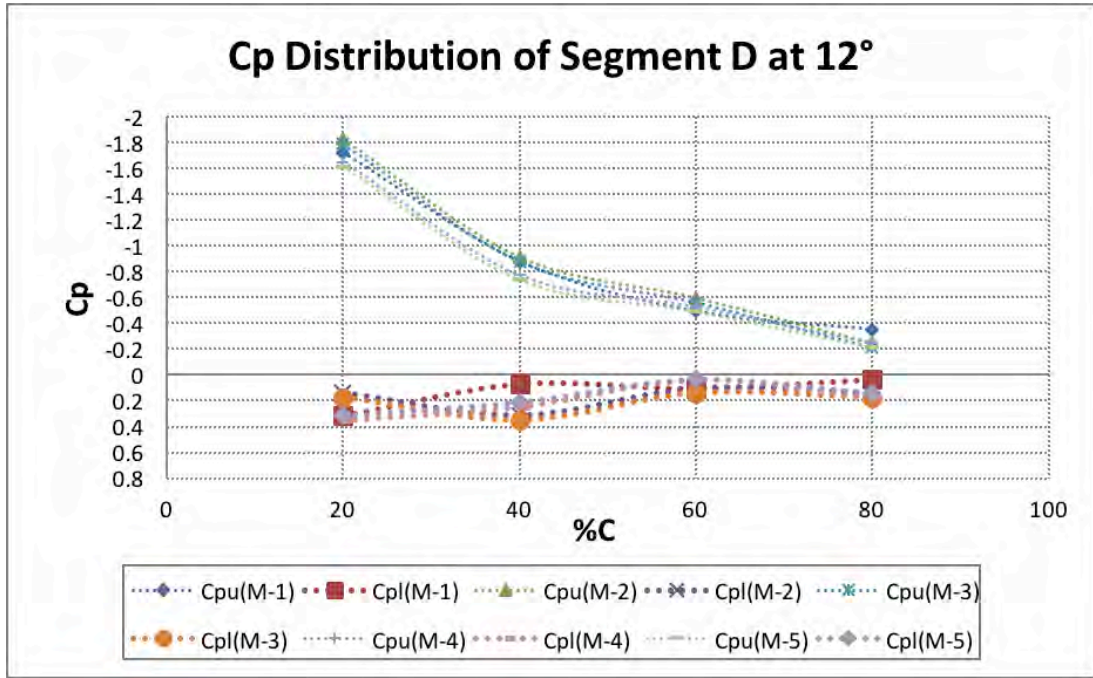


**Figure 6.20:  $C_p$  Distribution of Segment-D at  $\alpha = 12^\circ$**

### 6.2.6 Pressure Distributions at $16^\circ$ AOA

Surface pressure distribution along the chord at  $16^\circ$  angle of attack for four segments of Model- 1, 2, 3, 4 and 5 planforms are shown in Figure 6.21, 6.22, 6.23 and 6.24, respectively. Pressure distribution along the chord for segment-A is shown in Figure 6.21. From the graph, it is observed that upper surface suction pressure of Model-1 planform decreases from 20% C to 40% C rapidly, then decreases slowly up to 60% C and again increases up to 80% C. The lower surface positive pressure gradually decreases up to 60% C and finally reaches to the suction side from 60% C to 80% C. For Model- 2 and 3 planforms, the upper surface suction pressure reduces gradually from leading edge to trailing edge and its lower surface positive pressure increases gradually from leading edge to trailing edge. For Model- 4 and 5 planforms, the upper and lower surface pressure curves follow the similar pattern as those of Model- 2 and 3 planforms. But upper surface of Model- 4 and 5 planforms is having greater suction pressure than that of Model- 2 and 3 planforms and the lower surface of Model- 4 and 5 planforms is having greater positive pressure than Model- 2 and 3 planforms. Thus, Model- 4 and 5 planforms is having greater pressure difference between its two surfaces than Model- 2 and 3 planforms. From the graph it is

evident that the pressure difference between two surfaces of Model- 4 and 5 planforms is also higher than the pressure difference between the surfaces of Model- 1 planforms.

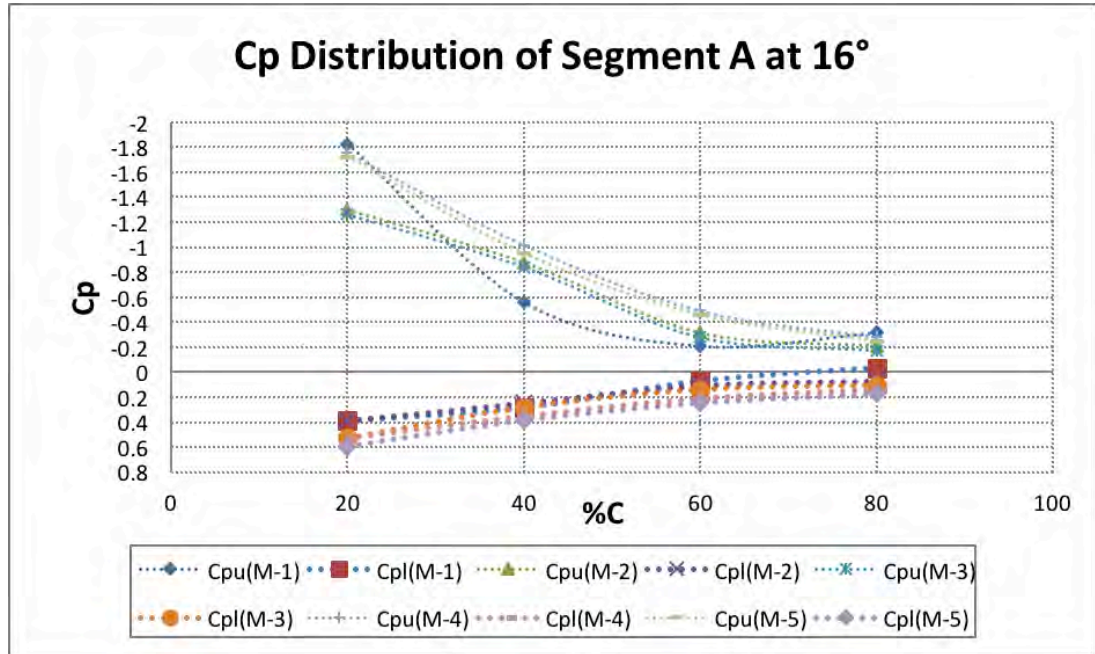


**Figure 6.21:  $C_p$  Distribution of Segment-A at  $\alpha = 16^\circ$**

Similarly, Figure 6.22, 6.23 and 6.24 shows the surface pressure distribution of segment B, C and D respectively for all five planforms at 16° angle of attack. From

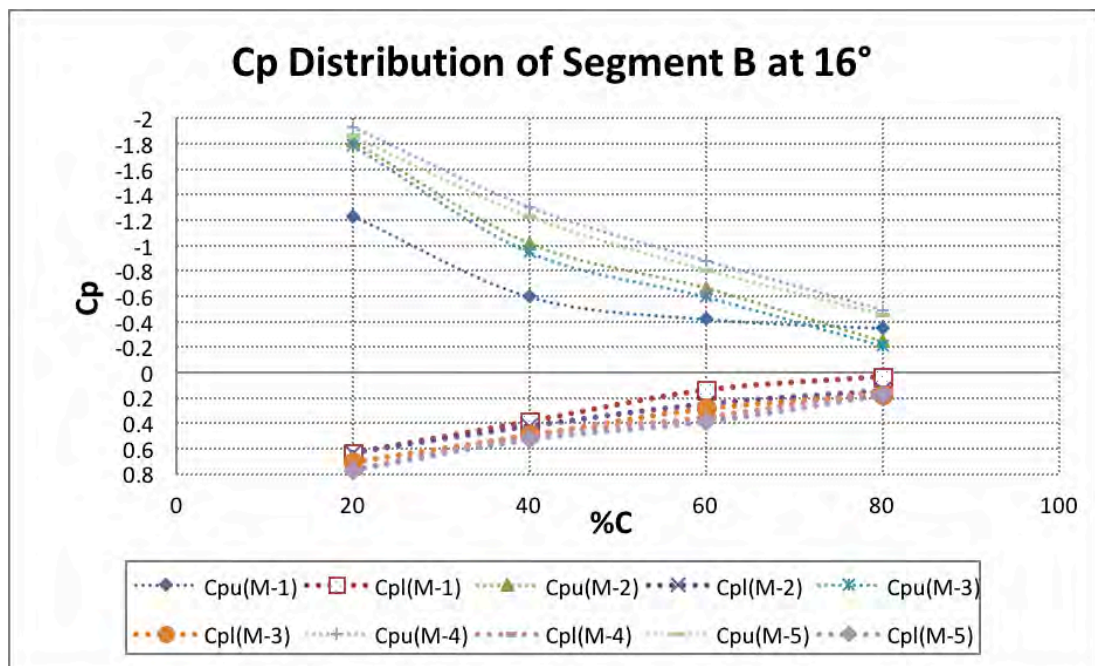


**Figure 6.21:  $C_p$  Distribution of Segment-B at  $\alpha = 16^\circ$**

the figures it is seen that pressure difference between the surfaces of Model- 4 and 5 planforms is higher than Model- 1, 2 and 3 planforms in segment B, C and D.

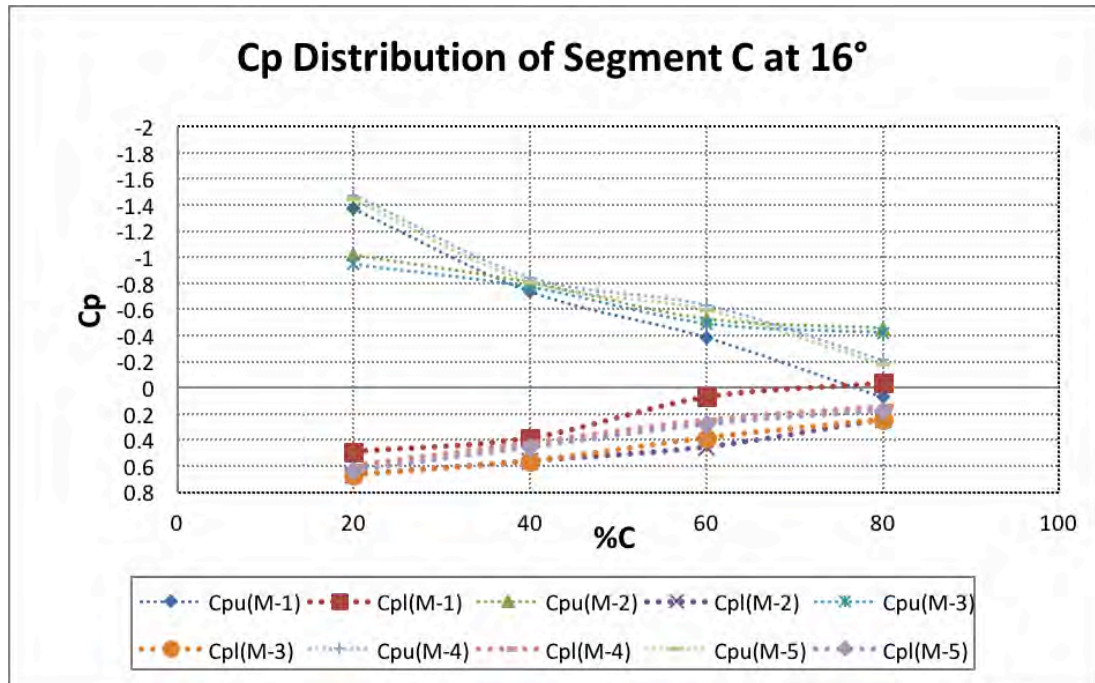


Figure 6.23:  $C_p$  Distribution of Segment-C at  $\alpha = 16^\circ$

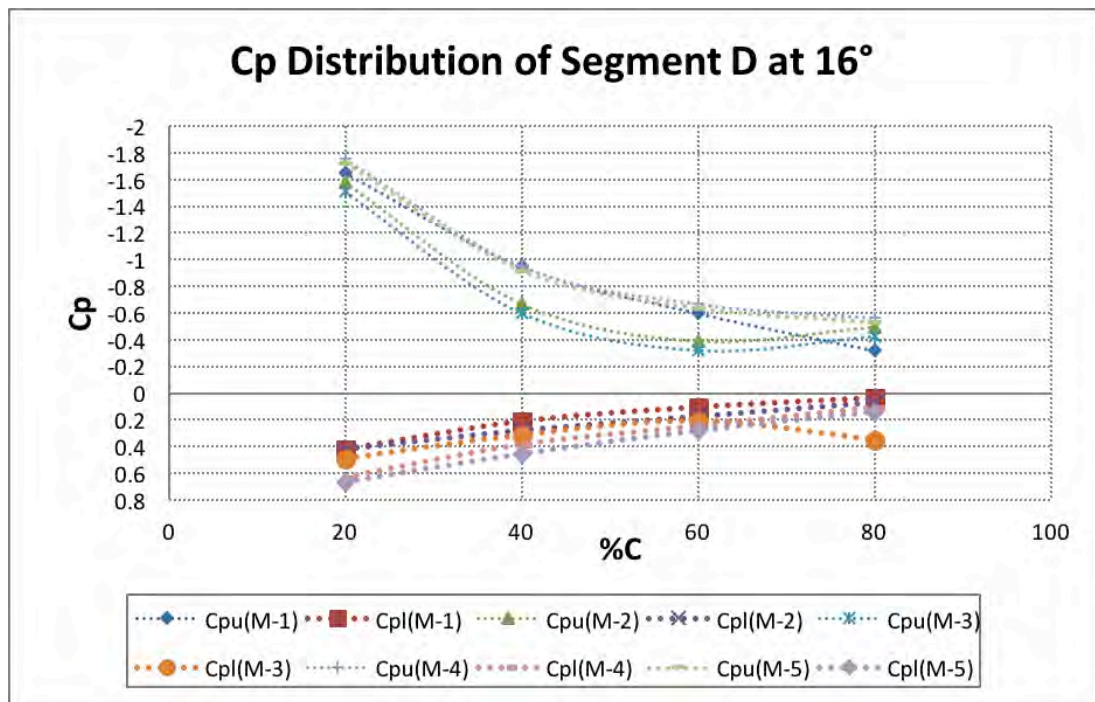


Figure 6.24:  $C_p$  Distribution of Segment-D at  $\alpha = 16^\circ$

### 6.2.7 Pressure Distributions at 20° AOA

The surface pressure distributions along the chord at 20° angle of attack for four segments of all Models are shown as Figure 6.25, 6.26, 6.27 and 6.28 respectively. From all the four figures, it is observed that in all the four segments, the upper surface suction pressure of the Model- 1 is much lower than the upper surface suction pressure at angle of attack 16° and below as shown in the previous figures. For Model- 2 and 3 planforms and Model- 4 and 5 planforms, the reduction in upper surface suction pressure is observed comparatively less than those at the previous angle of attack. In Figure 6.25 and Figure 6.26, the difference between the upper and lower surface pressure of Model- 2 and 3 planforms are seen maximum for segment-A and segment-B. But the said difference is maximum for Model- 4 and 5 planforms in segment-C and segment-D as shown in Figure 6.27 and Figure 6.28.

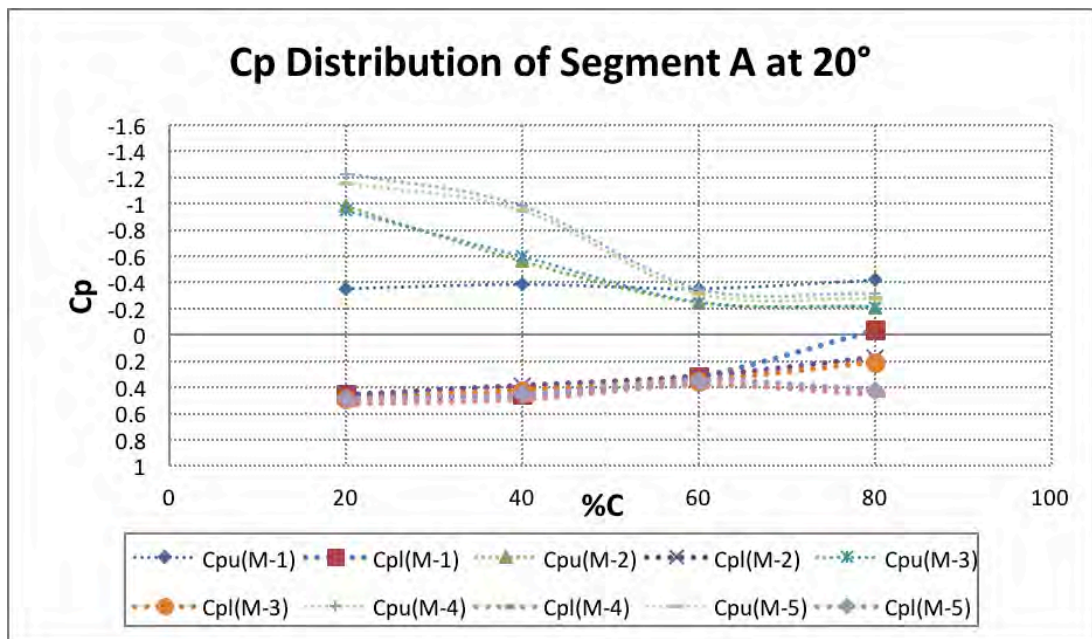


Figure 6.25:  $C_p$  Distribution of Segment-A at  $\alpha = 20^\circ$



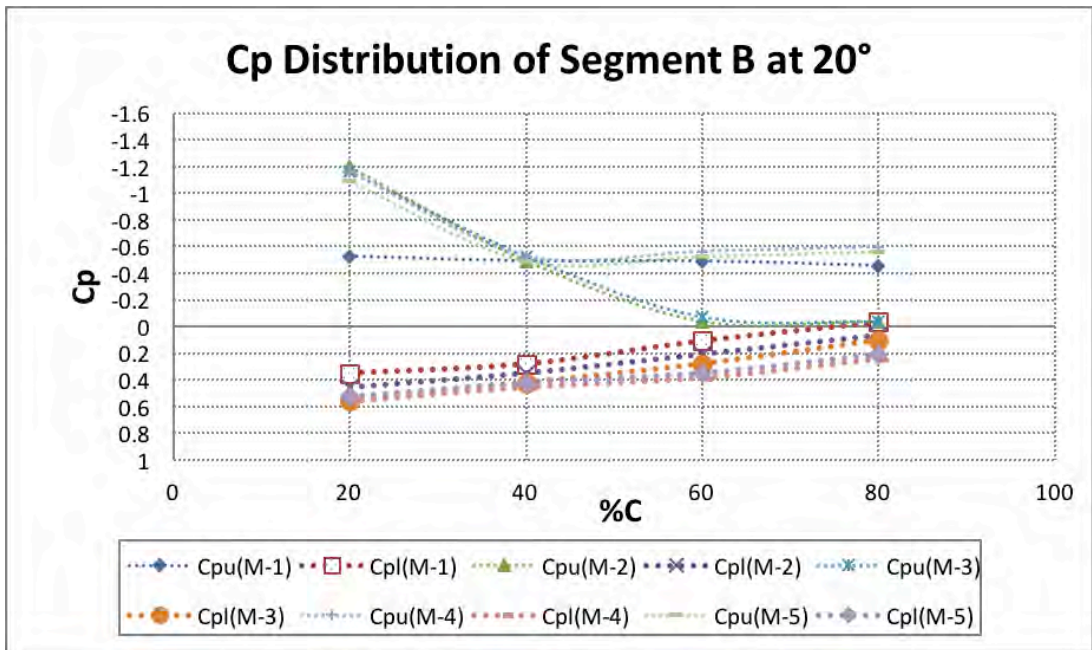


Figure 6.26:  $C_p$  Distribution of Segment-B at  $\alpha = 20^\circ$

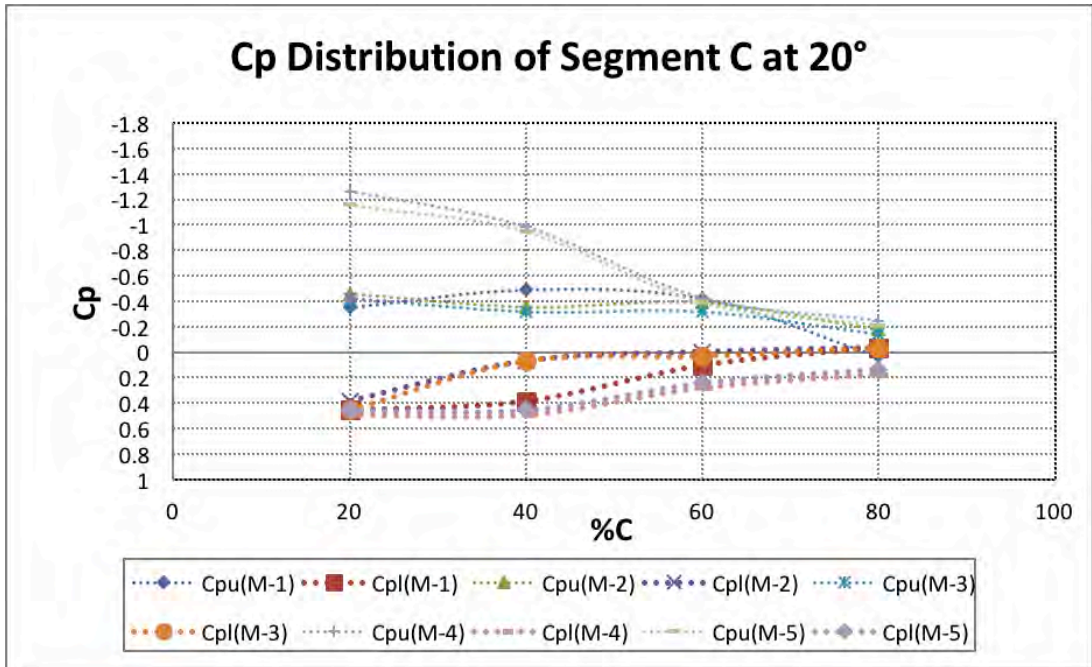
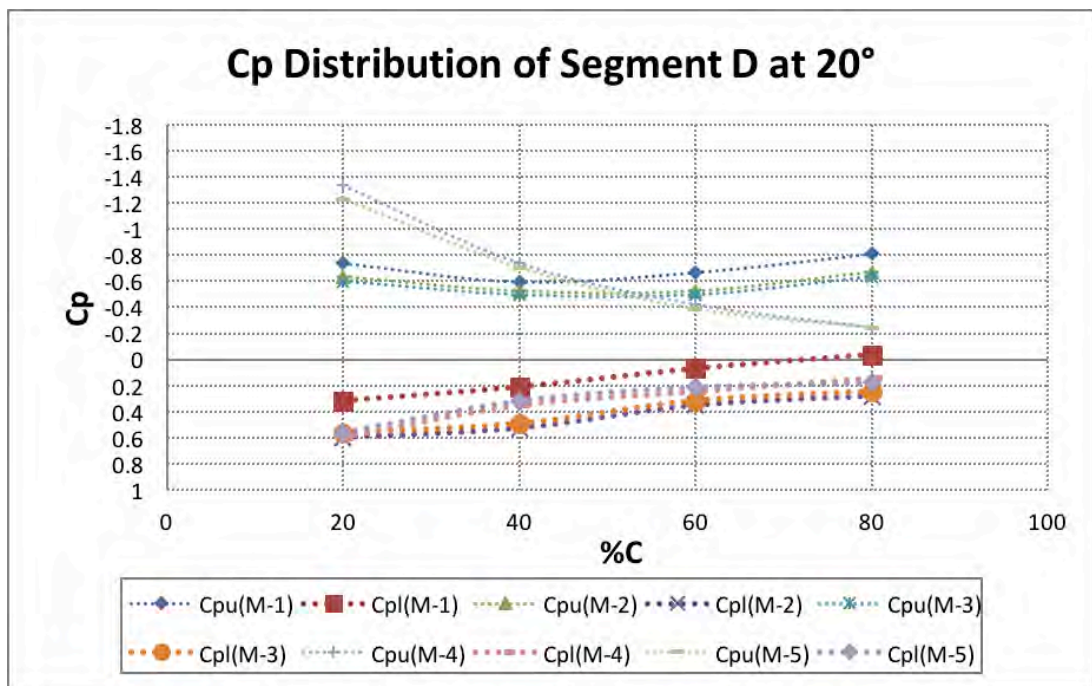


Figure 6.27:  $C_p$  Distribution of Segment-C at  $\alpha = 20^\circ$



**Figure 6.28:  $C_p$  Distribution of Segment-D at  $\alpha = 20^\circ$**

In comparison to the pressure difference of the surfaces of Model- 4 and 5 planforms are higher than Model- 2 and 3. Again, another observation is made from Figure 6.27 and Figure 6.28 is that the upper surface pressure curve of Model-1 and Model- 2 and 3 planforms follow almost similar pattern in segment-C and segment-D.

### 6.2.8 Pressure distribution at $24^\circ$ AOA

The surface pressure distributions along the chord at  $24^\circ$  angle of attack for four segments of all the five planforms are shown as Figure 6.29, 6.30, 6.31 and 6.32, respectively.

In all the four figures, it is observed that the pressure difference between upper and lower surface of all the planforms are very less compared to those at previous angles of attack. But among five planforms, Model- 4 and 5 planforms are having higher pressure difference between upper and lower surfaces at  $24^\circ$  angle of attack as observed in Figure 6.29-6.32.

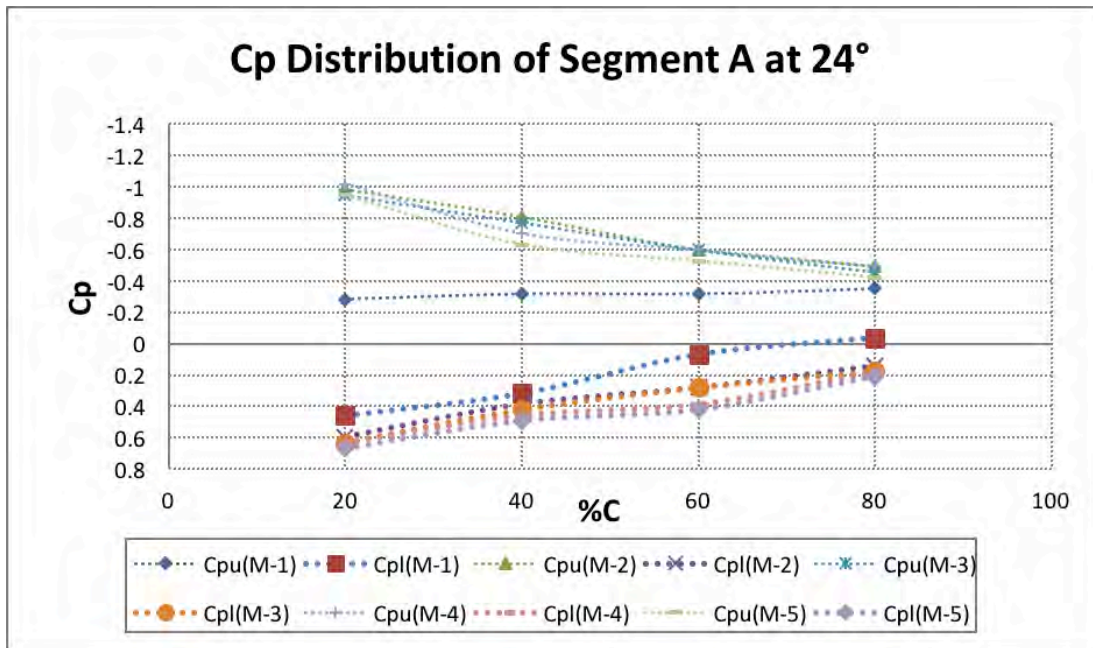


Figure 6.29:  $C_p$  Distribution of Segment-A at  $\alpha = 24^\circ$

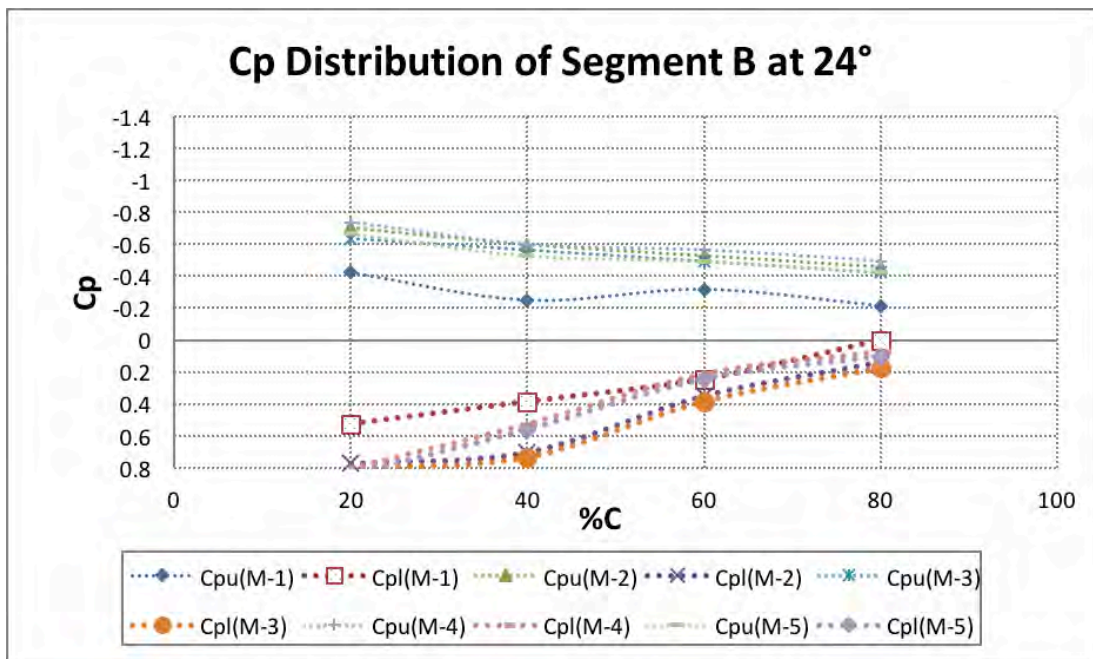


Figure 6.30:  $C_p$  Distribution of Segment-B at  $\alpha = 24^\circ$

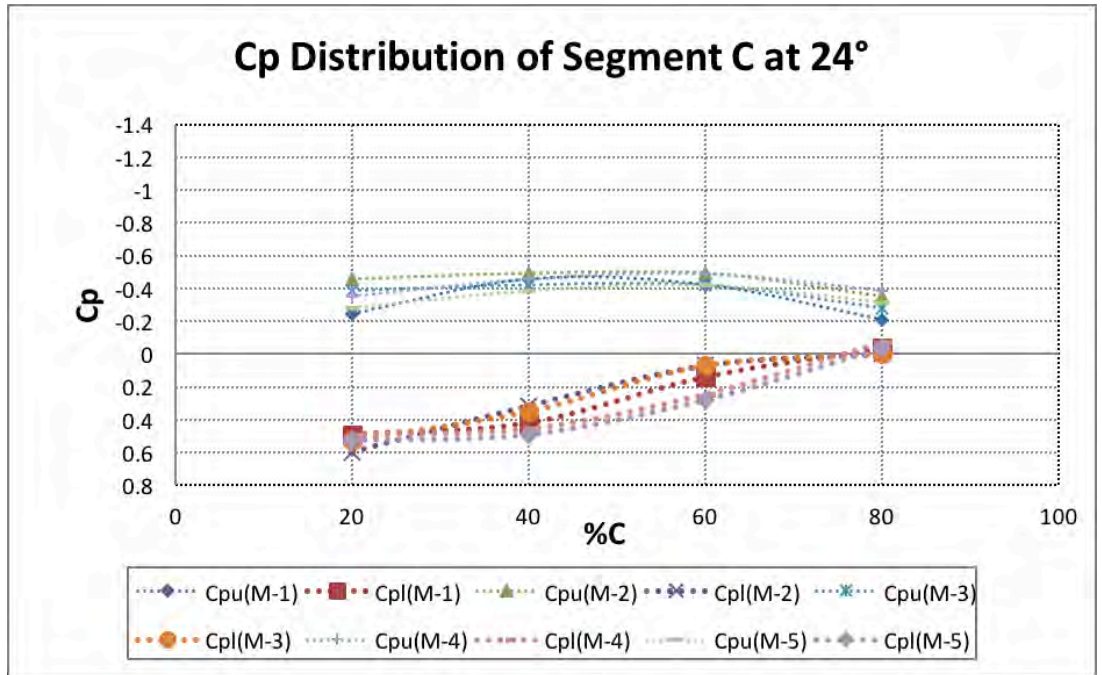


Figure 6.31:  $C_p$  Distribution of Segment-C at  $\alpha = 24^\circ$

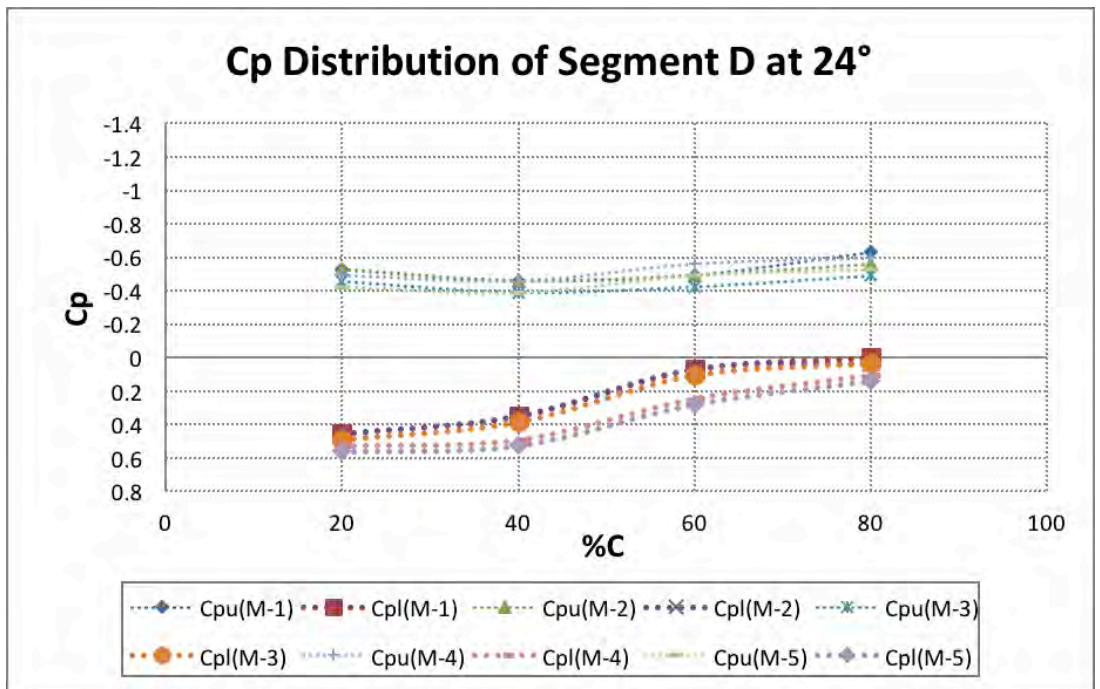
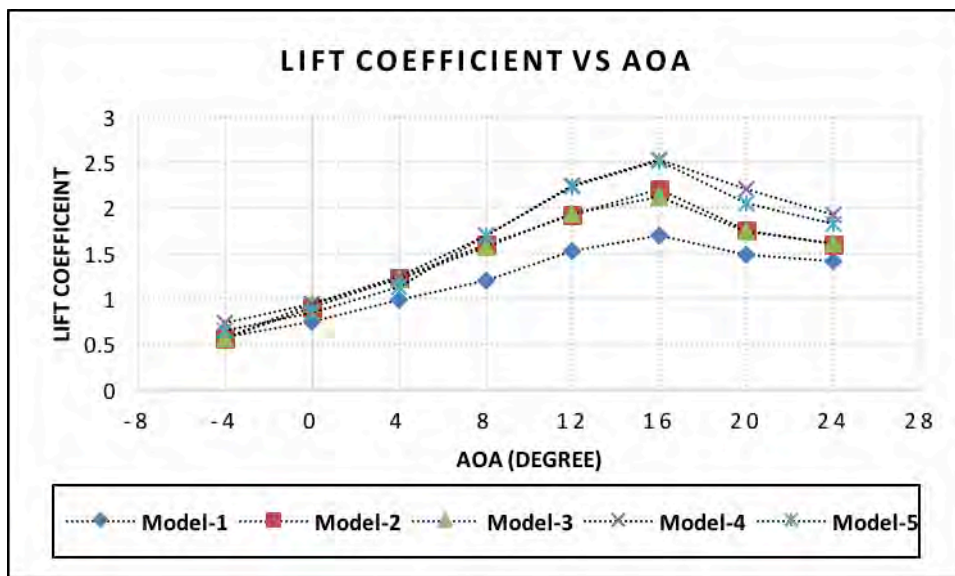


Figure 6.32:  $C_p$  Distribution of Segment-D at  $\alpha = 24^\circ$ .

### 6.3 Lift Characteristics

The lift coefficient characteristics of the five planforms for different angles under test are shown in Figure 6.33. The lift increases with increase in angle of attack to a maximum value and thereby decreases with further increase in angle of attack. It is seen that the lift coefficient curve rises from  $-4^\circ$  angle of attack up to  $16^\circ$  angle of attack for all the planforms and then falls rapidly beyond  $16^\circ$  angle of attack. Thus, the critical angle of attack of all the five planforms remain around  $16^\circ$  beyond which the stall occurs. Lift coefficient for Model- 4 and 5 planforms is observed much higher than that of Model- 1, 2 and 3 planforms. The difference between the values of lift coefficient of Model- 4 and 5 planforms and Model- 1, 2 and 3 planforms are observed highest at  $16^\circ$  angle of attack. So, it can be concluded that the optimum angle of attack is at around 16 degrees. The reason is that at this range the ratio between the coefficient of lift and the angle of attack is at its maximum. As a result, it is reasonable to assume that in order to obtain maximum lift from NACA 4412 airfoil, the wing needs to be positioned at around 16 degrees with respect to the flight path.



**Figure 6.33: Variation of Lift Coefficient with Angle of Attack.**

These statistics show the similar nature to Ghods analysis [3], Nazmul analysis [27] and National Aerofoil Data NACA 4412 [28].

## 6.4 Drag Characteristics

The drag coefficients of the wing planforms under test for different angle of attack (AOA) are shown in Figure 6.34. The drag increases slowly with increase in angle of attack to a certain value and then it increases rapidly with further increase in angle of attack. It is observed that the values of drag coefficient for Model-4 and 5 planforms are much lower than that of the Model- 1, Model- 2 and Model- 3 planforms. The significant reduction of drag of curved Model- 4 and 5 planforms is observed from  $8^\circ$  to  $24^\circ$  angle of attack. It is seen that after the peak occurs at  $16^\circ$  and the coefficient of drag starts increasing at an exponential rate. This exponential rate of increase demonstrates that if the angle of attack is increased any further the drag will dominate lift and stall will occur. These statistics show the similar nature to Ghods analysis [3], Nazmul analysis [27] and National Aerofoil Data NACA 4412 [28].

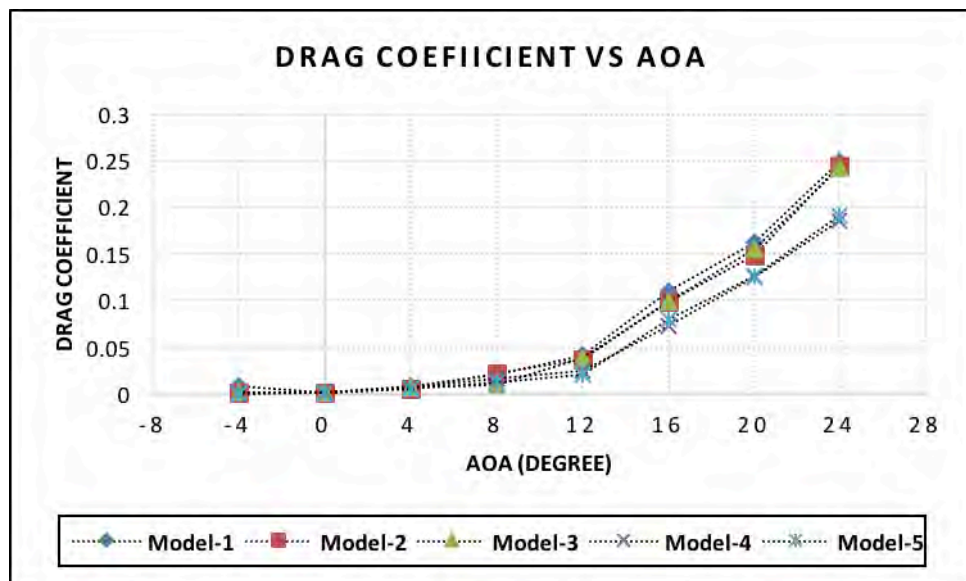


Figure 6.34: Variation of Drag Coefficient with Angle of Attack.

## 6.5 Lift to Drag Ratio

The values of lift to drag ratio are plotted for various angle of attack in Figure 6.35. It is found that the lift to drag ratio of Model-2 and 3 planforms wing is higher than that of Model- 1 planform. It is also observed from the graph that the lift to drag ratio of Model- 4 and 5 planforms is higher than that Model- 2 and 3 planforms and the Model- 1 planform for all angles of attack. For  $-4^\circ$  angle of attack, lift to drag ratio of Model- 4 and 5 wing planforms is observed significantly higher (Model- 4 is higher than Model- 5) than other three planforms. It is also found that the drag is lowest for the curved trailing edge (Model- 4 and 5) planforms among the five experimental wings. The curved leading edge (Model- 2 and 3) planforms also produce less drag than the rectangular (Model- 1) planform. The results from testing the existing wing section are close to the theoretical results from the National Airfoil Database [46]. From all the analysis, it is seen that Model- 4 and 5 planforms are better lift characteristics due to less drag. These statistics show the similar nature to Nazmul analysis [27] and National Aerofoil Data NACA 4412 [28].

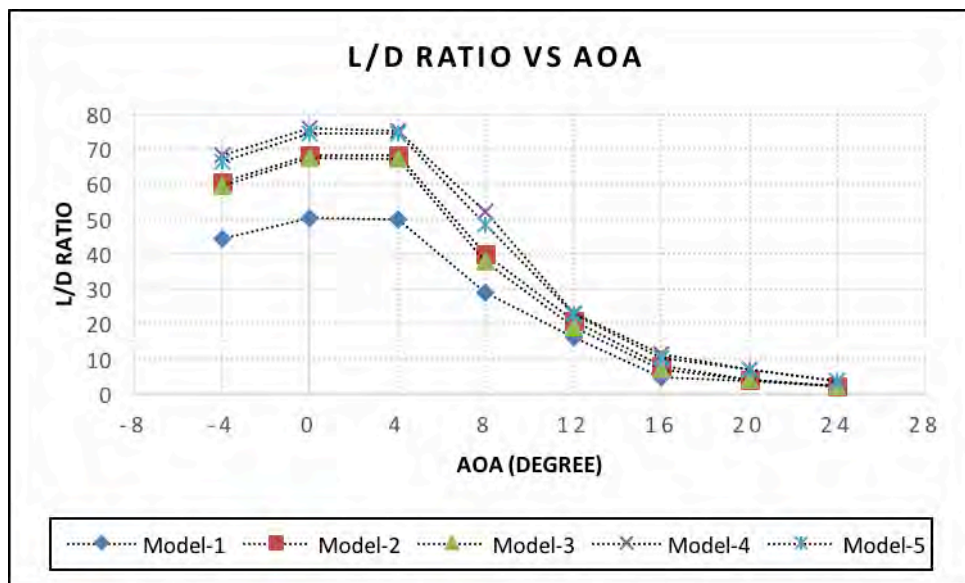


Figure 6.35: Variation of Lift to Drag Ratio with Angle of Attack

## CONCLUSIONS AND RECOMMENDATIONS

### 7.1 Conclusions

An investigation of the wing concept of aerofoil is primarily concentrated on the study of aerodynamic characteristics of the aircraft. From the experiment that has been conducted on the wing planforms of aircraft and data has been tabulated and curves of lift coefficient, drag coefficient and lift to drag ratio versus angle of attack have been plotted. From these data it can be made few conclusions regarding the model aerodynamic performance at various angles of attack.

In an aircraft, lift is caused by an upward force that is resulted from the difference in pressure between the top and the bottom surface of the wings. This difference in pressure is due to the special shape of the airfoil, and the amount of this lift is dependent upon the angle at which the wing is inclined. In this research, curved boundary is integrated at the leading edge and trailing edge of Model- 2, 3, 4 and 5 planforms in such a way so that the surface area from the middle of the wing towards the root increases and the area decreases in the same rate towards the tip. But the total surface area of the wings remains same as of the Model- 1 planform.

As it is observed from the analysis of surface pressure distribution, the difference in upper and lower surface pressure of the curved-edge wing planforms (Model- 2, 3, 4 and 5) near the root (in segment-A and segment-B) are higher than the pressure difference near the tip (in segment- C and segment- D). Thus, the curved-edge wing ( Model- 2, 3, 4 and 5) planforms can produce more lift due to increased surface area near the root of the wings. It is also seen that near the tip (in segment- C and segment- D), the difference between upper and lower surface pressure of curved-edge (Model- 2, 3, 4 and 5) planforms is comparatively higher than that of the



rectangular (Model- 1) planform. This phenomenon happened as tip loss of the curved-edge wing (Model- 2, 3, 4 and 5) planforms is reduced due to reduction of chord length at the tip.

From the analysis of variation of lift coefficient with angle of attack, it is found that the critical angle of attack for curved-edge (Model- 2, 3, 4 and 5) planforms remains around  $16^\circ$  as of the rectangular (Model-1) planform. So, stalling occurs after  $16^\circ$  angle of attack for all five wing planforms. The curved trailing edge (Model- 4 and 5) planforms exhibit the best lift characteristics among the five planforms because they have better lift coefficient, lower draw coefficient and better lift to drag ratio. So it is found that for a given wing area, a wing of high aspect ratio (Span/Avg Chord) will produce less induced drag than a wing of low aspect ratio because there is less air disturbance at the tip of a longer and thinner wing. By changing the airfoil section near the wingtips allows more lift to be generated nearer the wing root and less towards the wingtip. Thereby, the curved-edge wing planforms can produce more lift due to increased surface area towards the root of the wings.

The results from testing the existing wing section are close to the theoretical and practical results of Nazmul Analysis [27], National Airfoil Database NACA 4412 [28] and Ghods analysis [3] which validate the result of this research. As a final comment, curved trailing edge planform model may be considered by the aircraft designers and engineers to design a wing model with a view to reducing the drag for efficient flying.

## 7.2 Recommendations for Future Works

The wing is a very important component, and the results obtained in this study demand further work be done to characterize the overall performance over a larger set of flow regimes. As such the author would like to make the following recommendations for future work in this field:

- a. The research on NACA airfoils may be conducted at higher speed wind tunnel to analyze the variation of aerodynamic characteristics of slant/curved-edge planforms with the variation of air speed or Mach number and also to validate by Computation Fluid Dynamics (CFD) simulations.
- b. Using material to construct a wing is significant to obtain efficient performance. To reduce friction from wooden-plastic made wing, researcher a softer type of fiberglass may be used to cover the wing to decrease the friction between air and the wing surface and compared with the obtained results.
- c. Flaps may be incorporated at any suitable location at the leading edge and/trailing edge to analyze the aerodynamic characteristics of curved-edge wing planforms with and without flaps.
- d. The coefficient of moment of the curved-edge wing planforms may be determined and compared with that of the rectangular planform to analyze the aerodynamic stability characteristics of the wings.
- e. Different types of airfoils other than NACA 4412 may be used for the wing planforms to analyze the aerodynamic characteristics of the wings by experimentally and compared with the result of simulations.

- f. All the models should be tested at higher speeds, so that the critical Reynolds number may be attained.
  
- g. In this research work, the winglet concept may be developed to observe the lift coefficient and drag coefficient and compare the results with a view to developing an efficient wing shape in an aircraft design.

## REFERENCES

- [1] Lynch, F.T., “Commercial Transports- Aerodynamic Design for Cruise Performance Efficiency.” *Progress in Astronautics and Aeronautics*, Vol. 81, pp. 81-144, 1982.
- [2] Hossain, A., Rahman, A., Iqbal, A.K.M.P., Ariffin, M., and Mazian, M., “Drag Analysis of an Aircraft Wing Model with and without Bird Feather like Winglet”, *Int. J. of AE and Mech Engg*, Vol. 6, pp. 8-13, 2012.
- [3] Ghods, M., *Theory of Wings and Wind Tunnel Testing of a NACA 2415 Airfoil*, M.Sc. Engg. Thesis, Department of Mechanical Engineering, The University of British Columbia, 2001.
- [4] Dash, A., “CFD Analysis of Wind Turbine Airfoil at Various Angles of Attack, “*Journal of Mechanical and Civil Engineering*, Vol 13, pp. 18-24, 2016.
- [5] Mineck, R.E., and Vijgen P.M.H.W., “Wind-Tunnel Investigation of Aerodynamic Efficiency of Three Planar Elliptical Wings with Curvature of Quarter-Chord Line” *NASA Technical Paper 3359*, pp.1-20, 1993.
- [6] Recktenwald, B., “ Aerodynamic of a Circular Plan form Aircraft”. *American Institute of Aeronautics and Astronautics 022308*, pp.1-7, 2008.

- [7] Wakayama, S., “Subsonic Wing Plan form Design Using Multidisciplinary Optimization”. *Journal of Aircraft*, Vol. 32, pp. 746-753, 1995.
- [8] Paulo, F.R., Bento, S.M., Roberto, M.G., and Pedro, P., “Wing Plan from Optimization of a Transport Aircraft”, *22<sup>nd</sup> Applied Aerodynamics Conference Rhode Island, U.S.A*, pp.1-14, 2004.
- [9] Dwivedi, Y.D., Prasad, M.S., and Dwivedi, S., “Experimental Aerodynamic Static Stability Analysis of Different Wing Planforms”, *Int. J. of Advancements in Research & Technology*, Vol. 2, pp. 60-63, 2013.
- [10] Mahmud, M.S., “Analysis of Effectiveness of an Airfoil with Bicamber Surface”, *International journal of Engineering and Technology*, Vol. 3 No.5, May 2013, pp. 569-577.
- [11] Kandwal, S., and Singh, S., “Computational Fluid Dynamics Study of Fluid Flow and Aerodynamic Forces on an Airfoil.” *International Journal of Engineering and Technology*, Vol. 1, pp. 1-8, 2012.
- [12] Robert, M.P., “The Variation with Reynolds Number of Pressure Distribution over an Airfoil Section”, *NACA Report No. 613*, pp.65-84, 1938.
- [13] Sharma, A., “Evaluation of Flow Behavior around an Airfoil Body”, M. Engg Thesis, Department of Mechanical Engineering, Thapar University, Patiala 147004, India, pp. 1-60, 2012.
- [14] Wells, A.J., “*Experimental Investigation of an Airfoil with Co-flow Jet Flow Control*”, M Sc Thesis, University of Florida, 2005.

- [15] Demasi, L., “*Aerodynamic Analysis of Non-conventional Wing Configurations for Aero-Elastic Applications*”, Ph D Dissertation, Politecnico di Torono, 2004.
- [16] Ismail, L.W., “Investigation of Load and Pressure Distribution on Wing with Wake Rollup for Low Speed Aircraft”, *Al-Khwarizmi Engineering Journal*, Vol. 4, pp. 59-68, 2008.
- [17] McArthur, J., “*Aerodynamics of Wings at Low Reynold Numbers: Boundary Layer Separation and Reattachment*”, PhD Dissertation, University of Southern California, 2008.
- [18] Hassan, I. A., DARwish, A. S., and Jaffal, H. M., “Theoretical and Experimental Study of a Forward Swept Wing”, *Anbar Journal for Engineering Sciences*, Vol.3, pp. 15-30, 2010.
- [19] Ahmed, M. R., “Aerodynamics of a Cambered Airfoil in Ground Effect”, *International Journal of Fluid Mechanics Research*, Vol. 32, pp. 157-183, 2005.
- [20] Alam, G. M. J., “Interference Effect and Flow Pattern of Four Biplane Configurations using NACA 0024 Profile”, *Proceedings of The International Conference on Mechanical Engineering, Dhaka Bangladesh*, 2011.
- [21] Walter, D. J., “*Study of Aerofoils at High Angle of Attack, in Ground Effect*”, M.Sc. Thesis, School of Aerospace, Mechanical & Manufacturing Engineering, RMIT University, Australia, 2007.
- [22] Al- Kayiem, H, H. and Kartigesh, A K., “An Investigation on the Aerodynamic Characteristics of 2-D Airfiol in Ground Collision,

*Journal of Engineering Science and Technology*, Vol.6, pp. 369-381, 2011.

- [23] Janiszewska, J.M., “*Three Dimensional Aerodynamics of a Simple Wing in Oscillation Including Effects of Vortex Generators*”, PhD Dissertation, Graduate School of Ohio State University, 2004.
- [24] Arora, P. R., Hossain,A., Edi, P., Jaafar, A. A., Younis, T. S., and Saleem, M., “Drag Reduction in Aircraft Model using Elliptical Winglet”, *Journal of The Institute of Engineers, Malaysia*, Vol. 66, pp. 1-8, 2005.
- [25] Mashud, M., and Hossain, M. F., “*Experimental Study of Flow Separation Control of an Airfoil by Suction and Injection*”, Proceedings of the 13<sup>th</sup> Asian Congress of Fluid Mechanics, *Dhaka, Bangladesh*, pp. 166-169, 2010.
- [26] Sahin I. and Acir A., “Numerical and Experimental Investigations of Lift and Drag Performances of NACA 0015 Wind Turbine Airfoil”, *Int. J. of Materials, Mechanics and Manufacturing*, Vol. 3, pp. 15-19, 2015.
- [27] Nazmul M. and Ali M. “*An Experimental Investigation on the Aerodynamic Characteristics of NACA 4412 Aerofoil with Curved-Edge Planform*”, M.Sc. Thesis, Mechanical Engineering, BUET, Dhaka-1000, Bangladesh, 2015.
- [28] *National Aerofoil Data NACA 4412*, Online data, <http://airfoiltools.com/airfoil/details?airfoil=NACA4412-il>
- [29] Anderson, J.D., “*Fundamentals of Aerodynamics*”, *McGraw-Hill Series in Aeronautical and Aerospace Engineering*, 3<sup>rd</sup> Edition, pp. 15-22, 2010.

- [30] Kermode, A.C., "*Flight without Formula*", Pitman, 8<sup>th</sup> edition 1970.
- [31] Clancy, L.J., "*Aerodynamics*", John Wiley, New York, 1975.
- [32] Abbott, I. H. and Doenhoff, A.E.V., "Theory of Wing Sections including a Summary of Aerofoil Data", *Dover Publications*, New York, 1990.
- [33] Ramesh, P., "*Numerical and Experimental investigation of the effect of geometry modification on the Aerodynamic characteristics of a NACA 64 (2)-415 wing*", M.Sc. Thesis, Royal Institute of Technology, Stockholm, Sweden, 2013.
- [34] Laurence, K. L. Jr. and Poteat, M. I., "Aerodynamic Characteristics of several NACA airfoil sections at seven Reynolds number from  $0.7 \times 10^6$  to  $9.0 \times 10^6$ ", *Langley Memorial Aeronautical Laboratory*, 1948.
- [35] Eppler, R., "*Airfoil Design and Data*", Springer-Verlag, Berlin, 1990.
- [36] Abbott, I. H. Von Doenhoff, A.E.V., "and Stivers, L. S. "Summary of Aerofoil Data", *NACA Report No. 824*, 1945.
- [37] White, F.M., "Fluid Mechanics", *McGraw-Hill Series in Mechanical Engineering*, 4<sup>th</sup> Edition , pp. 526, 1999.
- [38] Devenport, W.J. and Schetz, J. A., "The *Investigation of an Inboard-Winglet Application to a Roadable Aircraft*", M.Sc. In Aerospace Engineering Thesis, Virginia polytechnic Institute and State University, pp. 24-26, 2002.



- [39] Mainuddin, M., and Ali, M.A.T., “Experimental Investigation of Lift to Drag Ratio between Volumetric Equivalent Fuselages”, *Proceedings of the 4<sup>th</sup> BSME-ASME International Conference on Thermal Engineering*, Dhaka, Bangladesh, pp. 383-390, 2008.
- [40] Cimbala, J.M., “*Experimental Uncertainty Analysis*”, Online Edition, pp.1-4, 2013.
- [41] Sadraey, M.H., “Aircraft Design: A systems Engineering Approach”, *Wiley Publications -October*, pp. 170-178, 2012.
- [42] Kocyigit, S., “Investigating the Relation between Symmetric Properties and Lift/Drag Coefficients for Airfoils”, *Int. Baccalaureate*, Vol. 58, pp. 29-58, 2015.
- [43] Jin Y., Weibin Y., Jianliang W., Jianbin Xie, Haipeng Z., Mingjun P. and Yong S., “Numerical Simulation of Aerodynamic Performance for Two Dimensional Wind Turbine Airfoils”, *Procedia Engineering*, Vol. 31, pp. 80-86, 2012.
- [44] Kandwal, S., and Singh, S., “Computational Fluid Dynamics Study of Fluid Flow and Aerodynamic Forces on an Airfoil”, *Int. J. of Engineering and Technology*, Vol.1, pp. 1-8, 2012.
- [45] Bhushan S. Patil and Hitesh R. T., “Computational Fluid Dynamics Analysis of Wind Turbine Blade at Various Angles of Attack and different Reynolds Number”, *Procedia Engineering*, Vol. 127, pp. 1363-1369, 2015.
- [46] Prabhakar A., “A CFD Analysis of Static and Dynamic Pressure for NACA 4412”, *Int. J. of Engineering Trends and Technology*, Vol. 4, pp. 3258-3265, 2013.

# APPENDIX-1

**Table 2: Calculated Values of Pressure Coefficient at -4° Angle of Attack**

Segment	%C	Model-1		Model-2		Model-3		Model-4		Model-5	
		$C_{pu}$	$C_{pl}$	$C_{pu}$	$C_{pl}$	$C_{pu}$	$C_{pl}$	$C_{pu}$	$C_{pl}$	$C_{pu}$	$C_{pl}$
Segment-A	20	-0.526641549	-0.807517041	-0.035109437	-0.526641549	-0.035109437	-0.491532112	-0.10532831	-0.596860422	-0.070218873	-0.561750985
	40	-0.421313239	-0.245766056	-0.280875493	-0.070218873	-0.245766056	-0.035109437	-0.315984929	-0.035109437	-0.245766056	-0.035109437
	60	-0.351094366	-0.035109437	-0.210656619	0.035109437	-0.175547183	0.070218873	-0.245766056	0.10532831	-0.175547183	0.140437746
	80	-0.315984929	0.035109437	-0.140437746	0.070218873	-0.10532831	0.10532831	-0.175547183	0.140437746	-0.10532831	0.175547183
	20	-0.491532112	-0.737298168	-0.245766056	-0.561750985	-0.210656619	-0.526641549	-0.245766056	-0.245766056	-0.175547183	-0.210656619
	40	-0.386203802	-0.245766056	-0.456422676	-0.140437746	-0.421313239	-0.10532831	-0.526641549	-0.070218873	-0.456422676	-0.035109437
Segment-B	60	0.035109437	0	-0.526641549	-0.035109437	0	-0.631969858	0.070218873	-0.561750985	-0.561750985	0.10532831
	80	-0.421313239	0.035109437	-0.245766056	0.035109437	-0.210656619	-0.245766056	-0.210656619	-0.175547183	-0.175547183	
	20	-0.456422676	-0.772407605	-0.702188732	-0.175547183	-0.631969858	-0.140437746	-0.772407605	-0.035109437	-0.702188732	0
	40	-0.351094366	-0.210656619	-0.386203802	-0.035109437	-0.351094366	0	-0.421313239	0	-0.351094366	0.035109437
	60	-0.421313239	-0.070218873	-0.175547183	0	-0.140437746	0.035109437	-0.140437746	0.035109437	-0.070218873	0.070218873
	80	0.035109437	0.035109437	-0.070218873	0.035109437	-0.035109437	0.070218873	-0.175547183	0.070218873	-0.10532831	0.10532831
Segment-C	20	-0.631969858	-0.561750985	-0.561750985	-0.386203802	-0.526641549	-0.351094366	-0.561750985	-0.456422676	-0.491532112	-0.386203802
	40	-0.526641549	-0.10532831	-0.386203802	-0.175547183	-0.351094366	-0.140437746	-0.386203802	-0.175547183	-0.315984929	-0.10532831
	60	-0.421313239	-0.070218873	-0.175547183	0	-0.140437746	0.035109437	-0.140437746	0.035109437	-0.070218873	0.070218873
	80	0.035109437	0.035109437	-0.070218873	0.035109437	-0.035109437	0.070218873	-0.175547183	0.070218873	-0.10532831	0.10532831
	20	-0.631969858	-0.561750985	-0.561750985	-0.386203802	-0.526641549	-0.351094366	-0.561750985	-0.456422676	-0.491532112	-0.386203802
	40	-0.526641549	-0.10532831	-0.386203802	-0.175547183	-0.351094366	-0.140437746	-0.386203802	-0.175547183	-0.315984929	-0.10532831
Segment-D	60	-0.386203802	0	-0.245766056	0.035109437	-0.210656619	0.070218873	-0.386203802	0.035109437	-0.315984929	0.070218873
	80	-0.561750985	0	-0.245766056	0.070218873	-0.210656619	0.10532831	-0.315984929	0.070218873	-0.245766056	0.10532831

**Table 3: Calculated Values of Pressure Coefficient at 0° Angle of Attack**

Segment	%C	Model-1		Model-2		Model-3		Model-4		Model-5	
		C <sub>pu</sub>	C <sub>pl</sub>	C <sub>pu</sub>	C <sub>pl</sub>	C <sub>pu</sub>	C <sub>pl</sub>	C <sub>pu</sub>	C <sub>pl</sub>	C <sub>pu</sub>	C <sub>pl</sub>
Segment-A	20	-0.877735914	-0.315984929	-0.140437746	-0.245766056	-0.175547183	-0.280875493	-0.210656619	-0.351094366	-0.140437746	-0.280875493
	40	-0.596860422	-0.245766056	-0.421313239	-0.175547183	-0.456422676	-0.140437746	-0.596860422	-0.035109437	-0.526641549	-0.035109437
	60	-0.456422676	-0.035109437	-0.245766056	0.070218873	-0.280875493	0.035109437	-0.315984929	0.070218873	-0.245766056	0.10532831
	80	-0.245766056	0.035109437	-0.140437746	0.10532831	-0.175547183	0.070218873	-0.210656619	0.10532831	-0.140437746	0.140437746
	20	-0.807517041	0.035109437	-0.596860422	-0.210656619	-0.631969858	-0.245766056	-0.667079295	-0.245766056	-0.596860422	-0.210656619
	40	-0.596860422	0	-0.667079295	-0.070218873	-0.702188732	-0.10532831	-0.702188732	-0.070218873	-0.631969858	-0.10532831
Segment-B	60	0.10532831	-0.035109437	-0.737298168	-0.035109437	-0.772407605	-0.070218873	-0.772407605	-0.035109437	-0.702188732	0
	80	-0.210656619	-0.070218873	-0.280875493	0.10532831	-0.315984929	0.070218873	-0.210656619	0.070218873	-0.140437746	0.10532831
	20	-0.877735914	-0.175547183	-0.983064224	-0.10532831	-1.053283097	-0.140437746	-0.245766056	-0.245766056	-0.10532831	-0.175547183
	40	-0.456422676	-0.280875493	-0.526641549	0.035109437	-0.596860422	0.035109437	-0.421313239	0.035109437	-0.351094366	0.070218873
	60	-0.491532112	-0.245766056	-0.210656619	-0.035109437	-0.245766056	-0.070218873	-0.175547183	-0.035109437	-0.10532831	0
	80	-0.10532831	-0.210656619	-0.140437746	0.035109437	-0.175547183	0.035109437	-0.140437746	0.035109437	-0.070218873	0.070218873
Segment-C	20	-0.912845351	-0.315984929	-0.772407605	-0.175547183	-0.842626478	-0.210656619	-0.877735914	-0.245766056	-0.807517041	-0.210656619
	40	-0.702188732	-0.210656619	-0.456422676	-0.070218873	-0.491532112	-0.10532831	-0.596860422	-0.035109437	-0.526641549	0
	60	-0.456422676	-0.070218873	-0.351094366	-0.035109437	-0.386203802	-0.070218873	-0.456422676	-0.035109437	-0.386203802	0
	80	-0.526641549	0	-0.280875493	0.070218873	-0.315984929	0.070218873	-0.351094366	0.070218873	-0.280875493	0.10532831
Segment-D	20	-0.912845351	-0.315984929	-0.772407605	-0.175547183	-0.842626478	-0.210656619	-0.877735914	-0.245766056	-0.807517041	-0.210656619
	40	-0.702188732	-0.210656619	-0.456422676	-0.070218873	-0.491532112	-0.10532831	-0.596860422	-0.035109437	-0.526641549	0
	60	-0.456422676	-0.070218873	-0.351094366	-0.035109437	-0.386203802	-0.070218873	-0.456422676	-0.035109437	-0.386203802	0
	80	-0.526641549	0	-0.280875493	0.070218873	-0.315984929	0.070218873	-0.351094366	0.070218873	-0.280875493	0.10532831

**Table 4: Calculated Values of Pressure Coefficient at 4° Angle of Attack**

Segment	%C	Model-1		Model-2		Model-3		Model-4		Model-5	
		C <sub>pu</sub>	C <sub>pl</sub>	C <sub>pu</sub>	C <sub>pl</sub>	C <sub>pu</sub>	C <sub>pl</sub>	C <sub>pu</sub>	C <sub>pl</sub>	C <sub>pu</sub>	C <sub>pl</sub>
Segment-A	20	-1.193720844	-0.070218873	-0.421313239	-0.10532831	-0.386203802	-0.070218873	-0.491532112	-0.035109437	-0.421313239	0
	40	-0.807517041	-0.035109437	-0.596860422	0	-0.561750985	0	-0.702188732	0	-0.631969858	0.035109437
	60	-0.315984929	0	-0.315984929	0.070218873	-0.280875493	0.070218873	-0.315984929	0.035109437	-0.315984929	0.070218873
	80	-0.210656619	0.035109437	-0.210656619	0.10532831	-0.175547183	0.140437746	-0.280875493	0.070218873	-0.245766056	0.10532831
	20	-1.193720844	0.070218873	-0.842626478	0.070218873	-0.807517041	0.10532831	-0.947954788	0.070218873	-0.912845351	0.10532831
	40	-0.772407605	-0.035109437	-0.807517041	-0.807517041	-0.772407605	0.035109437	-0.877735914	0.035109437	-0.842626478	0.070218873
Segment-B	60	0.10532831	-0.070218873	-0.702188732	0	-0.667079295	0	-0.807517041	0	-0.772407605	0
	80	-0.140437746	0	-0.175547183	0.070218873	-0.157992465	-0.210656619	0.070218873	-0.175547183	0.10532831	
	20	-0.877735914	-0.070218873	-1.053283097	0	-1.018173661	0	-1.158611407	0	-1.123501971	0
	40	-0.667079295	-0.140437746	-0.702188732	0.070218873	-0.667079295	0.10532831	-0.737298168	0.10532831	-0.702188732	0.10532831
	60	-0.491532112	-0.070218873	-0.561750985	0.035109437	-0.526641549	0.035109437	-0.561750985	0	-0.491532112	0
	80	0.070218873	-0.035109437	-0.175547183	0.10532831	-0.140437746	0.10532831	-0.175547183	0.070218873	-0.175547183	0.10532831
Segment-C	20	-0.877735914	-0.070218873	-0.947954788	-0.035109437	-0.912845351	-0.035109437	-1.053283097	-0.070218873	-0.983064224	-0.035109437
	40	-0.842626478	-0.035109437	-0.772407605	0.10532831	-0.737298168	0.10532831	-0.842626478	0.070218873	-0.807517041	0.10532831
	60	-0.421313239	0	-0.491532112	0	-0.456422676	0	-0.456422676	0	-0.386203802	0
	80	-0.456422676	0	-0.315984929	0.245766056	-0.315984929	0.280875493	-0.315984929	0.140437746	-0.315984929	0.175547183
	20	-0.877735914	-0.070218873	-0.947954788	-0.035109437	-0.912845351	-0.035109437	-1.053283097	-0.070218873	-0.983064224	-0.035109437
	40	-0.842626478	-0.035109437	-0.772407605	0.10532831	-0.737298168	0.10532831	-0.842626478	0.070218873	-0.807517041	0.10532831
Segment-D	60	-0.421313239	0	-0.491532112	0	-0.456422676	0	-0.456422676	0	-0.386203802	0
	80	-0.456422676	0	-0.315984929	0.245766056	-0.315984929	0.280875493	-0.315984929	0.140437746	-0.315984929	0.175547183

**Table 5: Calculated Values of Pressure Coefficient at 8° Angle of Attack**

Segment	%C	Model-1		Model-2		Model-3		Model-4		Model-5	
		C <sub>pu</sub>	C <sub>pl</sub>	C <sub>pu</sub>	C <sub>pl</sub>	C <sub>pu</sub>	C <sub>pl</sub>	C <sub>pu</sub>	C <sub>pl</sub>	C <sub>pu</sub>	C <sub>pl</sub>
Segment-A	20	-1.650143519	0.140437746	-0.877735914	0.175547183	-0.807517041	0.210656619	-0.947954788	0.245766056	-0.912845351	0.280875493
	40	-0.877735914	0.070218873	-0.737298168	0.175547183	-0.667079295	0.210656619	-0.737298168	0.210656619	-0.737298168	0.245766056
	60	-0.456422676	-0.035109437	-0.456422676	0.140437746	-0.421313239	0.175547183	-0.456422676	0.140437746	-0.456422676	0.175547183
	80	-0.210656619	0	-0.245766056	0.10532831	-0.210656619	0.140437746	-0.245766056	0.140437746	-0.245766056	0.175547183
	20	-1.404377463	0.245766056	-1.263939717	0.280875493	-1.22883028	0.315984929	-1.369268027	0.386203802	-1.33415859	0.421313239
	40	-0.842626478	0.070218873	-0.912845351	0.315984929	-0.877735914	0.351094366	-0.947954788	0.280875493	-0.912845351	0.315984929
Segment-B	60	0	0	-0.772407605	0.070218873	-0.737298168	0.10532831	-0.807517041	0.175547183	-0.737298168	0.175547183
	80	-0.10532831	-0.035109437	-0.280875493	0.140437746	-0.245766056	0.175547183	-0.245766056	0.140437746	-0.245766056	0.140437746
	20	-1.018173661	0.140437746	-1.790581266	0.175547183	-1.720362392	0.210656619	-1.931019012	0.386203802	-1.860800139	0.421313239
	40	-0.631969858	0.035109437	-0.772407605	0.245766056	-0.737298168	0.280875493	-0.947954788	0.245766056	-0.877735914	0.280875493
Segment-C	60	-0.561750985	-0.035109437	-0.245766056	0	-0.210656619	0	-0.526641549	0.210656619	-0.491532112	0.245766056
	80	0.070218873	-0.070218873	-0.070218873	0.070218873	-0.035109437	0.070218873	-0.315984929	0.140437746	-0.280875493	0.175547183
	20	-1.088392534	0.10532831	-1.404377463	0.070218873	-1.369268027	0.10532831	-1.650143519	0.245766056	-1.579924646	0.280875493
	40	-0.772407605	0.070218873	-0.842626478	0.245766056	-0.807517041	0.280875493	-0.983064224	0.315984929	-0.947954788	0.351094366
Segment-D	60	-0.456422676	0	-0.526641549	0.035109437	-0.491532112	0.070218873	-0.702188732	0.070218873	-0.667079295	0.10532831
	80	-0.315984929	0.070218873	-0.315984929	0.070218873	-0.280875493	0.10532831	-0.456422676	0.210656619	-0.421313239	0.245766056

**Table 6: Calculated Values of Pressure Coefficient at 12° Angle of Attack**

Segment	%C	Model-1		Model-2		Model-3		Model-4		Model-5	
		$C_{pu}$	$C_{pi}$	$C_{pu}$	$C_{pi}$	$C_{pu}$	$C_{pi}$	$C_{pu}$	$C_{pi}$	$C_{pu}$	$C_{pi}$
Segment-A	20	-1.825690702	0.315984929	-0.947954788	0.245766056	-0.912845351	0.280875493	-1.088392534	0.175547183	-1.053283097	0.140437746
	40	-0.807517041	0.175547183	-0.807517041	0.210656619	-0.842626478	0.245766056	-0.807517041	0.140437746	-0.807517041	0.10532831
	60	-0.315984929	0	-0.526641549	0.175547183	-0.561750985	0.210656619	-0.351094366	0.10532831	-0.315984929	0.070218873
	80	-0.210656619	0.070218873	-0.315984929	0.140437746	-0.280875493	0.175547183	-0.140437746	0.070218873	-0.10532831	0.035109437
	20	-1.720362392	0.456422676	-1.404377463	0.351094366	-1.369268027	0.386203802	-1.263939717	0.351094366	-1.22883028	0.315984929
	40	-0.842626478	0.245766056	-1.018173661	0.315984929	-0.983064224	0.351094366	-1.053283097	0.245766056	-1.018173661	0.245766056
Segment-B	60	-0.631969858	0.10532831	-0.842626478	0.140437746	-0.807517041	0.175547183	-0.842626478	0.140437746	-0.807517041	0.175547183
	80	0	0.070218873	-0.315984929	0.10532831	-0.280875493	0.140437746	-0.210656619	0.070218873	-0.210656619	0.035109437
	20	-1.685252956	0.421313239	-1.860800139	0.315984929	-1.825690702	0.351094366	-1.615034083	0.351094366	-1.579924646	0.315984929
	40	-0.842626478	0.175547183	-0.842626478	0.245766056	-0.807517041	0.280875493	-1.123501971	0.210656619	-1.088392534	0.175547183
Segment-C	60	-0.491532112	0.035109437	-0.315984929	0	-0.280875493	0	-0.842626478	0.175547183	-0.807517041	0.10532831
	80	0.035109437	-0.035109437	-0.140437746	0.070218873	-0.10532831	0.035109437	-0.280875493	0.10532831	-0.245766056	0
	20	-1.720362392	0.315984929	-1.825690702	0.140437746	-1.790581266	0.175547183	-1.650143519	0.351094366	-1.615034083	0.315984929
	40	-0.877735914	0.070218873	-0.912845351	0.315984929	-0.877735914	0.351094366	-0.772407605	0.245766056	-0.737298168	0.210656619
Segment-D	60	-0.491532112	0.10532831	-0.596860422	0.10532831	-0.561750985	0.140437746	-0.526641549	0.035109437	-0.491532112	0.035109437
	80	-0.351094366	0.035109437	-0.245766056	0.140437746	-0.210656619	0.175547183	-0.245766056	0.175547183	-0.210656619	0.140437746

**Table 7: Calculated Values of Pressure Coefficient at 16° Angle of Attack**

Segment	%C	Model-1		Model-2		Model-3		Model-4		Model-5	
		$C_{pu}$	$C_{pl}$	$C_{pu}$	$C_{pl}$	$C_{pu}$	$C_{pl}$	$C_{pu}$	$C_{pl}$	$C_{pu}$	$C_{pl}$
Segment-A	20	-1.825690702	0.386203802	-1.299049153	0.386203802	-1.263939717	0.526641549	-1.755471829	0.526641549	-1.720362392	0.596860422
	40	-0.561750985	0.280875493	-0.8777735914	0.245766056	-0.842626478	0.280875493	-1.018173661	0.351094366	-0.947954788	0.386203802
	60	-0.210656619	0.070218873	-0.315984929	0.10532831	-0.280875493	0.140437746	-0.491532112	0.210656619	-0.456422676	0.245766056
	80	-0.315984929	-0.035109437	-0.210656619	0.070218873	-0.175547183	0.10532831	-0.280875493	0.140437746	-0.245766056	0.175547183
	20	-1.22883028	0.631969858	-1.825690702	0.631969858	-1.790581266	0.702188732	-1.931019012	0.772407605	-1.860800139	0.772407605
	40	-0.351094366	0.386203802	-1.018173661	0.421313239	-0.947954788	0.491532112	-1.299049153	0.491532112	-1.22883028	0.526641549
Segment-B	20	-0.421313239	0.140437746	-0.667079295	0.245766056	-0.596860422	0.280875493	-0.877735914	0.351094366	-0.807517041	0.386203802
	40	-0.351094366	0.035109437	-0.245766056	0.140437746	-0.210656619	0.175547183	-0.491532112	0.140437746	-0.456422676	0.175547183
	60	-0.351094366	0.035109437	-0.245766056	0.140437746	-0.210656619	0.175547183	-0.491532112	0.140437746	-0.456422676	0.175547183
	80	-0.351094366	0.035109437	-0.245766056	0.140437746	-0.210656619	0.175547183	-0.491532112	0.140437746	-0.456422676	0.175547183
	20	-1.369268027	0.491532112	-1.018173661	0.667079295	-0.947954788	0.667079295	-1.474596336	0.596860422	-1.4394869	0.631969858
	40	-0.737298168	0.386203802	-0.807517041	0.561750985	-0.772407605	0.561750985	-0.842626478	0.421313239	-0.807517041	0.456422676
Segment-C	20	-1.650143519	0.421313239	-1.579924646	0.421313239	-1.509705773	0.491532112	-1.755471829	0.631969858	-1.720362392	0.667079295
	40	-0.947954788	0.210656619	-0.667079295	0.280875493	-0.596860422	0.315984929	-0.947954788	0.386203802	-0.912845351	0.456422676
	60	-0.596860422	0.10532831	-0.386203802	0.175547183	-0.315984929	0.210656619	-0.667079295	0.245766056	-0.631969858	0.280875493
	80	0.070218873	-0.035109437	-0.456422676	0.245766056	-0.421313239	0.245766056	-0.210656619	0.140437746	-0.175547183	0.175547183
	20	-1.650143519	0.421313239	-1.579924646	0.421313239	-1.509705773	0.491532112	-1.755471829	0.631969858	-1.720362392	0.667079295
	40	-0.947954788	0.210656619	-0.667079295	0.280875493	-0.596860422	0.315984929	-0.947954788	0.386203802	-0.912845351	0.456422676
Segment-D	20	-1.650143519	0.421313239	-1.579924646	0.421313239	-1.509705773	0.491532112	-1.755471829	0.631969858	-1.720362392	0.667079295
	40	-0.947954788	0.210656619	-0.667079295	0.280875493	-0.596860422	0.315984929	-0.947954788	0.386203802	-0.912845351	0.456422676
	60	-0.596860422	0.10532831	-0.386203802	0.175547183	-0.315984929	0.210656619	-0.667079295	0.245766056	-0.631969858	0.280875493
	80	-0.315984929	0.035109437	-0.491532112	0.070218873	-0.421313239	0.351094366	-0.561750985	0.10532831	-0.526641549	0.140437746

**Table 8: Calculated Values of Pressure Coefficient at 20° Angle of Attack**

Segment	%C	Model-1		Model-2		Model-3		Model-4		Model-5	
		C <sub>pu</sub>	C <sub>pl</sub>	C <sub>pu</sub>	C <sub>pl</sub>	C <sub>pu</sub>	C <sub>pl</sub>	C <sub>pu</sub>	C <sub>pl</sub>	C <sub>pu</sub>	C <sub>pl</sub>
Segment-A	20	-0.351094366	0.456422676	-0.983064224	0.456422676	-0.947954788	0.491532112	-1.22883028	0.526641549	-1.158611407	0.491532112
	40	-0.386203802	0.456422676	-0.561750985	0.386203802	-0.596860422	0.421313239	-0.983064224	0.491532112	-0.947954788	0.456422676
	60	-0.351094366	0.315984929	-0.245766056	0.315984929	-0.245766056	0.351094366	-0.351094366	0.386203802	-0.315984929	0.351094366
	80	-0.421313239	-0.035109437	-0.210656619	0.175547183	-0.210656619	0.210656619	-0.315984929	0.456422676	-0.280875493	0.421313239
	20	-0.526641549	0.351094366	-1.193720844	0.456422676	-1.158611407	0.561750985	-1.158611407	0.561750985	-1.088392534	0.526641549
	40	-0.491532112	0.280875493	-0.491532112	0.351094366	-0.526641549	0.421313239	-0.526641549	0.456422676	-0.491532112	0.421313239
Segment-B	20	-0.491532112	0.10532831	-0.035109437	0.210656619	-0.070218873	0.280875493	-0.561750985	0.386203802	-0.526641549	0.351094366
	40	-0.456422676	-0.035109437	-0.035109437	0.070218873	-0.035109437	0.10532831	-0.596860422	0.245766056	-0.561750985	0.210656619
	60	-0.456422676	-0.035109437	0.070218873	-0.035109437	-0.035109437	0.10532831	-0.596860422	0.245766056	-0.561750985	0.210656619
	80	-0.456422676	-0.035109437	0.070218873	-0.035109437	-0.035109437	0.10532831	-0.596860422	0.245766056	-0.561750985	0.210656619
	20	-0.351094366	0.456422676	-0.456422676	0.386203802	-0.421313239	0.456422676	-1.263939717	0.491532112	-1.158611407	0.456422676
	40	-0.491532112	0.386203802	-0.351094366	0.070218873	-0.315984929	0.070218873	-0.983064224	0.491532112	-0.947954788	0.456422676
Segment-C	20	0.035109437	-0.035109437	-0.175547183	-0.035109437	-0.140437746	-0.035109437	-0.245766056	0.175547183	-0.210656619	0.140437746
	40	-0.421313239	0.10532831	-0.386203802	0	-0.315984929	0.035109437	-0.421313239	0.280875493	-0.386203802	0.245766056
	60	-0.421313239	0.10532831	-0.386203802	0	-0.315984929	0.035109437	-0.421313239	0.280875493	-0.386203802	0.245766056
	80	0.035109437	-0.035109437	-0.175547183	-0.035109437	-0.140437746	-0.035109437	-0.245766056	0.175547183	-0.210656619	0.140437746
	20	-0.737298168	0.315984929	-0.631969858	0.596860422	-0.596860422	0.561750985	-1.33415859	0.596860422	-1.22883028	0.561750985
	40	-0.596860422	0.210656619	-0.526641549	0.526641549	-0.491532112	0.491532112	-0.737298168	0.351094366	-0.702188732	0.315984929
Segment-D	20	-0.667079295	0.070218873	-0.526641549	0.351094366	-0.491532112	0.315984929	-0.421313239	0.245766056	-0.386203802	0.210656619
	40	-0.667079295	0.070218873	-0.526641549	0.351094366	-0.491532112	0.315984929	-0.421313239	0.245766056	-0.386203802	0.210656619
	60	-0.667079295	0.070218873	-0.526641549	0.351094366	-0.491532112	0.315984929	-0.421313239	0.245766056	-0.386203802	0.210656619
	80	-0.807517041	-0.035109437	-0.667079295	0.280875493	-0.631969858	0.245766056	-0.245766056	0.140437746	-0.245766056	0.175547183



**Table 9: Calculated Values of Pressure Coefficient at 24° Angle of Attack**

Segment	%C	Model-1		Model-2		Model-3		Model-4		Model-5	
		C <sub>pu</sub>	C <sub>pl</sub>	C <sub>pu</sub>	C <sub>pl</sub>	C <sub>pu</sub>	C <sub>pl</sub>	C <sub>pu</sub>	C <sub>pl</sub>	C <sub>pu</sub>	C <sub>pl</sub>
Segment-A	20	-0.280875493	0.456422676	-0.983064224	0.596860422	-0.947954788	0.631969858	-1.018173661	0.631969858	-0.947954788	0.667079295
	40	-0.315984929	0.315984929	-0.807517041	0.386203802	-0.772407605	0.421313239	-0.702188732	0.456422676	-0.631969858	0.491532112
	60	-0.315984929	0.070218873	-0.596860422	0.280875493	-0.596860422	0.280875493	-0.596860422	0.386203802	-0.526641549	0.421313239
	80	-0.351094366	-0.035109437	-0.491532112	0.140437746	-0.456422676	0.175547183	-0.491532112	0.175547183	-0.421313239	0.210656619
	20	-0.421313239	0.526641549	-0.702188732	0.772407605	-0.631969858	0.807517041	-0.737298168	0.807517041	-0.667079295	0.842626478
	40	-0.245766056	0.386203802	-0.596860422	0.702188732	-0.561750985	0.737298168	-0.596860422	0.526641549	-0.526641549	0.561750985
Segment-B	60	-0.315984929	0.245766056	-0.526641549	0.351094366	-0.491532112	0.386203802	-0.561750985	0.210656619	-0.491532112	0.245766056
	80	-0.210656619	0	-0.456422676	0.140437746	-0.421313239	0.175547183	-0.491532112	0.070218873	-0.421313239	0.10532831
	20	-0.245766056	0.491532112	-0.456422676	0.596860422	-0.386203802	0.526641549	-0.351094366	0.491532112	-0.280875493	0.526641549
	40	-0.456422676	0.421313239	-0.491532112	0.315984929	-0.421313239	0.351094366	-0.456422676	0.456422676	-0.386203802	0.491532112
	60	-0.421313239	0.140437746	-0.491532112	0.070218873	-0.421313239	0.070218873	-0.491532112	0.245766056	-0.421313239	0.280875493
	80	-0.210656619	-0.035109437	-0.351094366	0	-0.280875493	0	-0.386203802	-0.070218873	-0.315984929	-0.035109437
Segment-C	20	-0.526641549	0.456422676	-0.526641549	0.456422676	-0.456422676	0.491532112	-0.491532112	0.526641549	-0.421313239	0.561750985
	40	-0.456422676	0.351094366	-0.456422676	0.351094366	-0.386203802	0.386203802	-0.456422676	0.491532112	-0.386203802	0.526641549
	60	-0.491532112	0.070218873	-0.491532112	0.070218873	-0.421313239	0.10532831	-0.561750985	0.245766056	-0.491532112	0.280875493
	80	-0.631969858	0	-0.561750985	0.035109437	-0.491532112	0.035109437	-0.596860422	0.10532831	-0.526641549	0.140437746
	20	-0.526641549	0.456422676	-0.526641549	0.456422676	-0.456422676	0.491532112	-0.491532112	0.526641549	-0.421313239	0.561750985
	40	-0.456422676	0.351094366	-0.456422676	0.351094366	-0.386203802	0.386203802	-0.456422676	0.491532112	-0.386203802	0.526641549
Segment-D	60	-0.491532112	0.070218873	-0.491532112	0.070218873	-0.421313239	0.10532831	-0.561750985	0.245766056	-0.491532112	0.280875493
	80	-0.631969858	0	-0.561750985	0.035109437	-0.491532112	0.035109437	-0.596860422	0.10532831	-0.526641549	0.140437746
	20	-0.526641549	0.456422676	-0.526641549	0.456422676	-0.456422676	0.491532112	-0.491532112	0.526641549	-0.421313239	0.561750985
	40	-0.456422676	0.351094366	-0.456422676	0.351094366	-0.386203802	0.386203802	-0.456422676	0.491532112	-0.386203802	0.526641549
	60	-0.491532112	0.070218873	-0.491532112	0.070218873	-0.421313239	0.10532831	-0.561750985	0.245766056	-0.491532112	0.280875493
	80	-0.631969858	0	-0.561750985	0.035109437	-0.491532112	0.035109437	-0.596860422	0.10532831	-0.526641549	0.140437746

# APPENDIX-II

## UNCERTAINTY ANALYSIS

Experimental uncertainty analysis by Cimbala [40] provides a method for predicting the uncertainty of a variable based on its component uncertainty. Furthermore, unless otherwise specified, each of these uncertainties has a confidence level of 95%.

In this investigation, values of pressure coefficients on each surface points are calculated from the respective multi-tube manometer readings obtained during wind tunnel test. The coefficient of lift and coefficient of drag is estimated from the surface pressure coefficients. As such, the uncertainty started from the initial measurement of manometer height and it propagates with the values of  $C_p$ ,  $C_L$  and  $C_D$ . The uncertainty in  $C_p$ ,  $C_L$  and  $C_D$  can be estimated if their components individual uncertainty is known.

The equation of  $C_p$  can be rewritten in terms of all its components from equation (4.2) as follows:

$$C_p = \frac{\rho_{water} \times g \times \Delta H_{Multitubemanometer}}{\frac{1}{2} \rho_{air} \times U_{\alpha}^2} = f(g, \rho_{water}, \rho_{air}, U_{\alpha}, \Delta H_{Multitubemanometer})$$

Due to temperature rise during the experiment, the density of air is changed. So, uncertainty of 0.02 may be assumed as the uncertainty of  $\rho_{air}$  (air density at 29°C). Uncertainty in the measurement of height from the multi-tube manometer may be assumed 0.001 (as the reading vary  $\pm 1.0$  mm or 0.001 m from the actual reading). The uncertainty in other components of  $C_p$  can be neglected. So,

$$u_{\rho_{air}} = 0.02$$

$$u_{\Delta H} = 0.001$$

The expected uncertainty in  $C_p$  can be estimated from the following formula:

$$U_{c_p} = \sqrt{(u_{\rho_{air}} \frac{\partial C_p}{\partial \rho_{air}})^2 + (u_{\Delta H} \frac{\partial C_p}{\partial \Delta H})^2} \text{-----(1)}$$

Let us consider the case of segment-A of rectangular wing(Model-1) at  $0^\circ$  AOA. There, at 20% chord on the upper surface,  $\Delta H = -0.150$  mm,  $\rho_{air} = 1.15$  kg/m<sup>3</sup> and corresponding  $C_p = 0.5267$ . So, from equation (1),

$$\frac{\partial C_p}{\partial \rho_{air}} = \frac{-C_p}{\rho_{air}^2} = \frac{-(-0.5267)}{1.15^2} = 0.398$$

$$\frac{\partial C_p}{\partial \Delta H} = \frac{C_p}{\Delta H} = \frac{(-0.5267)}{(-0.015)} = 35.11$$

Putting the above two values and the component uncertainties in equation (1), we get the uncertainty of  $C_p$  as:

$$U_{c_p} = \sqrt{(0.02 \times 0.398)^2 + (0.001 \times 35.11)^2} = 0.036$$

So, the uncertainty in  $C_p$  is 3.6%. Similarly, from the respective equation of  $C_L$  and  $C_D$  their corresponding uncertainty can be calculated considering the uncertainty of respective  $C_p$  values.